Title
Transient Plasma Effects in Optical-field Ionized Helium Gas

Author
Huang, Chen-Kang

Publication Date
2020

Peer reviewed|Thesis/dissertation

UNIVERSITY OF CALIFORNIA
Los Angeles

Transient Plasma Effects in Optical-field Ionized Helium Gas

A dissertation submitted in partial satisfaction
of the requirements for the degree
Doctor of Philosophy in Electrical and Computer Engineering

by

Chen-Kang Huang

2020

ABSTRACT OF THE DISSERTATION

Transient Plasma Effects in Optical-field Ionized Helium Gas

by

Chen-Kang Huang
Doctor of Philosophy in Electrical and Computer Engineering
University of California, Los Angeles, 2020
Professor Chandrashekar Joshi, Chair

Optical-field ionization (OFI) is often used to produce plasmas for myriad laboratory applications. In this thesis, the electron velocity distribution functions of OFI helium plasmas are shown to be controlled by changing the wavelength and polarization of a sub 100 fs pump laser and ionization state of the plasma. Thomson scattering is used to measure the distinct electron velocity distributions of helium plasmas produced by linearly and circularly polarized laser pulses within a few inverse plasma periods after the plasma formation. In both cases, nonthermal and highly anisotropic initial electron velocity distributions (EVD) are observed that are consistent with expectations from OFI of both He electrons.

Such OFI plasmas are used to study two important problems in plasma physics. First we show that the ability to initialize the EVD of electrons allows kinetic plasma instabilities to be studied in the laboratory. Second we carry out a comprehensive study of transfer of spin and orbital angular momentum in the process of second harmonic generation.

We show that following the ionization but before collisions thermalize the electrons, the OFI plasma undergoes two-stream, filamentation, and Weibel instabilities that isotropize the electron distributions. The polarization-dependent frequency and growth rates of these kinetic instabilities, measured using Thomson scattering of a probe laser, agree well with the kinetic theory and simulations. Thus, we have demonstrated an easily deployable laboratory platform for studying kinetic instabilities in plasmas.

The source and the angular momentum properties of the second harmonic beams generated from underdense OFI plasmas are studied. When laser beams with angular momentum interact with plasmas, one can observe the interplay between the spin and the orbital angular momentum. Here, by measuring the helical phase of the second harmonic 2ω radiation generated in an underdense plasma using a known spin and orbital angular momentum pump beam, we verify that the total angular momentum of photons is conserved in the generation of 2ω photons and observe the conversion of spin to orbital angular momentum. We further determine the source of the 2ω light by analyzing near field intensity distributions of the 2ω light. The 2ω images are consistent with these photons being generated near the largest intensity gradients of the pump beam in the plasma as predicted by the combined effect of spin and orbital angular momentum when Laguerre-Gaussian beams are used.

The dissertation of Chen-Kang Huang is approved.

Chee Wei Wong

Pietro Musumeci

Warren B. Mori

Chandrashekar Joshi, Committee Chair

University of California, Los Angeles

2020

Table of Contents

List of Figures

Acknowledgments

First and foremost, I would like to express my heartfelt gratitude to Professor Chan Joshi for his support, encouragement, and guidance throughout my years at UCLA. I am fortunate to have Professor Joshi as my advisor and a great source of inspiration. He is genuinely interested in students' well-being not only in research but life in general. I will always thank him for showing confidence in me, giving me opportunities to present my works at many conferences, as well as showing me how to be a critical thinker and an effective communicator. This dissertation would not be possible without his leadership and wisdom.

I would like to pay special thanks to many individuals in the 3rd-floor lab where I spent most of my doctoral time working and learning. Ken Marsh, who spent tremendous amount of time in lab helping me with my studies, taught me everything to become a good experimentalist. Chaojie Zhang, with whom I started to collaborate since the days at NCU in Taiwan, helped me both in conducting experiments and performing simulations to interpret the results. Chris Clayton, who is always willing to share his insights and experiences even after his retirement, has offered many valuable suggestions on my research. In the first half of my years at UCLA, I enjoyed the company of Nuno Lemos, Jessie Shaw, and Navid Vafaei-Najafabadi who helped me to overcome many challenges as a new international student. Lately, I had the great pleasure of working with Zan Nie and Yipeng Wu, who are both excellent scientists and good friends. Thanks to my fellow students Hiroki Fujii, Mitchell Sinclair, and Noa Nambu for the numerous discussions, encouragement, and friendship.

Next, I would like to thank members of the Neptune laboratory at UCLA for many insightful scientific discussions and expanding my knowledge spectrum. Thanks to Sergei Tochitsky for his good comments on my talks and kind encouragement. Thanks to Eric Welch, Jeremy Pigeon, and Daniel Matteo for their camaraderie and support over the years. Thanks to Dana Tovey, Jennifer Quintana, and Gerhard Louwrens for many delightful lunch conversations. Also thanks to Maria Guerrero and Michelle Phan for handling administrative

tasks and making life much easier for us.

I would like to extend my gratitude to Professor Warren Mori and members of his group, especially Xinlu Xu and Fei Li, for their useful comments and suggestions on my works. Thanks to Frank Tsung, Weiming An, Ben Winjum, Yujian Zhao, Lance Hildebrand, Kyle Miller, and Roman Lee for their friendship and support at several conferences. Also special thanks to Thamine Dalichaouch for being a great friend, colleague, and roommate.

I am indebted to Professor Jyhpyng Wang of Academia Sinica and Professor Wei Lu of Tsinghua University for leading me to this fascinating research area and this extraordinary group. I am also grateful to Professor Chee Wei Wong and Professor Pietro Musumeci for serving in my dissertation committee.

Finally, I would like to thank my parents, my family, and my friends for their endless support and encouragement. Thanks to Angel for her patience, understanding, and love.

This work was supported by DOE grant DE-SC0010064, NSF grant 1734315, AFOSR grant FA9550-16-1-0139, and ONR MURI award N00014-17-1-2705. The simulations were performed on Hoffman cluster at UCLA, Edison and Cori clusters at National Energy Research Scientific Computing Centre (NERSC).

Curriculum Vitae

2004 – 2008	B.S. in Electrical Engineering, National Taiwan University (NTU), Taipei, Taiwan.
2008 – 2010	M.S. in Physics, National Taiwan University (NTU), Taipei, Taiwan.
2014 – 2020	Ph.D. in Electrical and Computer Engineering, University of California, Los Angeles (UCLA).

Publications

[1] C. J. Zhang, J. F. Hua, Y. P. Wu, Y. Fang, Y. Ma, T. L. Zhang, S. Liu, B. Peng, Y. X. He, **C. K. Huang**, K. A. Marsh, W. B. Mori, W. Lu, and C. Joshi, "Measurements of the growth and saturation of electron Weibel instability in optical-field ionized plasmas" Phys. Rev. Lett. **125**, 255001 (2020) .

[2] **C.-K. Huang**, C.-J. Zhang, Z. Nie, K. A. Marsh, C. E. Clayton, and C. Joshi, "Conservation of angular momentum in second harmonic generation from under-dense plasmas" Commun. Phys. **3**, 213 (2020).

[3] **C.-K. Huang**, C.-J. Zhang, K. A. Marsh, C. E. Clayton, and C. Joshi, "Initializing anisotropic electron velocity distribution functions in optical-field ionized plasmas" Plasma Phys. Control. Fusion **62**, 024011 (2020).

[4] C. J. Zhang, **C. K. Huang**, K. A. Marsh, and C. Joshi, "Probing thermal Weibel instability in optical-field-ionized plasmas using relativistic electron bunches" Plasma Phys. Control. Fusion **62**, 024010 (2020).

[5] C. J. Zhang, **C. K. Huang**, K. A. Marsh, X. L. Xu, F. Li, M. Hogan, V. Yakimenko, S. Corde, W. B. Mori, and C. Joshi, "Effect of fluctuations in the down ramp plasma source profile on the emittance and current profile of the self-injected beam in a plasma wakefield accelerator" Phys. Rev. Accel. Beams **22**, 111301 (2019).

[6] C. J. Zhang, **C. K. Huang**, K. A. Marsh, C. E. Clayton, W. B. Mori, and C. Joshi, "Ultrafast optical field–ionized gases—A laboratory platform for studying kinetic plasma instabilities" Sci. Adv. **5**, eaax4545 (2019).

[7] **C. K. Huang**, N. Lemos, X. L. Xu, and C. Joshi, "Orbital angular momentum in the light emitted from laser-plasma accelerators" AIP Conf. Proc. **1812**, 100015 (2017).

CHAPTER 1

Introduction

Since the invention of the Q-switched ruby laser in 1960s, optical breakdown of gases has been intensely studied. A laser-ionized gas is one of the most important experimental platforms for atomic and plasma physics. Although they are closely related, atomic and plasma physics represent two different perspectives on matters: the former mostly considers the medium as atoms in isolation; the latter treats the medium as an ensemble of charged particles that is overall charge-neutral. Which perspectives is dominant for a particular situation depends on the density and average kinetic energy of the charged particles [1]. Generally speaking, an ionized gas is classified as a plasma when its density is high enough such that collective behavior of charged particles starts to manifest itself as charge density waves for example. In this dissertation, initial conditions of laser-ionized gases are studied at relatively high densities. Even though at the low density limit the system can be well-described by the atomic physical model, many collective behaviors that can only be explained in context of plasma physics have been observed at a higher density.

Intense femtosecond lasers are known to ionize atoms through optical-field ionization (OFI). In this process, bound electrons either tunnel through or directly overcome the strong-field-suppressed Coulomb barrier and the released electrons gain kinetic energy depending on the instantaneous electric field and phase of the laser [2]. Therefore, the residual energy and initial electron velocity distribution functions (EVDF) of ionized electrons are controlled by OFI process. Due to its unique features, OFI using intense ultrashort laser pulses has applied to high-harmonic generation [3], soft x-ray/XUV laser [4, 5], plasma channel formation [6, 7, 8], plasma-based photon and electron accelerators [9, 10], and attosecond pulse generation [11]. Each application requires distinct properties based on different experimen-

tal approaches. For examples, linearly polarized lasers can produce cold dense plasmas ideal for recombination x-ray lasers [12]; while a circularly polarized laser pulse can produce a hot, low-density plasma that evolves into a low-density plasma waveguide for laser wakefield acceleration [8].

Aside from these applications, the plasmas initialized by OFI process are of fundamental interest. The process that systematically produces non-Maxwellian and anisotropic velocity distributions affords an opportunity to quantitatively test the kinetic theory of plasmas. The theoretical foundation of plasma physics has a conceptual hierarchy: exact microscopic or single particle description, kinetic theory and fluid theory [1]. There are important physical problems in ionospheric, cosmic, and terrestrial plasmas where the complete single particle description is impractical whereas the fluid model is inadequate. In such cases the plasma must be described in terms of velocity distribution functions- this is the basis of kinetic theory of plasmas [13]. When the velocity distribution functions are nonthermal, plasmas are susceptible to kinetic instabilities such as the streaming [14], electron filamentation [15], and Weibel [16] instability. The kinetic plasma instabilities due to nonthermal plasmas are thought to occur in extremely broad range of situations, including gamma ray bursts [17], electron-positron plasmas [18, 19], collisionless shocks [20], solar corona and interplanetary medium [21, 22, 23], solar wind [24, 25, 26, 27], supernovae explosions [28, 29], quark-gluon plasmas [30, 31, 32], and fast ignition-inertial confinement fusion [33, 34]. For OFI plasmas, kinetic instabilities that follow the creation of anisotropic EVDF have been predicted [35, 36, 37]. Much of this work is theoretical since it has not been possible to initialize the initial EVDF of plasma species. One of the goal of this thesis was to show that an OFI plasma can be an ideal platform for such experimental study of kinetic instabilities.

Experimental validation of the theory of these instabilities is predicated upon having a direct knowledge of the initial velocity distribution functions of the plasma species. In Chapter 2, we show one can create plasmas with known EVDF by using an appropriate combination of laser wavelength(s), intensity profile, polarization, direction of propagation and ionization state of gases/molecules. The polarization dependence of OFI produced electrons has

been tested in previous work in either the long-wavelength [2] or the barrier suppression limit using very low-pressure gases [38, 39]. Moore et al. [40] showed that when intense ($a_0 \sim O(1)$), longer laser pulses are used, the electrons gain additional energy from the ponderomotive potential of the laser envelope. Glover et. al. [41] used Thomson scattering diagnostic probe an OFI He plasma produced using a femtosecond linearly polarized 800 nm pulse and fitted the scattering spectra with thermalized electron temperatures. The same group later used time-resolved spectral measurements of the recombination emission of OFI plasmas to infer non-Maxwellian initial distributions [42]. In spite of these two studies, there is no comprehensive and direct experimental proof of the nonthermal and/or highly anisotropic distributions expected in dense OFI plasmas, at least on a very short timescale. Such an effort would require a probing technique that can directly reveal electron distributions with sub-picosecond temporal resolution. In principle an ultrashort laser pulse can generate such dense plasmas on 10 fs timescale and also measure its density and temperature on a sub-picosecond timescale via the Thomson scattering diagnostic method, however the previous work mentioned above [43, 41] did not have the time resolution to directly observe the non-thermal nature of the EVDF from Thomson scattering measurements. In Chapter 3, we demonstrate the measurement of nonthermal and anisotropic initial EVDF in OFI He plasmas by using an improved short-pulse Thomson scattering technique.

A detailed knowledge of the OFI plasma dynamics (in particular how the "effective plasma temperatures" in the three spatial dimensions evolve as a function of time) is critical for kinetic plasma physics studies or optimizing applications. An ultrafast diagnostic method is needed in order to capture the transient dynamics from the highly nonequilibrium initial conditions. Time-resolved spectroscopy were applied for OFI plasma but was limited by the coarse temporal and spatial resolutions [42]. Ultrashort electron beams generated by a LWFA and a pulse laser photocathode have been successfully applied to measure the dynamics of electric field distribution in a plasma wake [44] and an OFI plasma [45], respectively. The time-resolved plasma density profiles of OFI plasmas were measured by optical interferometry [46, 47]. However, none of these methods are applicable for probing the field

and density fluctuations caused by plasma kinetic instabilities. In Chapter 4, we show the transient dynamics of OFI He plasmas from time-resolve short-pulse Thomson scattering measurements and particle-in-cell simulations. We find that the evolution of the streaming and oblique filamentation instabilities is strongly dependent on the initial EVDF, which is controlled by the polarization of the pump laser, as predicted by kinetic theory.

Polarization of a laser beam is known to be associated with the spin angular momentum of light. Beth [48] demonstrated the transfer of spin angular momentum from a circularly polarized light beam to a birefringent disc. Angular momentum transfer can also occur between a circular polarized laser beam and a plasma. It has been theoretically shown that during the absorption of a short circularly polarized laser pulse, a torque is delivered to plasma electrons, resulting in the generation of an induced azimuthal electric field and an axial magnetic field [49]. In Chapter 5, we show the theoretical and experimental study of the second harmonic generation in underdense plasmas by a laser beam with optical angular momentum. It is found when a short intense pulse of circularly polarized laser is focused to an underdense plasma, the emergent second harmonic beam will have a helical phase front. Such a property is associated with the orbital angular momentum of light. Further experiments show the sum of spin and orbital angular momentum is conserved in this second order nonlinear process.

CHAPTER 2

Distribution Functions of Optical-field Ionized Plasmas

In this chapter, controllable electron velocity distribution functions (EVDF) of optical-field-ionized plasmas are demonstrated and compared against theoretical calculations and particle-in-cell (PIC) simulations. The control can be realized by simply modifying the ionizing laser's polarization as shown in the 2D electron distributions that changes from linear polarization (LP), elliptical polarization (EP), to circular polarization (CP). Some fundamental physics, such as tunnel ionization, ionization heating, and plasma sheath formation, that are related to this phenomenon are discussed. The first two of these physical effects have been extensively explored in the framework of atomic physics. Under most circumstances, the dynamics of the photoelectrons and ions are subject to the electromagnetic field can be well applied to both atomic physics and plasma physics. However, we can clearly see the collective plasma effects take place in laser-ionized high-density plasmas from computer simulations. The implication of plasma effects will be elaborated in later chapters.

2.1 Optical-field ionization

With the advent of technologies (Q-switching, mode locking, and chirped-pulse amplification [50]) that have led to a disruptive increase in the intensity of high-power lasers, it becomes possible to ionize atoms (or molecules) using an optical beam whose photon energy is much less than the ionization potential of the atom [51]. The mechanism of ionization varies depending on the intensity, wavelength, duration of the laser, and the atom/ion being ionized. In the process called multiphoton ionization (MPI), a bound electron in the atom can simultaneously absorb energy of several photons and become a free electron (one that is

no longer bound by the atomic potential). At moderate laser intensity, MPI photoelectron spectra from atoms ionizing using ns and ps laser pulses were quantitatively explained by time dependent perturbation theory [52, 53]. However, at the low frequency limit (such as ionization by a CO_2 laser), a different mechanism called tunnel ionization, first proposed by Keldysh [54], is required since simultaneous absorption of more than 100 photons needed to overcome the ionization potential is practically forbidden for MPI. Tunneling of a bound electron can happen when the quasi-static laser field effectively (when tunneling time is negligible compared to 1/4 laser period) tilts the Coulomb potential well of the atom so that the bound electron may tunnel through the reduced energy barrier.

It turns out that the multiphoton and tunnel ionization are two limiting cases of the universal process of nonlinear ionization [55]. Keldysh introduced a parameter to separate these two regimes, known as the Keldysh parameter

$$\gamma_{\mathrm{k}} = \left(\frac{U_i}{2U_{\mathrm{p}}}\right)^{1/2} \tag{2.1}$$

where U_i is the ionization potential of the atom or ion in question, and U_{p} is the ponderomotive potential

$$U_{\mathrm{P}}(\mathrm{eV}) = \frac{e^2 E_0^2}{4 m_e \omega_0^2} \approx 9.3 \times 10^{-14} I_0(\mathrm{W/cm^2}) \lambda_0^2(\mu\mathrm{m}) \tag{2.2}$$

which is the average kinetic energy of an electron in the laser field. Here e is the charge of the electron, m_e is the mass the electron, ω_0 is the laser frequency, E_0 is the electric field strength of the laser, I_0 is the intensity of the laser, and λ_0 is the laser wavelength.

When $\gamma_{\mathrm{k}} \gg 1$, the ionization is dominated by the multiphoton effect. This regime corresponds to a relatively high frequency and low field strength of laser radiation. Oppsitely, when $\gamma_{\mathrm{k}} < 1$, the ionization is accurately described by the tunnel ionization, which is realized at a low frequency and high field strength. A simple model enables estimation of the laser intensity necessary for tunnel ionization to happen [56]. When the laser intensity is high enough to suppress the ionization potential of a given electron, the bound electron effectively

Atom/ion	U_i [eV]	$I_{\mathrm{BSI}}\left[\mathrm{W/cm^2}\right]$	$U_{\mathrm{p,BSI}}$ [eV]	γ_{k} at I_{BSI}
H	13.6	1.37×10^{14}	8.1	0.91
He	24.6	1.46×10^{15}	87	0.38
He^{1+}	54.4	8.77×10^{15}	520	0.23

Table 2.1: **The OFI parameters for hydrogen and helium.** U_i: ionization potential; I_{BSI}: Barrier-suppression ionization threshold intensity; U_{p}: ponderomotive potential; γ_{k}: Keldysh parameter. U_{p} and γ_{k} are calculated at the intensity of I_{BSI} for a 0.8 μm laser.

see no potential barrier and become free from the parent atom. In this so called barrier-suppression ionization (BSI) model [56], the ionization occurs instantaneously (since the electrons no longer has to tunnel through the barrier) when intensity reaches a threshold intensity, denoted as I_{BSI},

$$I_{\mathrm{BSI}}\left[\mathrm{W/cm^2}\right] = \frac{U_i^4}{128\pi Z^2 e^6} \approx 4\times10^9 \frac{[U_i(\mathrm{eV})]^4}{Z_{\mathrm{eff}}^2}. \tag{2.3}$$

where Z_{eff} is the effective atomic number for the atom/ion.

In this work, a short-pulse 0.8 μm (photon energy 1.55 eV) laser is used ionize hydrogen or helium gases. Table 2.1 lists some of the key parameters associated with optical-field ionization for atoms/ions that are considered here. It shows once the peak intensity is higher than I_{BSI}, the ionization is in tunnel ionization regime ($\gamma_{\mathrm{k}} < 1$). By keeping the pulse short and the peak intensity high above I_{BSI}, we ensure that MPI is negligible even in the rising part of laser pulse and atoms are fully ionized before the peak of the pulse is reached.

The population evolution of ion species for a given atom in a laser field is calculated by solving the ionization rate equations. A Gaussian pulse envelope is assumed and the recombination effect is ignored in these calculations. For the atom with atomic number Z, the rate equations are

$$\begin{cases} \dfrac{dN_0}{dt} &= -N_0 W_{01} \\ \dfrac{dN_1}{dt} &= -N_1 W_{12} + N_0 W_{01} \\ & \vdots \\ \dfrac{dN_z}{dt} &= N_{z-1} W_{z-1,z} \end{cases} \tag{2.4}$$

where N_j is density of ions in ionization stage j, and $W_{j,j+1}$ is the ionization rate of the ionic species j. The formula of ionization rate W depends which tunneling model is adopted. Although the BSI model may give the ion yields that qualitative agree with experimental measurements [56], quantitative studies usually need more sophisticated models. One of such models is developed by Perelomov, Popov and Terent, known as PPT model [57]. This model has been shown to fit well for a wide range of γ_k with experimental results using femtosecond 0.8 μm Ti:sapphire laser [58]. In our case, a quasi-static model simplified from PPT theory, called ADK model [59], is used. For $\gamma_k \ll 1$, PPT theory converges to the standard ADK ionization rate:

$$W(t) = 2\omega_a \frac{(2l+1)(l+|m|)!}{2^{|m|}(|m|)!(l+|m|)!} \frac{U_i}{U_{\mathrm{H}}} \left[2 \left(\frac{U_i}{U_{\mathrm{H}}} \right)^{3/2} \frac{E_a}{E_0(t)} \right]^{2n^* - |m| - 1} \exp\left[-\frac{2}{3} \left(\frac{U_i}{U_{\mathrm{H}}} \right)^{3/2} \frac{E_a}{E_0(t)} \right] \tag{2.5}$$

where $\omega_a \sim 4.1 \times 10^{16}$ Hz is the atomic unit of freuqency, $U_{\mathrm{H}} = 13.6$ eV is the ionization potentials of hydrogen, $n^* = Z/\sqrt{U_i/U_{\mathrm{H}}}$ is the effective principle quantum number, Z is the charge of the nucleus, l and m are the angular momentum and magnetic quantum numbers, $E_a \sim 5.1 \times 10^9$ V/cm is the atomic field strength at the first Bohr radius of hydrogen, and $E_0(t)$ is the instantaneous electric field strength. Given the laser parameters, the initial atom density, and the ionization potential in each ionization stage, the evolution of the ion populations can be calculated by using Eq. (2.4) and (2.5).

Fig. 2.1(a) and (b) plot the evolution of the relative population of helium ion species in response to linearly and circularly polarized laser pulses, respectively. The laser pulses have a laser wavelength of 800 nm, pulse duration of 50 fs (FWHM), and the same field strength

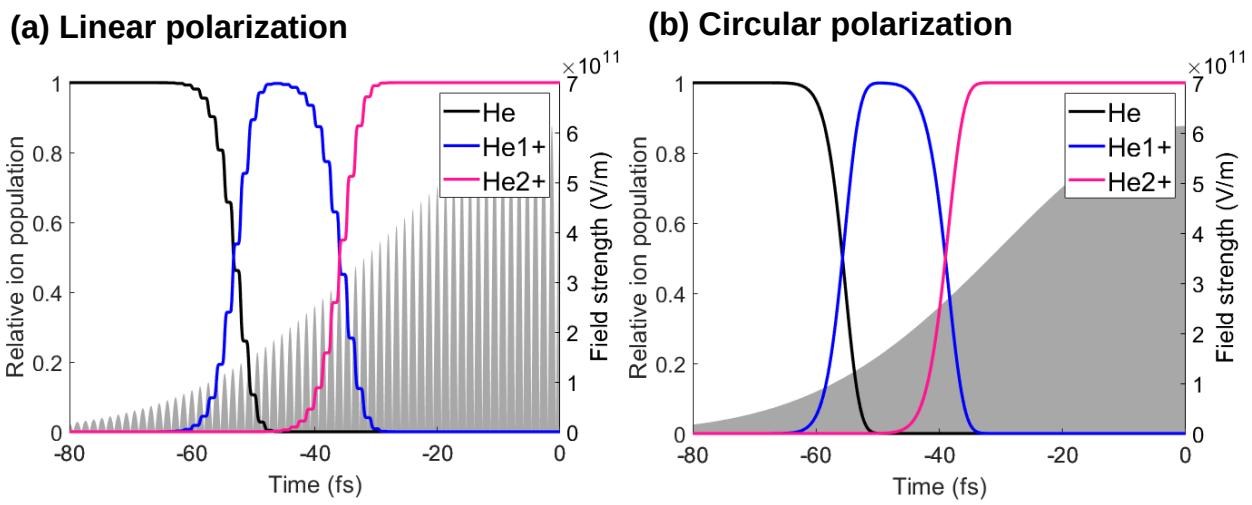

Figure 2.1: **Tunnel ionization of helium.** Calculated evolution of the relative population of helium atom and ion inside the laser field (gray shade) of (a) a linearly polarized pulse and (b) a circularly polarized pulse. The ionizing lasers have Gaussian envelops, a central wavelength of 800 nm , duration of 50 fs (FWHM), and the peak intensity of 5×10^{16} W/cm^2 (linear).

(corresponding to the intensity of 5×10^{16} W/cm^2 for a linear polarized pulse). The gray areas in the figures show the respective pulse wave forms. In the case of linear polarization, the evolution curves are not smooth and have step-like shapes. This is because the electric field oscillates sinusoidally and the ionization only occurs near the peak values. Consequently the period between the two successive ionization steps is equal to the half cycle of the laser field. In contrast, with circular polarization, the evolution curves are continuous and much smoother because the electric field strength increases continuously with time.

2.2 Plasmas generated by OFI

2.2.1 Semi-classical two-step model

In the tunnel ionization regime ($\gamma_k < 1$), the dynamics of the ionized particles can be described by a two-step process [2]. First, the electron is removed from the atom, absorbs

an amount of energy equal to the ionization potential, and becomes a free electron. Second, the electron and the ion are accelerated by the laser field and gain some kinetic energy after the laser pulse has passed. This semi-classical model, sometimes referred as the "simple man's model"', has successfully explained many strong field physics phenomena, including high-harmonic generation [3], angular distribution of photoelectrons [60], and the energy spectrum of the ionized electrons [61, 62].

The calculation of the motion of a charged particle in this model is very much simplified because the ionization process (quantum process) and the subsequent motion (classical process modelled by equations of motion) are separated. We consider here only the motion of electrons, but the same principle can be applied to ions. Assume an electron is released at time $t = t_0$ in an intense electric field $\mathbf{E}(t) = E_0(t)\cos(\omega t)\,\hat{\mathbf{x}} - \sigma E_0(t)\sin(\omega)\,\hat{\mathbf{y}}$, where $E_0(t)$ is the slow-varying amplitude of electric field strength and σ describes the polarization state of the laser ($\sigma = 0$ for linear polarization; $\sigma = \pm 1$ for circular polarization), the electron is initially at rest and then accelerated by the Lorentz force. By solving the equation motion (ignoring the magnetic field), the velocity of the electron is obtained for $t \geq t_0$

$$\begin{aligned} v_x(t) &= \frac{eE_0(t)}{m_e\omega}\sin(\omega t) - \frac{eE_0(t_0)}{m_e\omega}\sin(\omega t_0) \\ v_y(t) &= \sigma\left[\frac{eE_0(t)}{m_e\omega}\cos(\omega t) - \frac{eE_0(t_0)}{m_e\omega}\cos(\omega t_0)\right] \end{aligned} \tag{2.6}$$

and the cycle-averaged kinetic energy of this electron is $U_\mathrm{k} = \frac{1}{2}m_e\left(\left\langle v_x^2(t)\right\rangle + \left\langle v_y^2(t)\right\rangle\right)$. By inserting Eq. (2.6), we have

$$U_\mathrm{k}(t) = \frac{eE_0(t)}{4m_e\omega}\left(1+\sigma^2\right) + \frac{eE_0(t_0)}{2m_e\omega}\left[\sin^2(\omega t_0) + \sigma^2\cos^2(\omega t_0)\right] \tag{2.7}$$

where $|\sigma| \leq 1$. The first term of Eq. (2.7) corresponds to the quiver kinetic energy and the second term corresponds to the drift kinetic energy.

2.2.2 Residual energy

It is clear even after the laser field disappears the second term of Eq. (2.7) remains. The kinetic energy gained from the ionization process is known as the residual energy. The value of the residual energy depends on the polarization of the laser as well as the phase and instantaneous field strength when the particle is released. For a linearly polarized laser ($\sigma = 0$), the residual energy for a photoelectron is

$$U_{\mathrm{res,LP}} = 2U_{\mathrm{P}}(t_0)\sin^2(\omega t_0) \tag{2.8}$$

where $U_{\mathrm{P}}(t_0)$ is the Ponderomotive potential at time t_0. Note that the residual energy shown in Eq. (2.8) has a sinusoidal component that has a $\pi/2$ phase shift relative to the ionizing laser field. Because the tunnel ionization rate is strongly centralized at the peaks of the field, which in the LP case are at the phase of $\omega t_0 = n\pi$ where n is an integer, the residual energy distribution is peaked at a kinetic energy of zero. On the other hand, for a circularly polarized laser ($\sigma = \pm 1$), we have

$$U_{\mathrm{res,CP}} = 2U_{\mathrm{P}}(t_0) \tag{2.9}$$

The residual energy in this case depends only on the field strength at the time of ionization. Fig. 2.2 demonstrates the residual energy spectra calculated for hydrogen and helium gases with the same parameters that are used in 2.1. The energy distributions from different polarizations are distinct: for linear, there is a small portion of electrons gaining high energy but most electrons are cold; for circular, electron energy distributions peak near the energy of $2U_{p,\mathrm{BSI}}$ of the associated ionic species (shown in Table 2.1). Therefore, by controlling the polarization at a given intensity, one may generate cold plasmas using linearly polarized laser pulses or hotter plasmas using circularly polarized pulses. For short laser pulses and low plasma densities, this is the dominant heating mechanism, also known as above-threshold ionization heating.

So far we have only employed the non-relativistic treatment, which is valid for $a_0 \ll 1$.

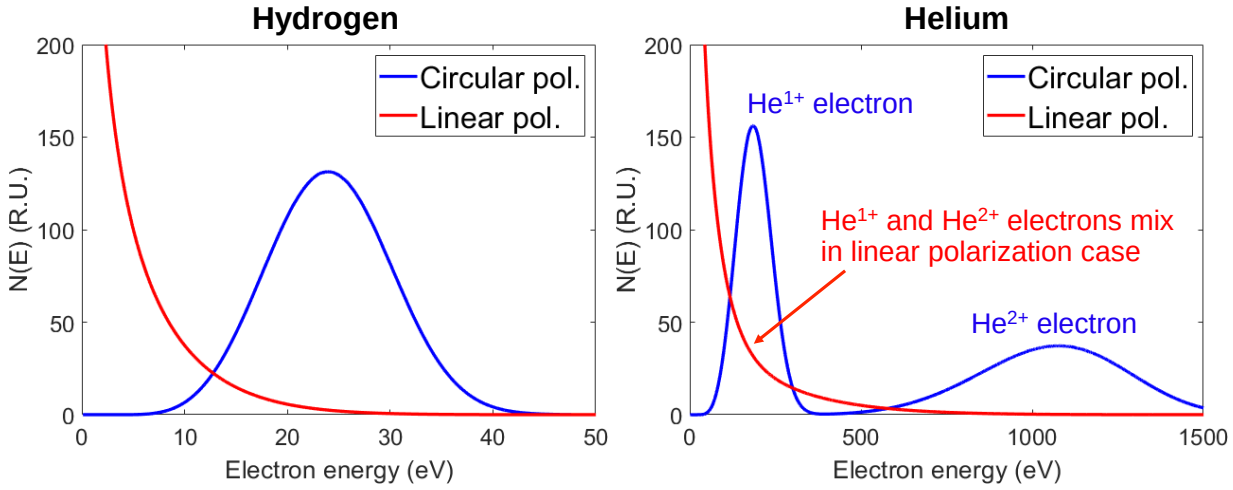

Figure 2.2: **Residual electron energy spectrum by a Gaussian laser pulse.** The calculations are done with laser intensities of 5×10^{15} W/cm^2 (hydrogen) and 5×10^{16} W/cm^2 (helium) using ADK model. He^{1+}electrons are released from He atoms and He^{2+}electrons are released from He^{1+} ions.

Here $a_0 = eA/m_e c^2 = eE/m_e\omega_0 c$ is the normalized laser strength parameter, where A is the peak value of the vector potential and c is the speed of light. A more general approach is to compute the constants of motion from the equations of motion and energy in Lorenz gauge. Consider an electron is released in an electromagnetic field with a transverse vector potential $A_\perp(t)$, the conservation of the canonical momentum gives

$$p_\perp - \frac{e}{c}A_\perp(t) = C \tag{2.10}$$

where $p_\perp$ is the transverse kinetic momentum (perpendicular to the laser propagation) and C is the constant of motion. Since the electron is assumed to be at rest when it is released at time $t = t_0$, the constant of motion has to be $-\frac{e}{c}A_\perp(t_0)$. When the electromagnetic field disappears, the residual momentum in the transverse direction equals to $p_\perp = -\frac{e}{c}A_\perp(t_0)$. In addition, there is a momentum component in the longitudinal direction. Therefore, the electron will drift forward longitudinally and in the reverse direction of the instantaneous vector potential at the time of ionization on the plane perpendicular to the laser propagation

axis. Note that the transverse momentum given by this treatment yields the same residual energy as Eq. (2.8) and (2.9) for the LP and CP cases respectively. To conserve the total linear momentum of the atom, the released ion gains the same amount of residual momentum (in the opposite direction) as the released electron, but its residual energy is much smaller than electron's due to the large mass difference.

2.2.3 Plasma sheath formation

A focused high-intensity laser pulse can generate a region of fully ionized plasma surrounded by a partially ionized plasma and neutral gas(es). Tunnel ionization increases drastically when the laser intensity approaches I_{BSI} of the given electron. Therefore, the ionized plasma will also have large density gradients at the boundary area. The electrons have higher thermal speed and tend to leave the plasma first. An electric field is built up when mobile plasma electrons diffuse into vacuum (or partially ionized region) and leave relatively immobile ions behind. This field slows down the loss of electrons and accelerate the ions. The layers of opposite electrical charge (also known as the double layer) can effectively constrain the plasma in its original volume on the time scale shorter than $L/c_s \sim 30$ ps, where L represents a characteristic length of an OFI plasma, $c_s \approx \sqrt{T_e/m_i}$ is the ion sound speed, T_e is the electron temperature and m_i is the mass of ion. We will refer this boundary structure as the plasma sheath in this work. The plasma will expand approximately at the speed c_s through the mechanism known as the ambipolar diffusion [63].

Fig. 2.3 shows the schematics of the plasma sheath structures of OFI hydrogen and helium plasmas shortly after the ionization is complete. In the hydrogen case (Fig. 2.3(a)), the sheath forms between the ionized hydrogen atom and neutral atom. While ions are effectively fixed, electrons spread outward and the electric field is set up. The electric field is able to reflect most of the electrons and keeps the bulk plasma region homogeneous. In the helium case (Fig. 2.3(b)), a two-step ionization structure is formed because of the ionization potential difference between the first and the second electron of helium. As we have shown in the previous section, this leads to a hotter central region and a colder boundary region.

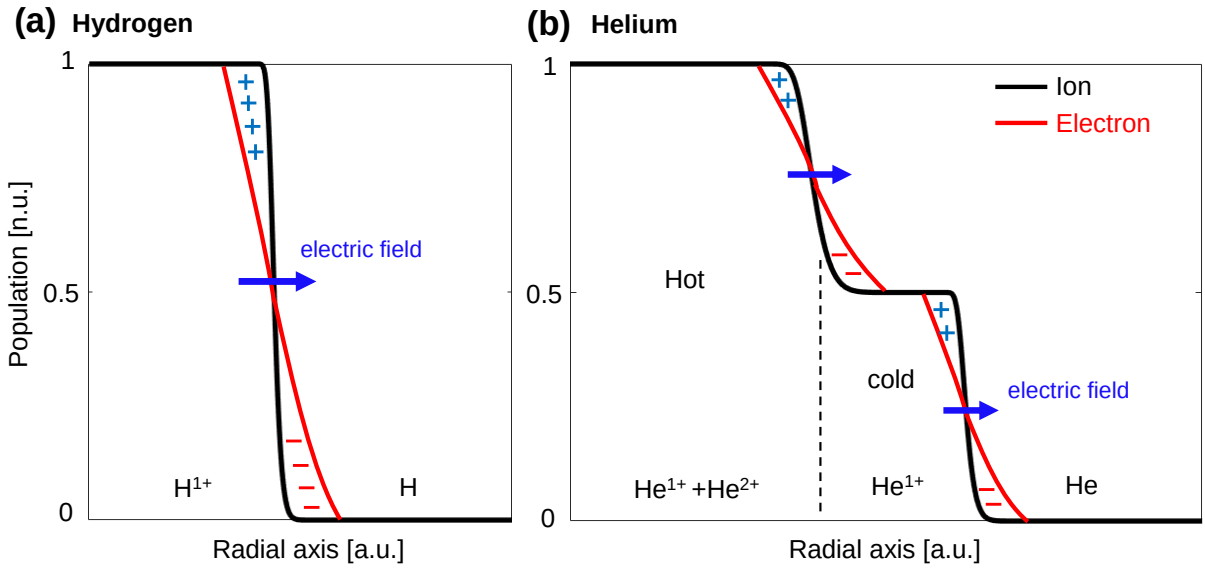

Figure 2.3: **Plasma sheath structures of OFI hydrogen and helium plasmas.** Metastable distributions of electrons and ions from OFI of (a) hydrogen and (b) helium. Double layers comprised of layers of positive charge (+) and negative charge (−) are located at the boundary regions between different ionic species.

The double-layer that separates these two regions will accelerate electrons from the cold region to the hot region and allow only the electrons with high velocity to penetrate from the hotter region. In this case, the sheath not only spatially confines the plasma but has a notable influence on the plasma distribution and electron dynamics.

2.3 Nonthermal EVDF of OFI plasmas

The energy and the direction of the ionized electron in OFI depends upon the details of the laser pulse(s) and the ionization state of the gas [2, 64, 60, 65]. As we have shown, the electrons are ejected along the reverse direction of the vector potential (in the direction of the electric field) upon ionization, therefore strongly non-thermal and/or anisotropic EVDF are produced in the resulting plasma. The EVDF of highly charged states produced by relativistic pulses ($a_0 \geq 1$) in a dense plasma are rather complicated because they can

be affected by numerous other physical effects such as wakefields/parametric instabilities [66, 67], direct energy exchange with the laser field [68] and therefore will not be considered here.

Just like the residual energy, the structure of the electron distribution in the transverse velocity space depends on the polarization of the ionizing laser. First of all, in the non-relativistic regime the electrons are considered to be cold in the direction of laser propagation. For the linear polarization (LP) case, the transverse EVDF are a combination of several groups of Maxwellian electrons associated with different ionic species. All group have hotter temperatures along the laser polarization and a similar cold temperature in the other direction. Assume a LP laser is polarized in x direction and propagates along z direction, the resultant EVDF can be written as

$$f_{e,\mathrm{LP}}(\mathbf{v}) = \frac{1}{Z}\left(\frac{m_e}{2\pi}\right)^{3/2} [n = 1]Z \sum \frac{1}{\sqrt{T_{n,x}T_{n,y}T_{n,z}}} \exp\left[-\frac{m_e}{2}\left(\frac{v_x^2}{T_{n,x}} + \frac{v_y^2}{T_{n,y}} + \frac{v_z^2}{T_{n,z}}\right)\right] \tag{2.11}$$

where $T_{n,x}$, $T_{n,y}$, are $T_{n,z}$ are the temperatures of the electrons from the nth electron group in the x, y, and z direction; and Z is the atomic number of the atom. In this case $T_{n,x} \gg T_{n,y}, T_{n,z}$. On the other hand, for the circular polarization (CP) case, transverse EVDF are initialized with ring structures (also can be considered as electron groups associated with different ionic species) because the vector potential rotates in the transverse plane. The EVDF from a CP laser propagating in z direction can be written as

$$f_{e,\mathrm{CP}}(\mathbf{v}) = \frac{1}{Z}\left(\frac{m_e}{2\pi}\right)^{3/2} [n = 1]Z \sum \frac{1}{\sqrt{T_{n,r}^2 T_{n,z}}} \exp\left[-\frac{m_e}{2}\left(\frac{2\left(v_r - v_{n,r}\right)^2}{T_{n,r}} + \frac{v_z^2}{T_{n,z}}\right)\right] \tag{2.12}$$

where $T_{n,r}$ is the thermal spread of the nth electron group in the radial direction and $v_{n,r}$ is the radial drift velocity of the nth electron group. The value of $v_{n,r}$ is decided by the ionization potential of the specific electron in the atom/ion.

EVDF of helium plasmas are computed by substituting various laser parameters into Eqns. (2.4), (2.5), and (2.6). We shall refer to the electron that ionizes first as the He^{1+}

electron and second as the He^{2+} electron. Fig. 2.4 shows the electron distribution along the laser polarization direction for the linear polarization case ($\sigma = 0$). The total distribution (blue curve) is the sum of two 1D Maxwellian distributions from He^{1+} electrons (dashed red curve) and He^{2+} electrons (dotted pink curve) with temperatures of 60 eV and 290 eV respectively. The temperatures in other directions (y and z) are both zero.

When $\sigma \neq 0$, the residual momentum distribution needs to consider the plane (v_x vs v_y) perpendicular to the propagation direction of the pump laser. Fig. 2.5 show the EVDF are changed with the ellipticity of the laser polarization. Here the value of the ellipticity, defined as the ratio of the major to minor axis of the polarization ellipse, is equal to $|\sigma|$. In the elliptical polarization (EP) cases (Fig. 2.5(a)-(c)), the EVDF show four lobes with the distribution in x much wider than that in y. Once again the He^{2+} electrons, which

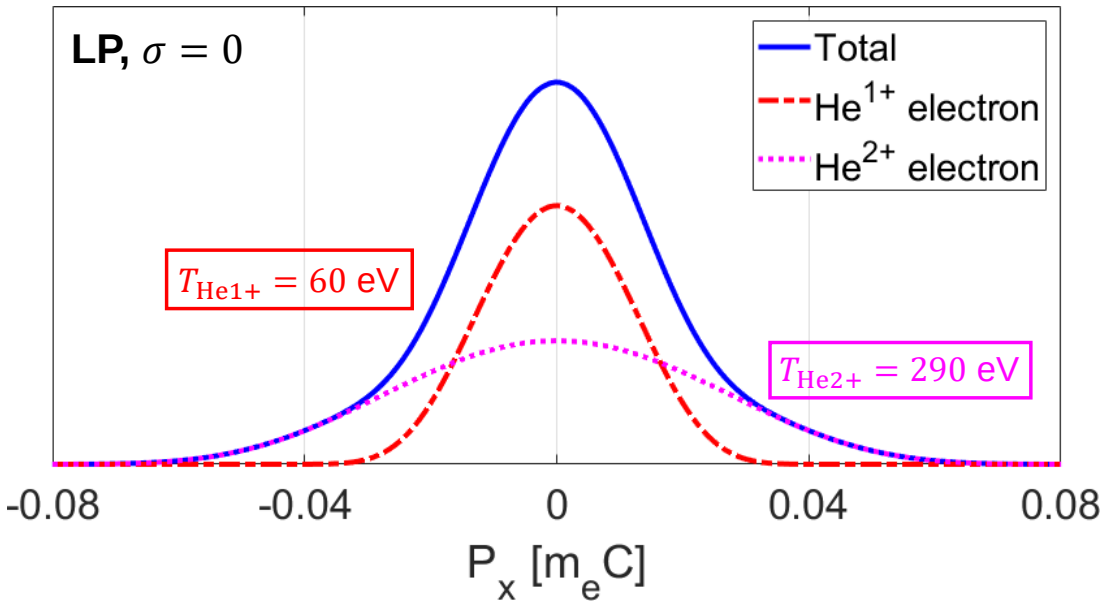

Figure 2.4: **EVDF for linear polarization case.** The 1D distributions of total electrons (blue), He^{1+} electrons (dashed red), and He^{2+} electrons (dotted pink) along the laser polarization, with the laser intensity of 1×10^{17} W/cm^2 and the pulse duration of 50 fs.

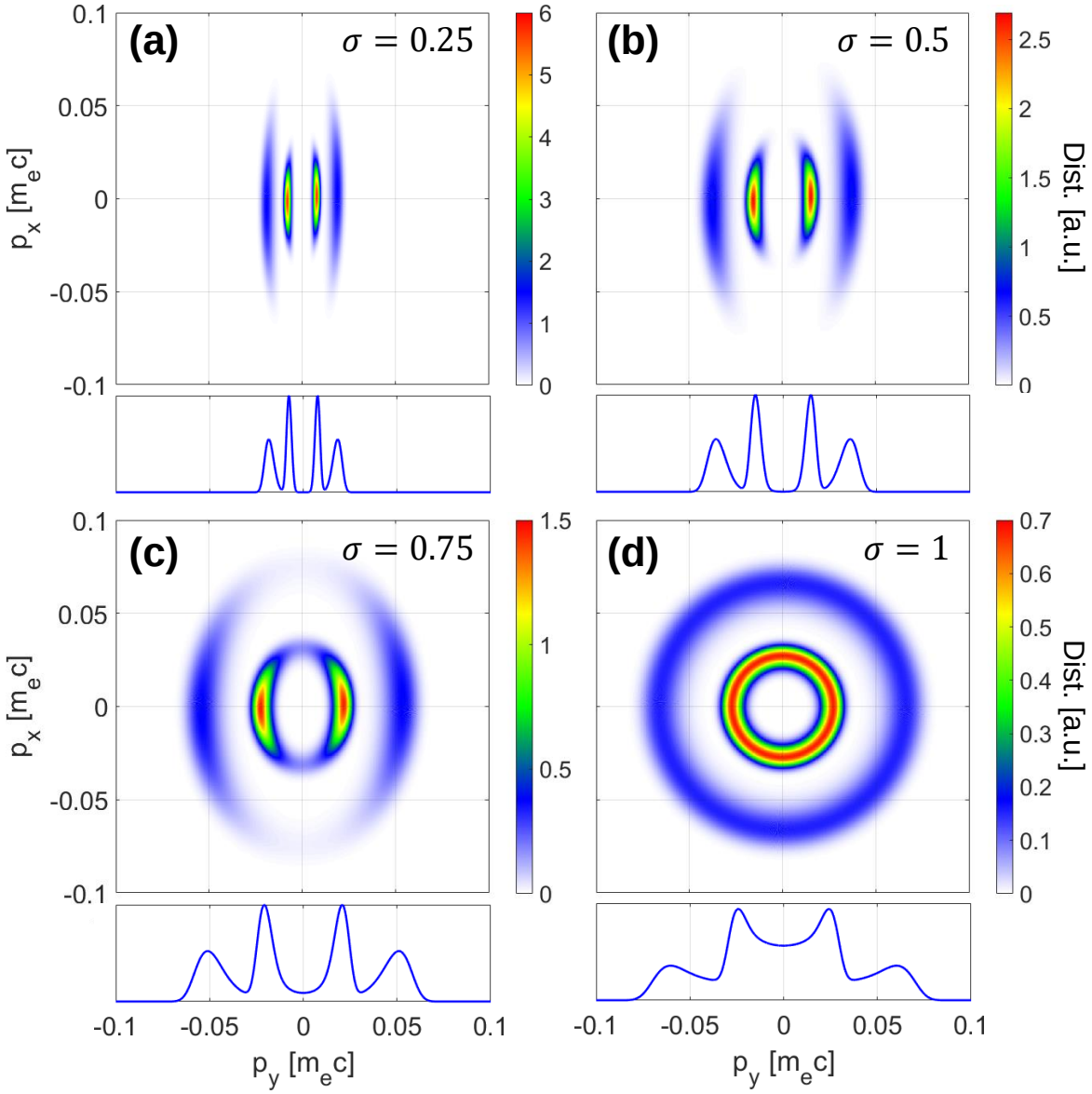

Figure 2.5: **EVDF from the pump laser with different polarization states.** 2D EVDF of He plasmas are calculated for laser pulses with ellipticity of (a) $\sigma = 0.25$, (b) $\sigma = 0.5$, (d) $\sigma = 0.75$, and (d) $\sigma = 1$. The 1D distribution along the y direction for each case is shown below the 2D distribution.

correspond to the outer lobes, are more energetic than He^{1+} electrons. In the CP case (σ = 1, Fig. 2.5(d)), electron distributions are donut-shaped in the x-y velocity space. In the x-y plane the resulting electron velocity distribution has four streams. The transverse streams in Fig. 2.5(a)-(c) and the radial streams in Fig. 2.5(d) have larger drift velocities than their thermal velocities. Kinetic theory predicts that plasmas with such distribution functions are susceptible to developing kinetic instabilities [13]. It is the relative drift between these streams that gives rise to the electron streaming and filamentation instabilities

2.4 Simulations of optical-field ionized helium plasmas

The simulations were performed using the 3D particle-in-cell (PIC) code OSIRIS [69], which self-consistently includes modules of ionization and other physical effects such as the ponderomotive force of the optical pulse, plasma kinetic effects, and wake formation. The configuration of the simulation is shown in Fig. 2.6. Here the x-y plane is perpendicular to the direction of propagation of the laser, z. The dimensions of the simulation box were $500 \times 280 \times 280\, c/\omega_0$ ($63.6 \times 35.6 \times 35.6$ μm) in the z, x and y directions. The box was divided into $2500 \times 560 \times 560$ cells. Eight particles with a quadratic shape were initialized in each cell. A 50-fs (FWHM), 800 nm laser with a $\sin^2$ intensity profile was injected from the left wall of the simulation box and propagated to the $+z$ direction. The laser pulse had a Gaussian radial intensity profile with a spot size of 8 μm. The peak intensity of the laser was 1.6×10^{17} W/cm^2 , which gives a normalized vector potential $a_0 = 0.19$ (CP) and $a_0 = 0.27$ (LP). Transversely uniform helium gas was initialized inside the box with a longitudinal profile that increases linearly from zero at $z = 10\, c/\omega_0$ to 2.5×10^{18} cm^{-3} at $z = 20\, c/\omega_0$ and then remains flat before decreasing linearly from the peak density at $z = 490\, c/\omega_0$ to zero at $z = 500\, c/\omega_0$. The ionization of the helium gas in OSIRIS was modeled using the ADK theory, and for the most simulations, the ions were immobile.

In Fig. 2.7 we show four examples of EVDF in velocity space from OSIRIS simulations of fully ionized, dense (5×10^{18} cm^{-3}) He plasmas. The simulation results self consistently take

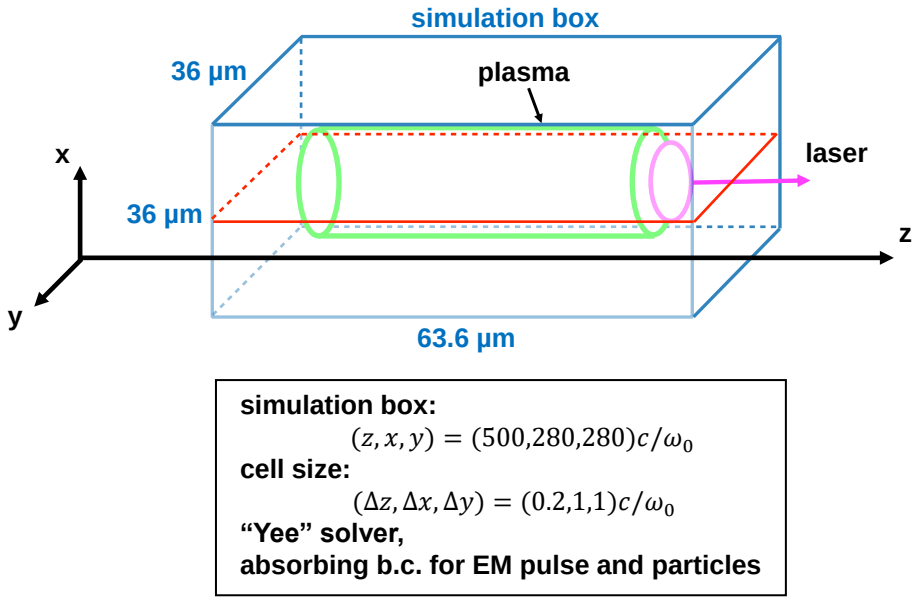

Figure 2.6: **Configuration of the simulations**

into account space charge effects, any onset of collective effects and sheath effects discussed earlier. The electrons used to generate the EVDF are those within a z = 2-μm-wide slab around the focal position of the laser at the time 300 fs after the laser had passed. The reason for choosing a later time in the simulation box is so that the simulated EVDF can be compared with the experimental results, which will be discussed in the next chapter. In these four cases, the He^{1+} electrons are ionized early during the risetime of the laser pulse within a few laser cycles and the He^{2+} electrons are ionized approximately 10 fs after the first He electron. These electrons have both transverse (x and y) and longitudinal (z) oscillating energy of a few eV due to a weak linear wake formed by the laser pulse [66] and the ions are essentially cold in all directions.

Fig. 2.7(a) shows that the initial electron distribution from a LP laser. The EVDF along the laser polarization direction (y) can as well described by a sum of two 1D (near) Maxwellian distributions to the calculated spectrum shown in Fig. 2.4. Two temperatures that fit these distributions are 60 eV (He^{1+}) and 210 eV (He^{2+}). Comparing this with the

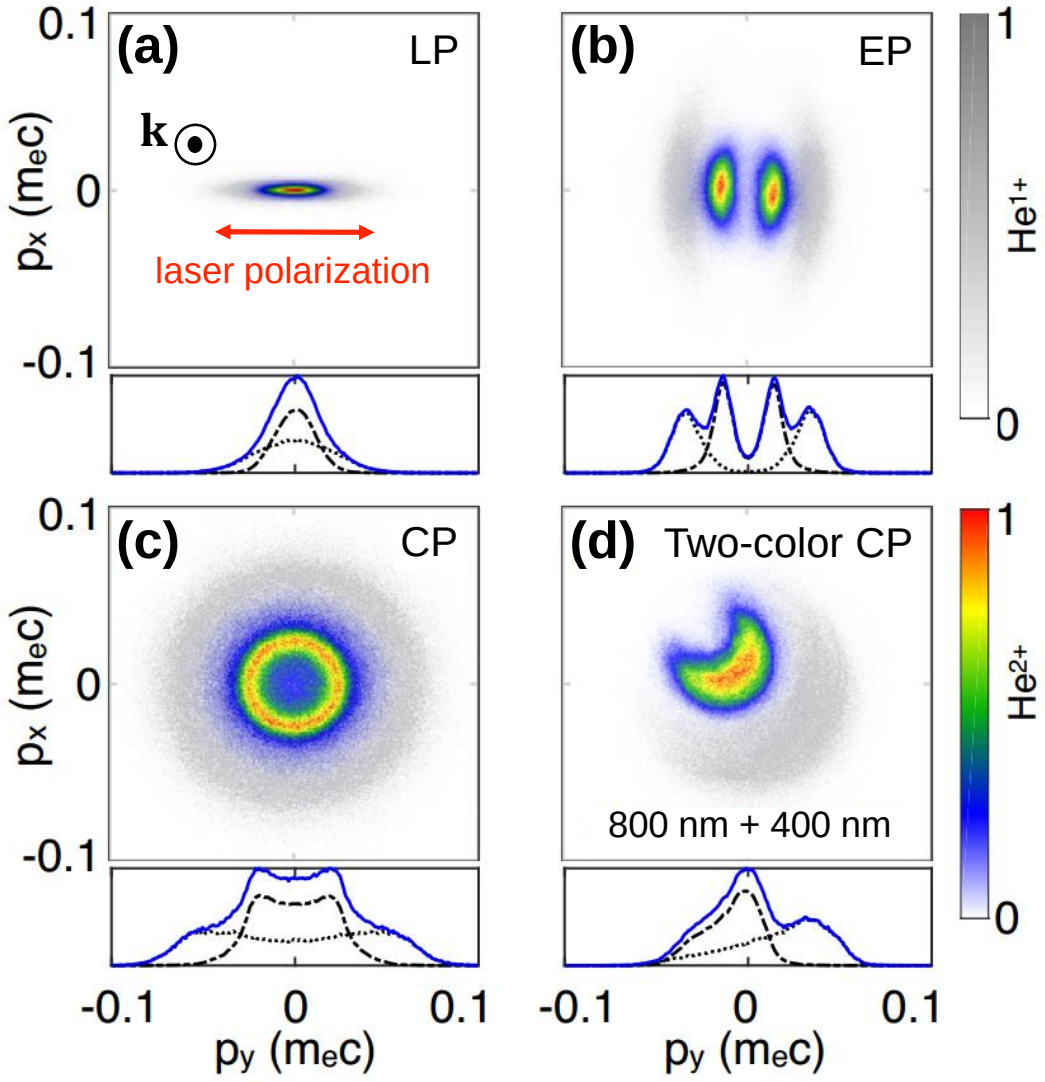

Figure 2.7: **Simulated EVDF:** (a)–(c) Examples of simulated electron velocity distributions using OSIRIS of He plasmas produced by 50 fs, 800 nm laser pulses with peak intensity of 1.6×10^{17} W/cm^2 and different polarizations (linear, elliptical, circular respectively). (d) Circular, 800 nm, 3×10^{16} W/cm^2 + circular, 400 nm, 1×10^{16} W/cm^2 with the same initial phase. Also shown below each v_x-v_y image is the v_y distribution (the sum of the number of particles at each v_y) for He^{1+} electrons (dashed green curve), He^{2+} electrons (dotted black curve) and their sum (solid blue line).

calculation shown in Fig. 2.4, we see a temperature drop for He^{2+} electrons and a small but finite temperature ($\sim$ 12 eV) in the x direction. In the elliptical polarization (EP) case (σ = 0.5, (Fig. 2.7(b)) the EVDF shows four lobes in P_y which can be approximated by four Maxwellian streams in the y direction. The width of each stream is larger than the calculated results. In the CP case (Fig. 2.7(c)), the existence of electrons close to zero transverse velocity suggests that the plasma has already evolved significantly by the end of the laser pulse, due to plasma collective effects. The overall initial electron distribution in the circular case is also shown in Fig. 2.7(c), blue curve. It indicates a highly non-Maxwellian distribution with much hotter root-mean-square (rms) temperature of $\sim$ 470 eV (220 eV and 910 eV for the He^{1+} and the He^{2+} electrons respectively). The simulated EVDF for the LP, EP, and CP cases (Fig. 2.7(a)-(c)) have similar characteristics (shapes) with the calculated ones (Fig. 2.4 and 2.5), but display diffusions in momentum space possibly caused by the boundary sheaths effect and plasma kinetic effects that are included in simulations. In Fig. 2.7(d) a two frequency CP laser pulse with different intensities generates a bump-on-tail distribution that would lead to spontaneous generation of plasma waves via inverse Landau damping.

2.5 Designer distribution functions

The OFI plasma is ideally suited for generating designer distribution functions using machine leaning/use of genetic algorithms. We will not demonstrate a case of specifying a true designer distribution function and use the above mentioned techniques to converge on the closest solution. Instead we will demonstrate the capacity of OFI plasmas for generating some unusual EVDF. In principle, a great many types of distributions may be achievable by multiple pulses with combinations of different laser polarizations, wavelengths, intensity profiles, and ionizing media. Asymmetrical two-dimensional momentum distributions have shown to be generated by ionizing atoms with two-color circularly polarized laser pulses [65] and orthogonal two-color laser pulses [64]. We have shown one example from the simulation in Fig. 2.7(d) whose characteristic distribution could be used for testing a plasma theory.

Different types of EVDF may be needed for various plasma theories.

Examples of calculated 2D EVDF from OFI hydrogen plasmas are shown in Fig. 2.8 by using two pulses with different polarizations, wavelengths, or relative phase. Fig. 2.8(a) shows the same type of electron distribution in reference [64] using superimposed, orthogonally polarized two-color LP pulses. The details of the distribution depend on the exact relative phase between two pulses. Fig. 2.8(b) and (c) show two cases of superimposed orthogonal linear polarized lasers with different wavelengths and a relative phase between two pulses. The X-shaped structure appears as the result of the complicated trajectories of the local vector potential. When two superimposed lasers have well-separated wavelengths, the distribution is the sum of contributions from each pulse. This is the case shown in Fig. 2.8(d). Fig. 2.8(e) and (f) show that by combining two colors with different polarizations and relative phases, various types of EVDF are initialized. From the above examples, it is clear other "designer" EVDF are possible by optimization of laser and choice of the ionizing medium. However, practical applications are limited by available laser parameters. With the advent of free electron lasers, currently unavailable parameters may be realized in the near future.

Figure 2.8: **Examples of various distribution functions.** (Next page) Calculations of 2D EVDF produced in OFI hydrogen plasmas by superimposing of two 50-fs (1 ps for 4 μm) pulses with various parameters. The table above each image of distribution shows the parameters (polarization, wavelengths, relative phase) of two laser pulses.

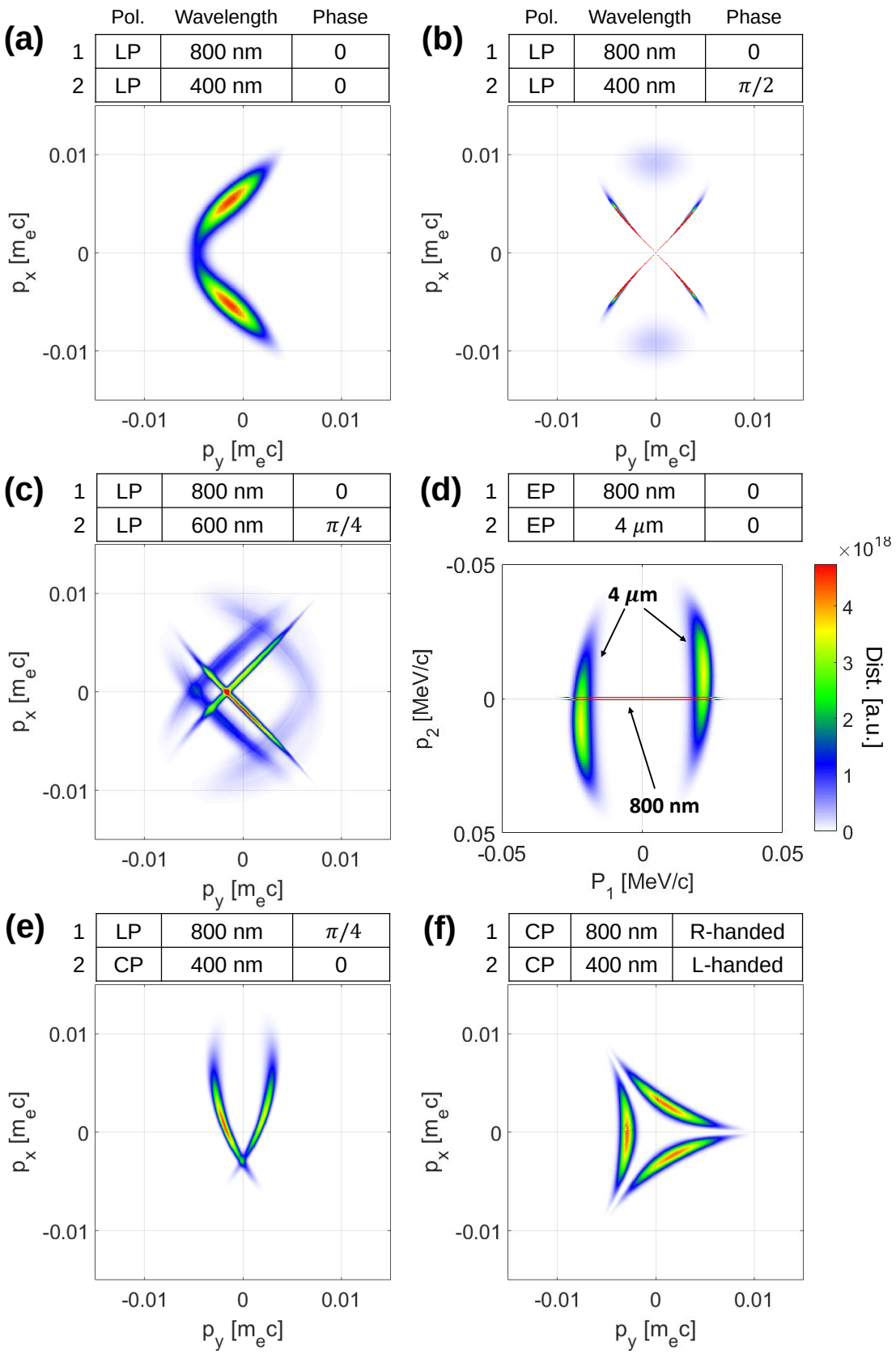
(a)
Pol. Wavelength Phase
1 LP 800 nm 0
2 LP 400 nm 0
(b)
Pol. Wavelength Phase
1 LP 800 nm 0
2 LP 400 nm $\pi/2$
(c)
1 LP 800 nm 0
2 LP 600 nm $\pi/4$
(d)
1 EP 800 nm 0
2 EP 4 μm 0
4 μm
800 nm
$\times 10^{18}$
Dist. [a.u.]
(e)
1 LP 800 nm $\pi/4$
2 CP 400 nm 0
(f)
1 CP 800 nm R-handed
2 CP 400 nm L-handed
p_x [$m_e c$]
p_y [$m_e c$]
p_2 [MeV/c]
P_1 [MeV/c]

CHAPTER 3

Measuring the Initial Electron Velocity Distribution Functions of OFI He Plasmas

Plasmas with controllable distribution functions are crucial for investigating kinetic plasma instabilities in the laboratory. As explained in the Chapter 2, initial electron velocity distributions function (EVDF) can be controlled by OFI process. Momentum distribution of photoelectrons or ions produced by strong field ionization are extensively studied within the scope of atomic physics. Velocity map imaging [70] has been used to directly map the momentum distribution of emitted electrons or ions but this technique is limited to extremely low densities where collisional (Coulomb) and collisionless (collective) interaction between electrons is negligible. In this case, the electrons and ions move to the detector without interacting with other particles. However, for relatively dense OFI plasmas ($n_e > 10^{17}$ cm^{-3}), most ionized electrons and ions are bounded by the sheath field formed at the plasma-vacuum boundary. This system is subject to collective dynamics of charged particles within the plasma body. Therefore, a different approach is required to measure the distribution in the bulk of the plasma. Using the scattering of electromagnetic radiation from the plasma is one of the most powerful method of plasma diagnostics [71, 72]. In the classical limit ($h\nu_{\mathrm{pr}} \ll m_e c^2$ where h is the Planck constant and ν_{pr} is the frequency of the probe wave), this method is called Thomson scattering (TS). It is intrinsically nonperturbing and provides the potential of determining detailed information about the EVDF.

In this chapter, we experimentally show the OFI-controlled distribution by using Thomson scattering as a diagnostic to probe the characteristic electron velocity distributions using linearly and circularly polarized laser pulses to ionize helium gas. The measurement of the

EVDF is difficult because plasmas can very quickly develop kinetic instabilities. These collisionless processes tend to isotropize the initially produced EVDF on a timescale far shorter than electron-electron collisions alone, estimated to be tens of ps for plasma density in the range of 10^{17}-10^{18} cm^{-3} and expected values of $T_\perp/T_\parallel$, where $T_\perp$ and $T_\parallel$ are the plasma temperatures in directions perpendicular and parallel to the propagation of the laser. The detailed mechanisms and growth rates of these kinetic instabilities will be discussed in the next chapter, but their effects can nevertheless be observed in the experiments mentioned here. A short-pulse ($\sim$ 90 fs) Thomson scattering technique is developed to interrogate the short-lived EVDF just $\sim$ 300 fs after ionization is completed. During such a short time period plasma density evolution due to expansion or recombination can be neglected.

3.1 Short-pulse Thomson scattering

3.1.1 Physics of Thomson scattering

Thomson scattering is essentially the electromagnetic radiation emitted by free electrons that are accelerated by the field of the incident electromagnetic wave. For an electron initially at rest, the emitted radiation is at the same frequency of the incident wave. If the free electron has an initial velocity, a stationary observer may observe a frequency shift of the emitted radiation due to the Doppler effect. This effect can be used to determine the velocity distribution of free electrons. In the case of high-density plasmas, however, the correlations between particles usually have to be taken into considerations. Due to the mass difference between the electron and ion, the radiation from ion motion is usually not significant but the information about plasma ions, in particular the ion and electron temperature can still be measured from the small but measurable frequency shifts due the effects ions have on the electrons.

Consider a probe beam (with average power $P_{\rm pr}$, electric field $\boldsymbol{E}_{\rm pr}$, wave vector $\mathbf{k}_{\rm pr}$, and freqency $\omega_{\rm pr}$) scatters from a volume V that contains on the average N electrons, the scatterd power measured from the wave vector $\boldsymbol{k}_{\rm s}$ in the frequency range $[\omega, \omega + d\omega]$ and solid angle

$d\Omega$ is

$$\frac{d^2P_s(\mathbf{k},\omega)}{d\omega d\Omega} = P_{pr} r_e^2 \frac{n_0 L}{2\pi}\left(1+\frac{2\omega}{\omega_{pr}}\right)\left|\hat{\mathbf{k}}_s \times \left(\hat{\mathbf{k}}_s \times \hat{\mathbf{E}}_{pr}\right)\right| S(\boldsymbol{k},\omega) \tag{3.1}$$

where $\mathbf{k} = \mathbf{k}_s - \mathbf{k}_{pr}$, $n_0 = N/V$ is the averaged electron density, L is the length of the scattering volumn, $r_e = e^2/m_e c^2 = 2.82\times10^{-13}$ cm is the classical electron radius, and $S(\boldsymbol{k},\omega)$ is known as the spectral density function (SDF) or the form factor. The SDF is the ensembled average of the Fourier transform of the fluctuating electron density $n_e(\boldsymbol{r},t)$,

$$S(\mathbf{k},\omega) = \lim_{V,T\to\infty}\frac{1}{VT}\left\langle\frac{|n_e(\mathbf{k},\omega)|^2}{n_0}\right\rangle \tag{3.2}$$

Except for a small factor $\left(1+2\omega/\omega_{pr}\right)$, the shape of measured power spectrum is fully determined by SDF, so Eq. (3.2) is generally used in fitting TS spectra to extract information about the plasma. For a non-relativistic, unmagnetized plasma with an electron distribution function $f_e(\mathbf{v})$ and ion distribution functions $f_{i,j}(\mathbf{v})$ for ionic species j, Eq. (3.2) can be calculated considering a finite scattering volume and time [72] and written as

$$S(\mathbf{k},\omega) = \frac{2\pi}{k}\left|1-\frac{\chi_e}{\epsilon}\right|^2 f_e\left(\frac{\omega}{k}\right) + \sum_j \frac{2\pi Z_j^2 N_j}{kN}\left|\frac{\chi_e}{\epsilon}\right|^2 f_{i,j}\left(\frac{\omega}{k}\right) \tag{3.3}$$

where Z_j is the charge of the jth ion, N_j is the number of jth ion, $\epsilon = 1+\chi_e+\sum_j \chi_{i,j}$ is the dielectric function, χ_e and $\chi_{i,j}$ are the electron and ion susceptibilities

$$\chi_e(\mathbf{k},\omega) = \frac{4\pi e^2 n_0}{m_e k^2}\int_{-\infty}^{\infty} d\mathbf{v}\frac{\mathbf{k}\cdot\partial f_e/\partial\mathbf{v}}{\omega-\mathbf{k}\cdot\mathbf{v}} \tag{3.4}$$

$$\chi_{i,j}(\mathbf{k},\omega) = \frac{4\pi Z_j^2 e^2 n_{i,j}}{m_{i,j} k^2}\int_{-\infty}^{\infty} d\mathbf{v}\frac{\mathbf{k}\cdot\partial f_{i,j}/\partial\mathbf{v}}{\omega-\mathbf{k}\cdot\mathbf{v}} \tag{3.5}$$

where $m_{i,j}$ and $n_{i,j}$ are the ion mass and density of the jth species. The first term on the right-hand side of Eq. (3.3) is called the electron feature because it depicts the plasma electron response to fluctuations; the second term corresponds to the electrons in the cloud surrounding the ions, and is therefore called the ion feature. Calculating the SDF using

Eq. (3.3) is usually not trivial due to poles in χ_e and χ_i, except for some special cases. A common case is when electrons and ions both have Maxwellian distributions, the SDF can be expressed by the plasma dispersion function $Z(\xi) = \pi^{-1} \int_{-\infty}^{\infty} \frac{e^{-t^2}}{t-\xi} dt$ [73]. A code to calculate SDF for a Maxwellian plasma is shown in Appendix D.

Whether the scattering spectrum demonstrates the collective plasma effects depends on the plasma parameters and the wavelength of the fluctuation. It is convenient to introduce the Thomson scattering parameter

$$\alpha = \frac{1}{k\lambda_{\mathrm{De}}} \approx \frac{1.08 \times 10^{-4} \lambda_{\mathrm{pr}}\,[\mathrm{cm}]}{\sin(\theta_{\mathrm{s}}/2)} \sqrt{\frac{n_0\,[\mathrm{cm}^{-3}]}{T_{\mathrm{e,eff}}\,[\mathrm{eV}]}} \tag{3.6}$$

where λ_{De} is the Debye length of the plasma electrons, λ_{pr} is the probe laser wavelength, θ_{s} is the scattering angle defined by the angle between the incident laser and the direction of the collected light $\hat{\mathbf{k}}_s$, and $T_{\mathrm{e,eff}} \sim m_e \langle v_e^2 \rangle$ is the effective electron temperature.

In the limit $\alpha \ll 1$, i.e. $2\pi/k \ll \lambda_{\mathrm{De}}$, then $\chi_e \ll 1$ so the first term is dominant in Eq. (3.3). The total scattered power can be obtained as the sum of scattered powers from single electrons. The SDF will be an accumulation of the Doppler shifted photons from each electron and therefore reflects the velocity distribution function of plasma electrons. Spectral density function in this so-called "non-collective regime" can simplified to

$$S(\mathbf{k}, \omega) \simeq \frac{2\pi}{k} f_e\left(\frac{\omega}{k}\right) \tag{3.7}$$

When $\alpha > 1$, the characteristic length of the collective disturbance is larger than the Debye length, the correlation between particles can not be ignored and the scattering is in the collective regime. For a plasma at its natural resonance, the high-frequency electron plasma resonance will be maximized at the frequency decided by the Bohm-Gross relation

$$\omega_{\mathrm{BG}}^2 \simeq \omega_{\mathrm{pe}}^2 + \frac{3k_{\mathrm{B}}T_e}{m_e} k^2 \tag{3.8}$$

where ω_{BG} is the Bohm-Gross frequency, ω_{pe} is the electron plasma frequency and k_{B} is the Boltzmann constant. In the low-frequency regime, the spectral peak of the ion feature is

associated with the ion-acoustic wave when $ZT_e/T_i \gg 1$ where T_e and T_i are the electron and ion temperature. Otherwise, ion waves would be strongly damped by ion Landau damping and the scattering spectrum reflects the ion thermal spread.

Fig. 3.1 show how the theoretical TS spectrum changes with electron temperatures for a 400-nm probe at a fixed plasma density, scattering angle, and ion temperature. When the electron temperature is small and $\alpha > 1$, a spectrum with two peaks at Bohm-Gross frequency can be seen. As the electron temperature increases, α decreases and the regime of TS changes from the collective to non-collective. When α is small enough, the spectral distribution becomes close to a Maxwellian distribution. In the calculated spectra shown in Fig. 3.1, the spectral shift of ion feature is about 0.1 nm when the room temperature ions are assumed. Because of the large difference between the resonant frequencies of the electrons and ions, separated setups and spectrometers with different spectral resolutions are generally required in experiments targeting both the electron and ion features in the collective scattering regime.

Collective Thomson scattering is also an effective tool to diagnose the characteristics of the plasma instabilities.When the plasma is far away from thermal equilibrium, the free energy of the system may be large enough to drive unstable modes. The turbulences or fluctuations whose characteristic lengths are larger than the Debye length can be detected by Thomson scattering. For an unstable mode that grows to a large amplitude in a plasma, the SDF is enhanced to well above the thermal level at certain angle (the measured wavevector matches the unstable wave). In this case, the collective features of TS are decided by the dispersion relation of the unstable wave. The usage of the collective Thomson scattering in studying kinetic instabilities arisen from OFI plasmas will be discussed in Chapter 4.

3.1.2 Thomson scattering from non-Maxwellian and anisotropic EVDF

As discussed in Chapter 2, the initial condition of an OFI plasma is nonthermal and anisotropic. Thomson scattering of these plasmas should consider the angle between the anisotropy and the measured wave vector $\mathbf{k}_\mathrm{m} = \mathbf{k}_\mathrm{s} - \mathbf{k}_\mathrm{pr}$ [74]. For the LP case, EVDF are the sum of

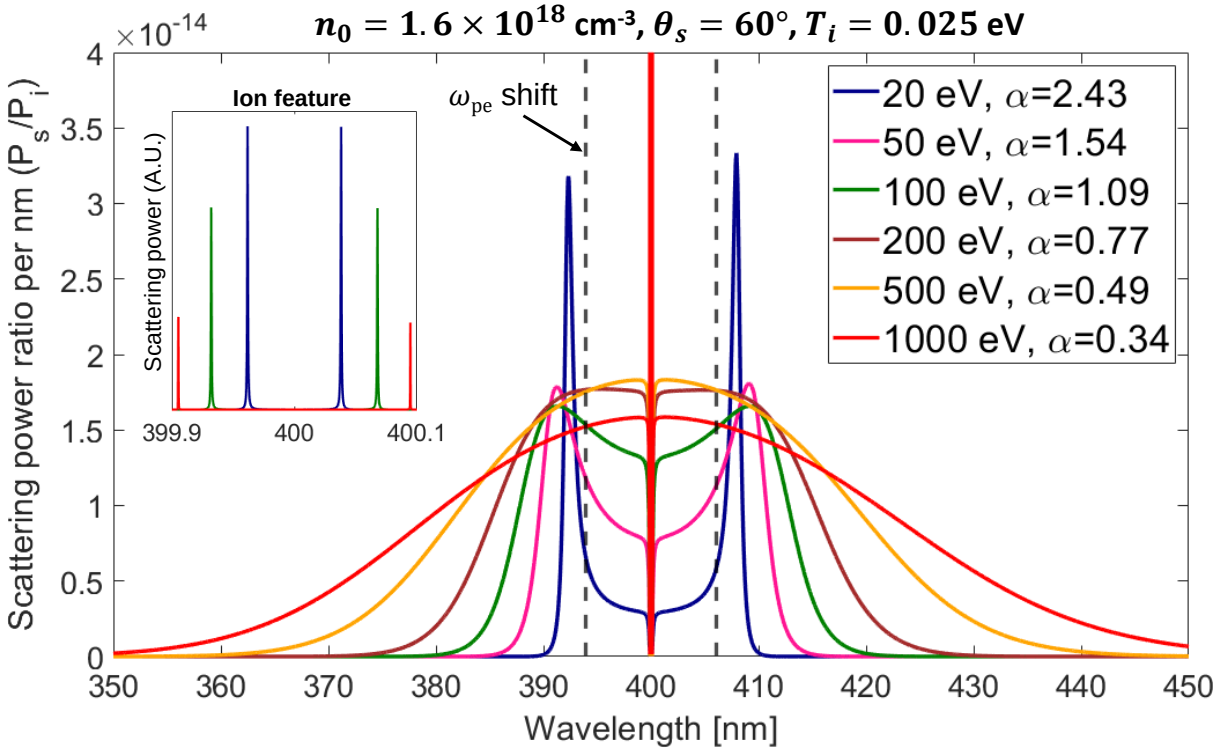

Figure 3.1: **Thomson scattering spectra for a range of scattering parameters.** For a fixed plasma density ($n_0 = 1.6 \times 10^{18}$ cm^{-3}), scattering angle ($\theta_s = 60°$), and probe laser wavelength ($\lambda_{pr} = 400$ nm), Maxwellian electron distributions with different temperatures have different values of α, where α is the Thomson scattering parameter. Thermal ions at room temperature ($T_i = 0.025$ eV) are included in calculations, but two peaks of the ion feature are not distinguishable in the figure. The ion features of some cases are shown in the expanded sepectrum (inset).

anisotropic Maxwellian electron velocity distributions with different temperatures as shown by Eq. (2.11). The temperature seen by the TS diagnostics are the projection of individual components in velocity space on the measured wave vector. Assume $\mathbf{k}_\mathrm{m} = |\mathbf{k}_\mathrm{m}|\,(\sin\vartheta\cos\varphi, \sin\vartheta\sin\varphi, \cos\vartheta)$, the measured temperature for electron group n is

$$T_{\mathrm{m},n} = T_{n,x}\sin^2\vartheta\cos^2\varphi + T_{n,y}\sin^2\vartheta\sin^2\varphi + T_{n,z}\cos^2\vartheta \tag{3.9}$$

where ϑ is the polar angle and φ is the azimuthal angle of $\mathbf{k}_\mathrm{m}$. For the CP case, transverse electron velocity distributions are the sum of electron groups with a ring structure as shown by Eq. (2.12). These EVDF are highly non-Maxwellian and not able to be described by Maxwellian temperatures as Eq. (3.9). Nevertheless, the spectral density function (SDF) should be calculated for the one-dimensional projection of the EVDF on $\mathbf{k}_\mathrm{m}$.

In principle, SDF can be calculated using Eq. (3.3) for arbitrary electron and ion distribution functions, although analytical results are not generally available. For an non-Maxwellian electron distribution function that can be well-approximated by the sum of different distributions, it is possible to treat different groups (with different distributions) of electrons the same way as different ion species by rewriting Eq. (3.3) as

$$S(\mathbf{k}_\mathrm{m},\omega) = \frac{2\pi}{k}\left|1-\frac{\chi_e}{\epsilon}\right|^2\sum_n\frac{N_n}{N}f_{e,n}\left(\frac{\omega}{k}\right) + \sum_j\frac{2\pi Z_j^2 N_j}{kN}\left|\frac{\chi_e}{\epsilon}\right|^2 f_{i,j}\left(\frac{\omega}{k}\right) \tag{3.10}$$

where

$$\chi_e = \textstyle\sum_n \chi_{e,n} \text{ and } \chi_{e,n} = \dfrac{4\pi e^2 n_0 N_n}{m_e k^2 N}\displaystyle\int_{-\infty}^{\infty} d\mathbf{v}\frac{\mathbf{k}\cdot\partial f_{e,n}/\partial\mathbf{v}}{\omega-\mathbf{k}\cdot\mathbf{v}}$$

where $N = \sum_n N_n$, N_n is the number of electrons in the nth electron group, and $f_{e,n}(v)$ is the velocity distribution for the nth electron group. When the OFI plasma is comprised of the several groups of Maxwellian electrons with different temperatures (such as in the LP case), its $S(\mathbf{k},\omega)$ can be calculated in the similar way as a Maxwellian plasma. A code for calculating SDF for Maxwellian electron groups is shown in Appendix D.

3.1.3 Characteristics of the short-pulse probe

Probing of the initial EVDF of an OFI plasma must be done within a very short time window (< 500 fs) after the plasma is initialized. On one hand, an OFI plasma is non-equilibrium, so there may be rapidly developing unstable modes that become dominant in a TS measurement. On the other hand, the probe should not overlap with the pump pulse, otherwise the probed electron velocity distribution will be modulated by the pump field. To achieve a precise temporal control, the probe beams in all our experiments are either directly separated from or generated by frequency doubling of the pump pulse. Aside from this critical timing issue, there are other requirements for the probe:

1. A shorter pulse duration is preferred as we want the state of the plasma unchanging during the time period being probed. It is important since the OFI plasma is volatile especially in the CP case.

2. The spectral bandwidth should be narrow enough to resolve the characteristics features of TS spectra.

3. The probe should have high enough power to generate enough scattered photons. However, the probe intensity has to be restrained from a strong perturbation of the plasma.

4. The plasma should be homogeneous within the scattering volume.

Since the requirement 1 and 2 (also partially 3) are mutual exclusive, a trade-off must be made when choosing the parameters of the probe. A 400-nm pulse converted from a 50-fs 800-nm pump pulse is used as the probe to optimize the bandwidth and the pulse duration. To fulfill the requirement 4, collinear pump-probe geometry is selected to ensure the probe beam (focused tighter than the 800 nm pump) overlay with the fully ionized region (which is considered homogeneous). The spectral bandwidth of the 400 nm probe is measured to be ~ 3.4 nm, which is relatively large compared with conventional TS probes. Therefore, we applied a special treatment (discussed in Section 3.3.2) to compensate the broadening due to the large probe bandwidth. The effects of the second harmonic generation, the dispersion and

the group delay between the pump and the probe pulses were calculated using a simulation software SNLO [**?**]. The simulation shows there is nearly no change of the pulse shape for the pump beam in the case of a 12 mJ, 50 fs (FWHM), 800 nm input. The second-harmonic beam generated in a 1.5-mm-thickness potassium dideuterium phosphate (KDP) crystal from this pump beam has a pulse energy of ~ 1.5 mJ and the pulse duration of 90 fs (FWHM). The group delay between the 800 nm pump beam and the 400 nm probe beam is estimated to be 300 fs.

3.2 Collinear pump-probe setup for measuring initial EVDF

The experimental setup is shown schematically in Fig. 3.2. The plasma was formed by ionizing a static fill of He gas at various pressures by focusing a 800 nm, ~ 50 fs (FWHM) duration laser pulse containing ~ 10 mJ energy. The laser was focused by a gold-coated off-axis parabolic mirror (OAP) to a spot size $2w_0$ of 16 μm giving a peak intensity of $\sim 1\times10^{17}$ W/cm^2. The ~ 1 mJ, ~ 90 fs (FWHM), 400 nm probe beam was focused by the same OAP and focused to an even smaller spot size within the fully ionized plasma. Thomson scattered light was collected at 60° with respect to (w.r.t.) the incident pulse by a one-to-one imaging system that relays image of the central part of the plasma to the entrance slit of the spectrograph. The imaging system for collecting the scattering light confines the collection volume to be about $20\,\mu\text{m} \times 20\,\mu\text{m} \times 200\,\mu\text{m}$.

The plane containing the incident probe wave vector ($\mathbf{k}_{\text{pr}}$) and the scattered light wave vector ($\mathbf{k}_{\text{s}}$) is referred to as the scattering plane. Two polarization configurations for linearly polarized pump beams are the polarization direction parallel ($L_{\parallel}$) or perpendicular ($L_{\perp}$) to the scattering plane. The $L_{\parallel}$ ($L_{\perp}$) polarization allows us to independently probe the EVDF essentially along the v_y (v_x) directions. There is only one configuration for circular polarization (C) since the "double donut" EVDF generated is transversely isotropic. The 60° scattering angle determines the measured wave vector ($\mathbf{k}_{\text{m}}$) in this experiment as depicted in Fig. 3.2. The spread of due to collection solid angle is about 3% of $|k_{\text{s}}|$, small enough to assume $k_{\text{m}} \approx 2k_{\text{pr}} \sin(\theta_{\text{s}}/2)$ where θ_{s} is the scattering angle.

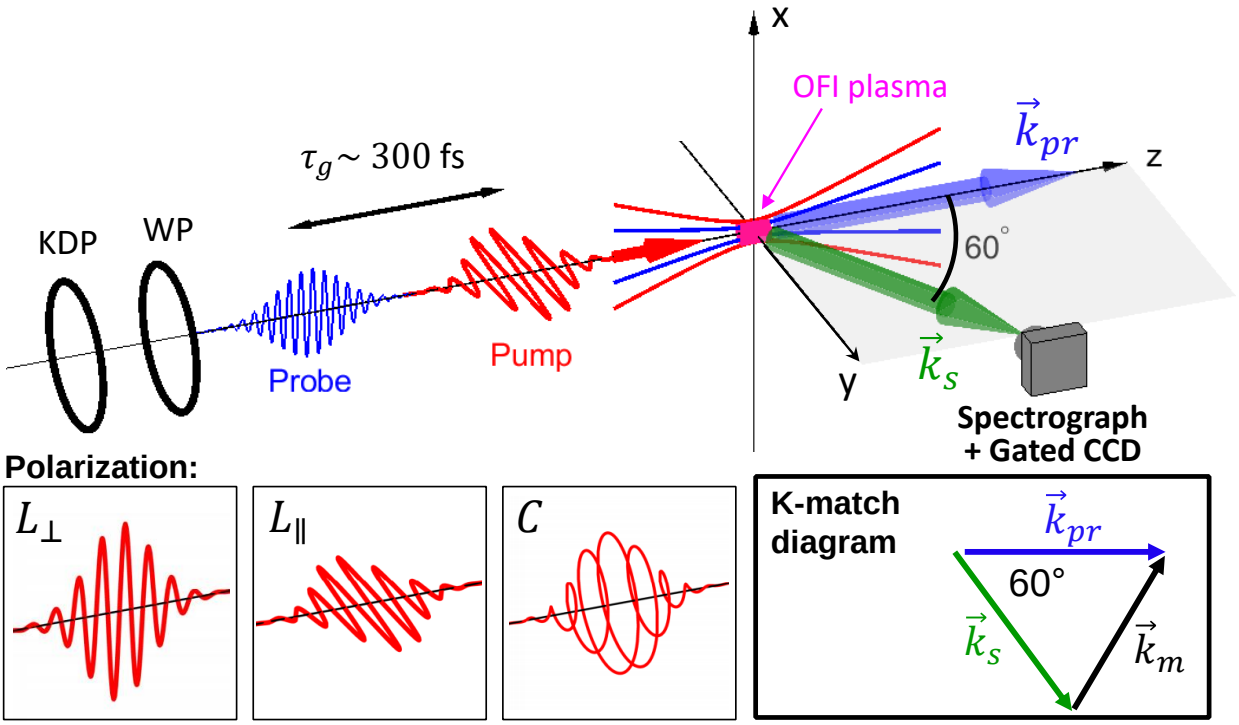

Figure 3.2: **Schematic of the collinear TS experiment:** The 800 nm pump beam generates OFI plasmas that are probed by a collinear 400 nm Thomson scattering beam using a fixed delay: linear polarization perpendicular to the scattering plane ($L_\perp$), parallel to the scattering plane ($L_\parallel$) and circular polarization (C). Also shown is the k-matching diagram where the vectorkm is probed in Thomson scattering. KDP: KDP crystal; WP: half-wave plate for linear polarization or quarter-wave plate for CP.

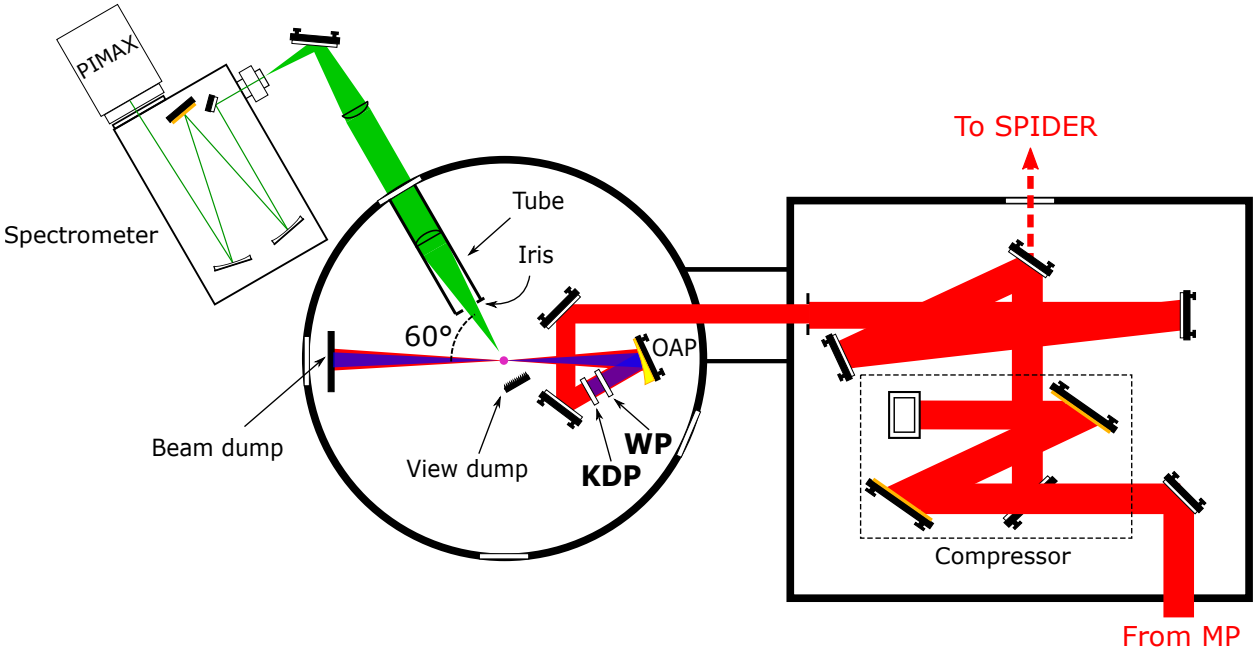

Figure 3.3: **Layout of the collinear TS experiment:** The pump beam (red) from the multipass (MP) amplifier is compressed and sent to the target chamber filled with helium gas. A small portion of the pump is separated by a beam splitter and sent to a commercial SPIDER. The probe beam (blue) is produced at the KDP crystal before it is focused by a gold OAP. The scattered light (green) is collected by an imaging system and sent to the spectrometer. Stray light control is carried out by setting the beam dump, view dump and the black tube in the collection system.

Figure 3.3 shows a detailed layout of the experiment, where the red, blue and green lines stand for the 800 nm pump beam, the 2ω probe beam, and the collected scattering light respectively. The pump beam was amplified to 10s of mJ at a multipass Ti:sapphire amplifier and then compressed to subpicosecond in the compressor. 1% of the pump pulse was separated and its spectral phase and pulse length was characterized by a commercial device based on the spectral phase interferometry for direct electric-field reconstruction (SPIDER, APE LX Spider [75]). The pump and the probe were focused on the center of the target chamber that filled with low pressure helium gas. The spectrometer consists of a Czerny-Turner spectrograph (ISA HR320) coupled with a time-gated intensified CCD (Princeton Instrument PI-MAX4). The gate width and the gate delay of the intensified CCD were set to optimize the Thomson scattered signal and minimize the stray light from plasma recombination emission and from other objects inside the chamber (will be discussed in depth later).

The control of polarization was achieved by inserting waveplates (half-wave plate for linear polarization and quarter-wave plate for circular polarization) between the KDP crystal and the OAP. This arrangement increases the delay between the pump and probe (due to the group delay in WP) but is necessary because in the opposite arrangement a circular polarized pulse will be temporally separated by the KDP crystal into two pulses that are linearly polarized along the fast and slow axes. The half-wave plate which is designed for 800 nm light has no effect on the polarization of the 400 nm probe beam, but the quarter waveplate will rotate the probe beam polarization by 90° (parallel to the scattering plane). While the polarization of the probe pulse has no influence on the spectral shapes, it affects the scattered power collected in the experiment, and the signal strength for circular polarization is reduced by a factor of 2. It should be noted that for the CP case the rotation angle of the quarter-wave plate has to be fine-tuned to make an ideally circularly polarized pump beam at the focus since the reflection from the OAP changes the polarization.

3.2.1 Alignment of the light collection system for the scattered light

A precise optical alignment is required for Thomson scattering experiment. The scattering volume, which is approximately the intersection of the plasma column and the cylinder defined by the collection optics, has a dimension of the order of 10^{-7} cm^3. To project the correct regime of the plasma into the entrance slit of the spectrometer, the horizontal precision of the alignment has to be better than the slit size $\sim$ 200 μm. Because of the shape the slit, the vertical precision is not as important as the horizontal one, but making the image of the plasma near the center of the slit is still desired.

To ensure a sufficient precision, the following alignment procedure is applied for this experiment:

1. A two-dimensional motorized stage mounted with a vertical metal wire (width 200 μm) is set in the center of the target chamber. The wire is placed at the focus of the OAP for 800 nm light in vacuum.

2. An auxiliary He-Ne laser beam is set as shown in the left and center of Fig. 3.4 to backlight the wire. The beam is guided through the center of the entrance slit of the spectrometer and monitored by an auxiliary CCD.

3. The one-to-one imaging system comprised of two achromatic lenses is aligned by using the He-Ne beam and the CCD. The images of the wire that are relayed to the entrance slit are shown in the top-right (by the auxiliary CCD) and the bottom-right (by the spectrometer at zero-order diffraction) of Fig. 3.4.

4. The spectral response of the imaging system and the spectrometer is measured by putting a calibration light source (Ocean Optics HL-2000) at the center of the target chamber.

A translation stage for the second lens is necessary to compensate the focal length differences between the He-Ne laser (633 nm) and the probe beam (400 nm) and between in vacuum and in air.

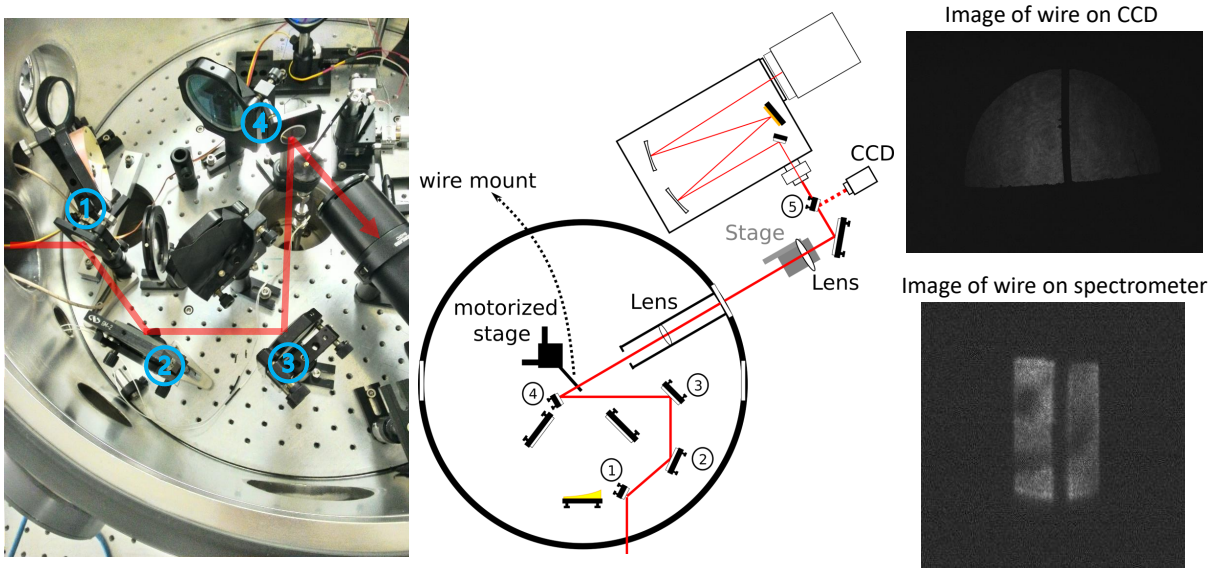

Figure 3.4: **The alignment of the spectrometer:** Five auxiliary mirrors, a motorized stage, and a CCD are set as shown. A small wire target is mounted on the motorized state and is used to indicate the focus position of the OAP. On the top-right side is the image of the wire on the CCD. On the bottom-right side is the image of the wire and the entrance slit on the intensified CCD of the spectrograph (the grating is at zero-order diffraction).

3.2.2 Stray light control

Another critical factor for Thomson scattering measurement is the signal-to-noise ratio. Since the small size of the scattering volume, the collected number of photons per unit frequency could be quite small, especially when the experiment is running in the noncollective regime. In some cases, signal-to-noise ratio can be significantly reduced when even a few stary light photons with a similar frequency of the probe are received by the detector.

Three main sources of stray light and the ways to control them are discussed in the following:

- Self-generated second-harmonic light

  It has been found that second harmonic generation occurs when an intense laser pulse interacts with an underdense plasma. Coherent 2ω light generated from laser-plasma interaction overlaps temporally with the pump pulse. Scattered 2ω photons from this source are regarded as stray light since the scattering happens at a time frame while the plasma is strongly affected by the laser field. Thomson scattering spectra from the self-generated 2ω light were measured independently without the KDP crystal for different setups and had been subtracted from the results with the probe beam. The properties of the self-generated 2ω light will be explored further in Chapter 5.

- Plasma emission

  The presence of continuous/line plasma emission reduces the signal-to-noise ratio for TS experiments. There are several prominent emission lines near 400 nm (especially the line at 388 nm) for helium plasmas. The emission is less intense than the scattered light but lasts much longer (10s of ns). The gated intensified CCD can effectively reduce the noise level from plasma emission by minimizing the gate width. The intensified CCD (PI-MAX4) has minimum gate width of 2.8 ns, but effective gate width can be further shortened by pre-opening the gate. Due to the jitter of the trigger signal, the effective gate width in the measurement is optimized to be ~ 5 ps.

- Parasite radiations

  Some radiations from the probe beam can reach the detector by routes other than scattering from the plasma. For example, a small portion of the probe beam can reflect from the beam dump or other objects inside the chamber and end up collected by the spectrometer. Scattered photons from other physical origins, such as Rayleigh scattering when many neutral particles are present, can also contribute to the unwanted radiation. In the present experiment, the parasite radiation is controlled by the gated intensified CCD of the spectrograph, black covers and a view dump. A gated camera can reduce the noise level by cutting the shutter before the photons reflected from distant objects reach the camera. It takes 10s of ns for photons to travel from the wall of chamber back to the plasma. A black tube and an iris that cover the lens inside the chamber (as shown in Fig. 3.3) can also reduce the chances that the parasite radiations are collected.

  One of the most important components to reduce the parasite radiation is the view dump, which is directly seen by the scattering light collection optics. Due to the limited space in the target chamber, a flat black material is used as the view dump instead of a deep cavity. Various materials, including black anodized aluminum (Al) plates, black Al foils, razor blade beam blocks, and commercial black coatings, were considered as the candidate of the view dump and tested using a low-power 800 nm laser without plasmas. The test results of the two most effective materials are shown in Fig. 3.5(a). Vantablack is a commercial black coating made of vertically aligned carbon nanotubes. Due to its effectiveness, a sample (4×4 cm^2) of Vantablack was used as shown in Fig. 3.3 and 3.5(b).

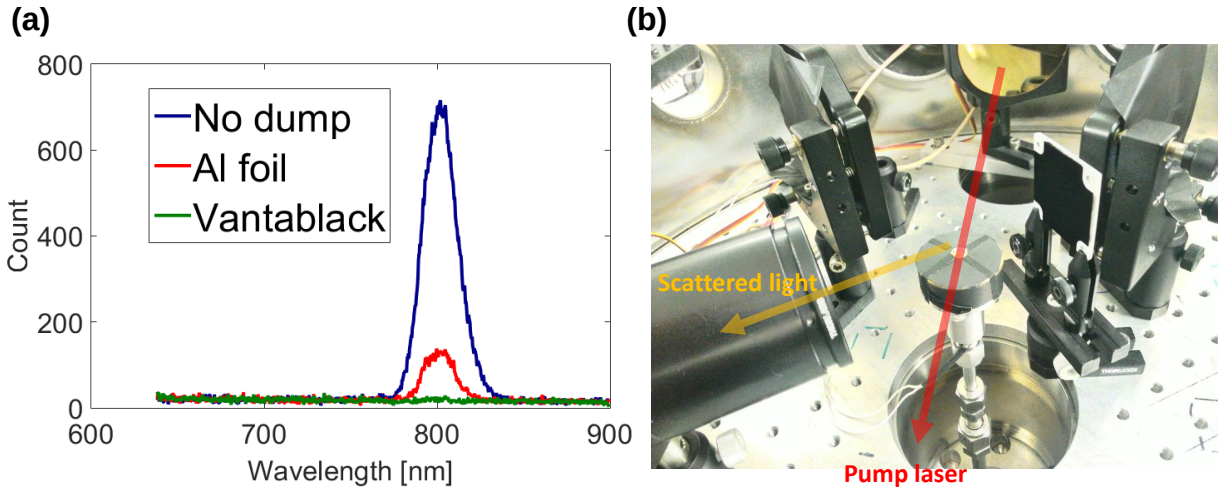

Figure 3.5: **The setup and test of the view dump**: (a) The measured background signal of the spectrometer from the 800-nm pump laser when no view dump or view dumps made of two materials are used. (b) A sample of Vantablack is used as the view dump.

3.3 Initial EVDF of OFI He plasmas

3.3.1 Raw spectra

A raw image from the imaging spectrometer is shown in Fig. 3.6(a) for the case of 100 torr He and the polarization of $L_\perp$. The horizontal axis show the spatially separated spectrum and the vertical axis represents the space spanned by the slit length. The central part of spectrum in Fig. 3.6(a) is deliberately set to be saturated to highlight the side-band feature. The scattered light from the regime of the plasma can be spatially separated from the scattering from other object such as the gas jet. The spectrum of the Thomson scattering from the plasma appears in a band (dashed blue box) with a frequency-dependent thickness. It is considered the consequence of the chromatic aberration of the imaging spectrometer but has not impact on the spectral density. The calibrated spectrum is shown in Fig. 3.6(b) by integrating all counts in the band and adjusting the magnitude based on the spectral response of the system. The signal strength from the ion feature is dominant over the one from the electron feature. However, it is the electron feature that gives the information of

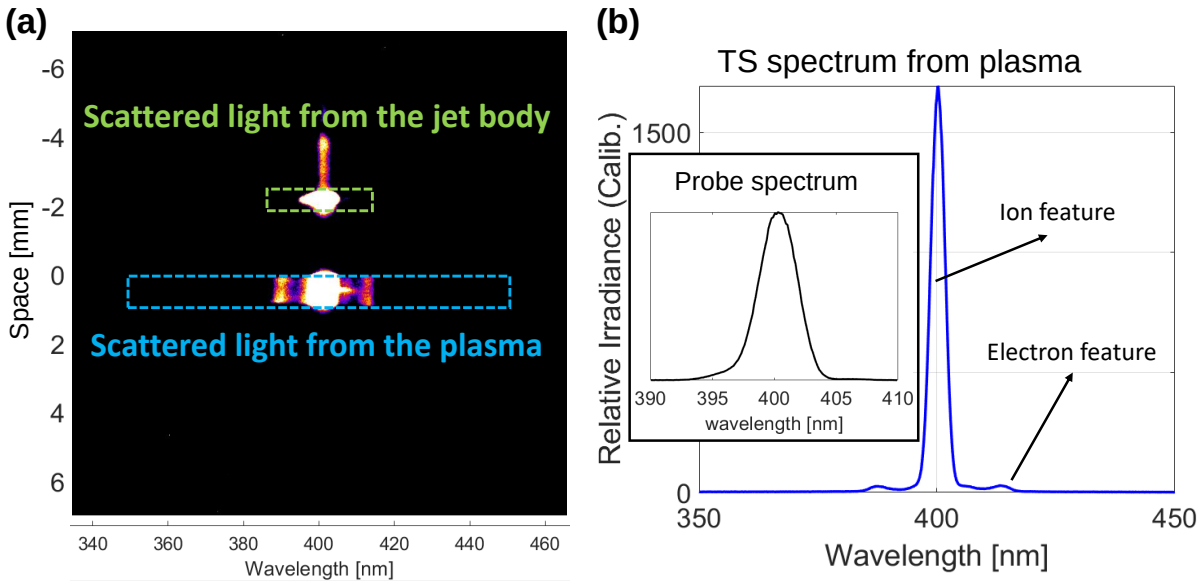

Figure 3.6: **Raw image and calibrated spectra:** (a) Raw image spectrum for a helium gas pressure of 100 torr and the polarization configuration $L_{\perp}$. (b) Calibrated spectrum of scattered light from plasma

the plasma electrons. The spectrum of the probe is shown in the inset of Fig. 3.6(b). This spectrum is obtained by using the probe beam light scattered from the gas jet, even though the gas jet is not actually used in this experiment. The measured bandwidth (3.7 nm) of the probe is the result of the convolution of the bandwidth of the probe beam ($\sim$ 3.4 nm) and the instrument function of the spectrometer.

3.3.2 Spectral fittings

The measured scattered spectra are used to infer the near instantaneous status of OFI plasmas by comparing them with the Thomson scattering theory [72]. All the data shown are the average of 200 consecutive shots to improve the signal-to-noise ratio. Due to the broad bandwidth of the probe beam and the limiting wavelength resolution ($\sim$ 1 nm) of the spectrograph, the ion feature spectrum is not resolved in our experiment and thus information about the plasma comes from the electron feature. For given plasma parameters (density and temperature) or distribution functions (f_e and f_i), the SPD function (Eq. (3.3)) is

convolved with the probe spectrum to generate a spectrum used in fitting. The convolved SDF functions (denoted as $S_{\mathrm{T}}(\omega)$) are calculated as

$$S_{\mathrm{T}}(\omega) = \sum_i \mathrm{W}(\omega_i)\, S(\mathbf{k}_{\mathrm{m}}, \omega_i) \tag{3.11}$$

where

$$S(\mathbf{k}_{\mathrm{m}}, \omega_i) = \frac{2\pi}{k_{\mathrm{m}}} \left|1 - \frac{\chi_e}{\epsilon}\right|^2 f_e\left(\frac{\omega_i}{k_{\mathrm{m}}}\right) + \frac{2\pi Z}{k_{\mathrm{m}}} \left|\frac{\chi_e}{\epsilon}\right|^2 f_i\left(\frac{\omega_i}{k_{\mathrm{m}}}\right)$$

where $k_{\mathrm{m}} = |\mathbf{k}_{\mathrm{m}}|$ is the measured wave number and $\mathrm{W}(\omega_i)$ is the weight factor function for the frequency component ω_i as shown in Fig. 3.7(a). In Eq. (3.11), the fit parameters should be applied to χ_e, χ_i, f_e, and f_i. The lowest $\Delta\omega$ achieved is about 0.1 nm which is the spectral difference between two adjoining pixels of the spectrometer.

A Maxwellian EVDF is assumed for the case in Fig. 3.6(b). Since the plasma density is known (6.6×10^{18} cm^{-3}) due to the full ionization of 100 torr helium, there is only one parameter (temperature) should be fitted. The fitting is done with a plasma temperature of 18 eV as demonstrated in Fig. 3.7(b).

3.3.3 EVDF of helium plasmas for different polarization configurations

The scattered light spectra from plasmas produced by LP pump taken at two fill pressures are shown in Fig. 3.8. The frequency shift of the electron feature, which is associated with collective scattering from electron plasma waves is symmetric on either side of the ion feature. The red dashed line in each plot is the best fit of the calculated SDF function $S_{\mathrm{T}}(\omega)$. Figure 3.8(a) and 3.8(b) show the spectra where the polarization is perpendicular to the scattering plane ($L_\perp$). We found that a single Maxwellian distribution with electron temperature of 18 ± 2 eV (room temperature ions) fits spectra obtained at both low (10 torr) and high (75 torr) pressures. The corresponding temperature in the perpendicular plane after 300 fs is expected to be ~ 12 eV from simulations. Thus there is a reasonable agreement between the experiment and the simulations.

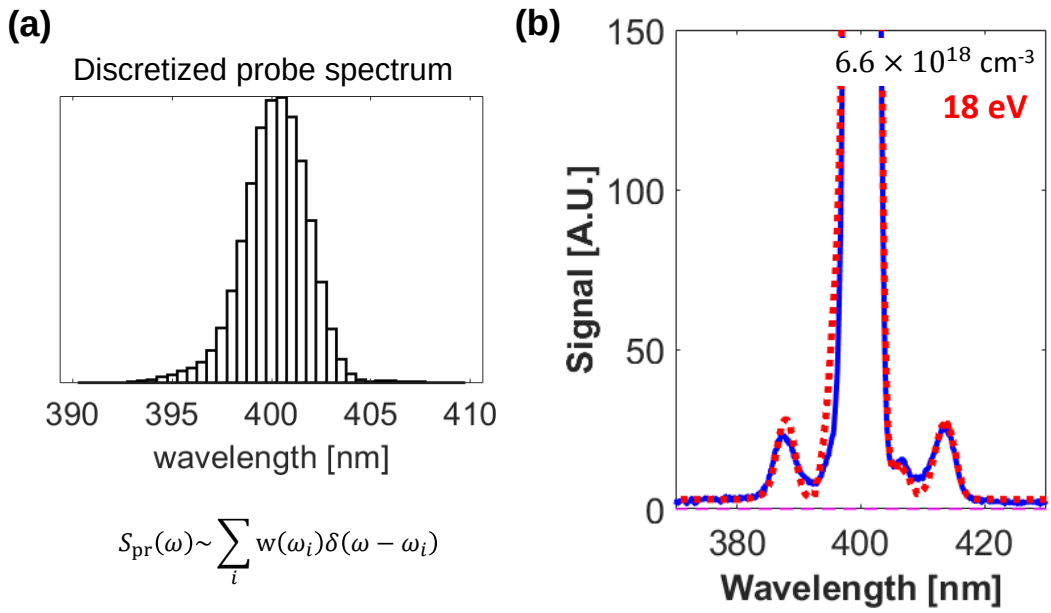

Figure 3.7: **Demonstration of fitting by the discretization of the probe spectrum:** (a) The measured probe spectrum is discretized. $w(\omega_i)$ represents the weight of the discretized frequency component ω_i. S_{pr} is the SPD function of the probe. (b) The measured spectrum (blue curve) and best fit (dotted red curve) for the case of 100 torr He and $L_\perp$ polarization. The fit is the sum of the SDF of frequency components ω_i for a Maxwellian distribution with an electron temperature of 18 eV and a density of 6.6×10^{18} cm^{-3}.

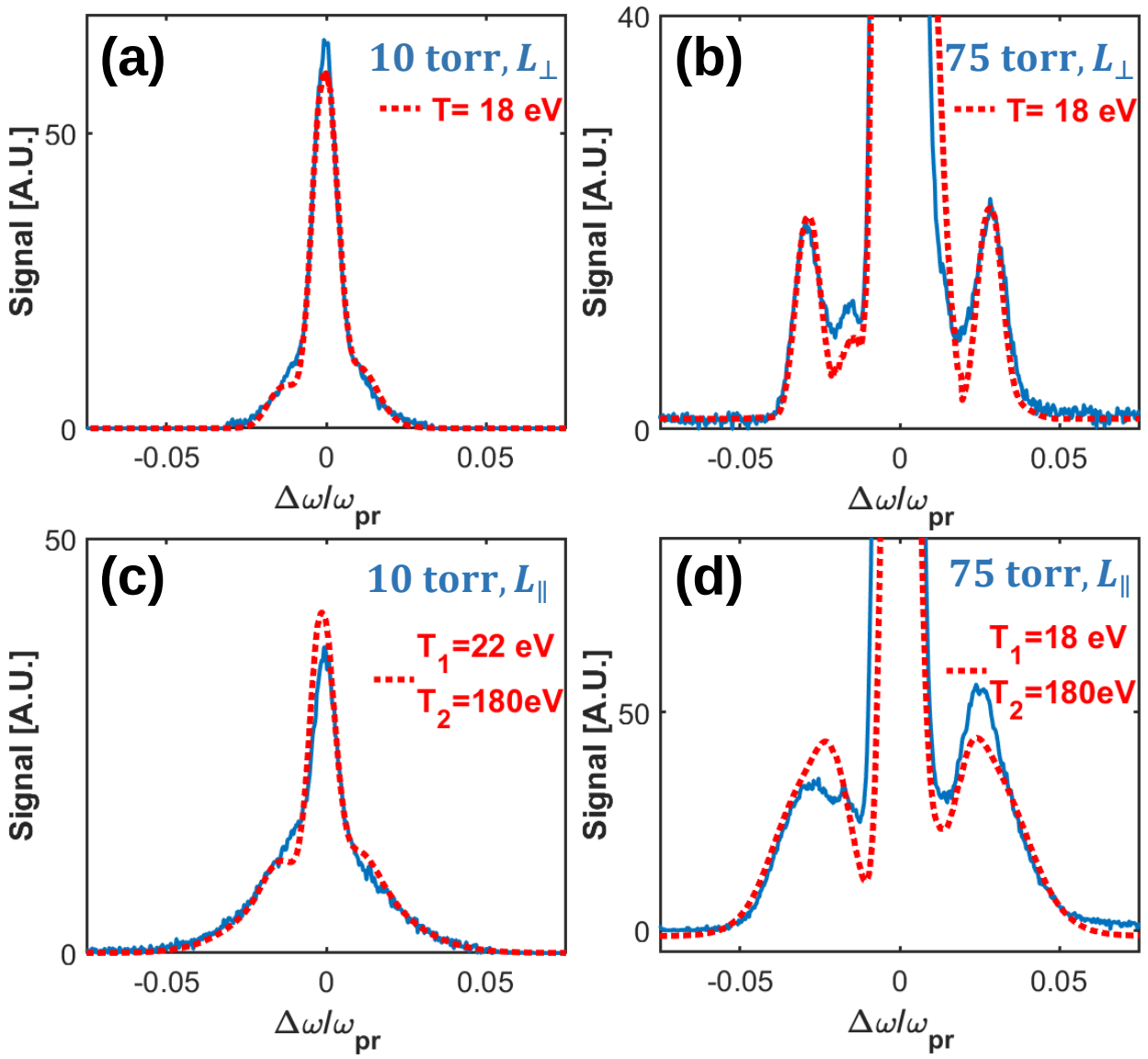

Figure 3.8: **Thomson scattering spectra for linear polarization.** (blue curves - experimental spectra; dotted red curves - calculated spectra). Polarization direction is out of the scattering plane for (a) and (b) and parallel to the scattering plane for (c) and (d). The $L_\perp$ cases can be fit by a single temperature (T) of 18 eV whereas the $L_\parallel$ cases require a two-temperature fit (T_1 and T_2) as shown.

The scattering spectra when the linear polarization is in the scattering plane $L_{\parallel}$ are shown in Fig. 3.8(c) and 3.8(d) also for helium fill pressures of 10 and 75 torr respectively. In this case, the calculated SPD functions given by a single Maxwellian distribution (not shown) do not fit with the experimental spectra. The data were therefore fitted by taking a two-temperature distribution into consideration. Substituting $f_e = 0.5 f_{e,T_1} + 0.5 f_{e,T_2}$ into Eq. (\ref{eq1}) where T_1 and T_2 are fitting parameters ($T_2 > T_1$) while keeping the ions as a fixed ultra-cold component, we get a new set of SPD functions that describe the scattering spectra for the linear polarization case. The best fits give $T_1 = 20 \pm 2$ eV and $T_2 = 180 \pm 20$ eV. As we discussed in Section 3.1.2, the temperatures of the two-Maxwellian distributions in the experiments are expected to be different than those from the simulations since we observe the plasma along $\mathbf{k}_{\mathrm{m}}$ which has a 30° angle with respect to the transverse plane used in simulations. The observable temperatures, which are evaluated from the projection of the distribution onto the measured wavevector [74], are about 45 and 160 eV for polarization $L_{\parallel}$. The agreement here with the simulations is again reasonable. We can see that the theoretical plots shown Fig. 3.8(c) and 3.8(d) fit less well than those for Fig 3.8(a) and 3.8(b) both taken at the same pressure but in the orthogonal plane.

The frequency shift of the electron feature in the collective scattering regime should increase as the Bohm-Gross frequency ω_{BG} (Eq. (3.8)). Figure 3.9 shows the measured spectral peak shifts for various plasma densities for different polarization configurations. For both $L_{\perp}$ and $L_{\parallel}$, the shifts of their sideband peaks both increase with densities as expected. This is clearly not the case in the case of circular polarization which is also shown. The frequency shift of the electron feature for the CP case was almost independent of the plasma density, which is indicative of some other collective phenomena being dominant collective scattering mechanism than the usual Bohm-Gross waves.

The Thomson scattered spectra for the CP pump pulses are shown in Fig. 3.10. Recall that the electrons in this case have higher average kinetic energy than those with LP and the EVDF deviate greatly from Maxwellian. Our fitting attempt using $S_{\mathrm{T}}(\omega)$ failed with either one-temperature or two-temperature Maxwellian distributions as expected. At low enough

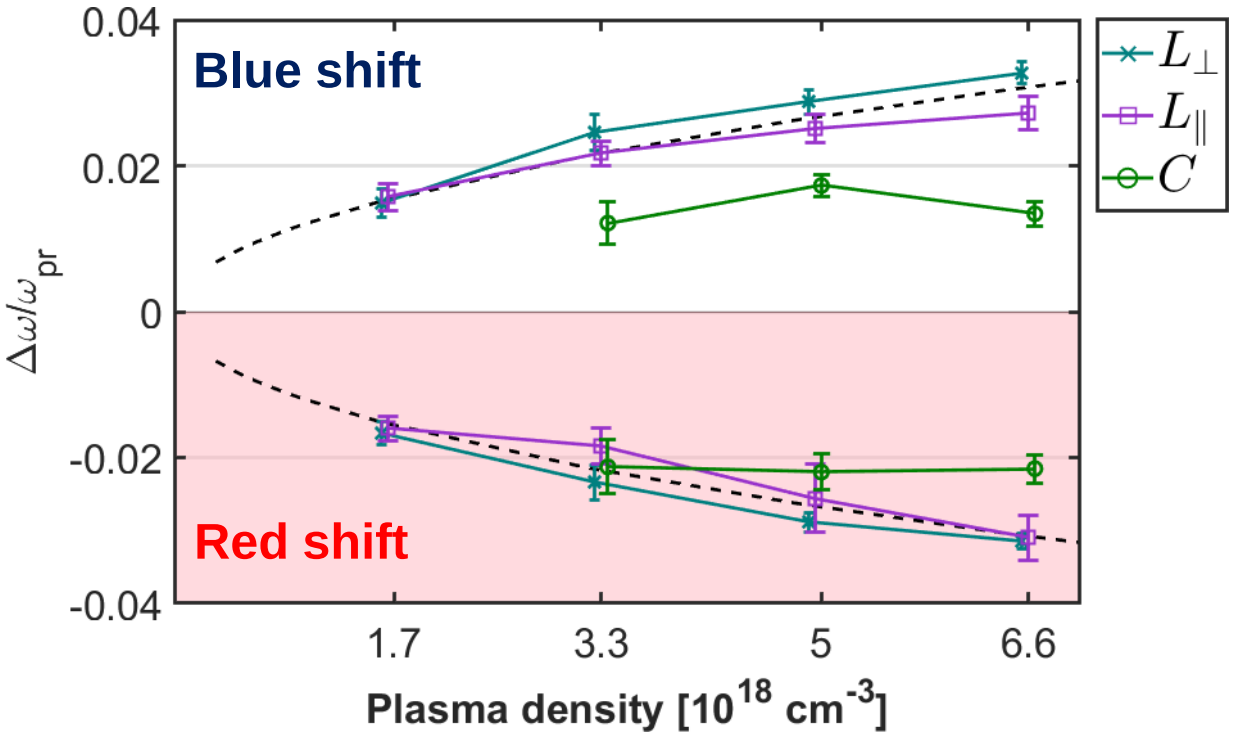

Figure 3.9: The measured spectral peak shifts of the electron feature for different plasma densities and different laser polarization ($L_\perp$, $L_\parallel$, C). The error bars show the standard deviation of the shifts for 100 shots. The dashed lines show the variation of frequency shift equal to the plasma frequency, $\Delta\omega = \omega_{\mathrm{pe}}(n_e)$.

plasma densities collective effects are not important and one expects photons to be Doppler up or down shifted because of the individual electron motion irrespective of the shape of the EVDF. We found that it is possible to fit the experimental spectrum taken at this low plasma density using the distribution function observed in the simulation as shown in Fig. 2.7(c). The simulated EVDF fits to the wings of the total spectrum with a plasma density of 6.6×10^{17} cm^{-3} used in the experiment. When the spectrum of the stray probe photons is also taken into account the overall Doppler shifted plus the stray photon spectrum fits the experimentally measured spectrum extremely well. This excellent fit confirms that the EVDF in the CP case has four streams in the radial direction as shown by the lineout in Fig. 2.7(c).

For the higher density case (Fig. 3.10(b)) two distinct spectral "electron" peaks with asymmetric shifts appeared. Their frequency shifts were both $\leq \omega_{\mathrm{BG}}$ and independent of the plasma density as was not the case with LP shown in Fig. 3.9. This is expected if the scattering is from the streaming instability where the spectral shift depends on the streams' drift velocity, $\Delta\omega \sim \mathbf{k}_{\mathrm{m}} \cdot \mathbf{v}_{\mathrm{d}}$ where $\mathbf{v}_{\mathrm{d}}$ is the relative drift velocity between electron streams which is independent of plasma density. Substituting the observed spectral shift of two satellites we obtain $|\mathbf{v}_{\mathrm{d}}|$ equal to $(0.02 \pm 0.002)\,c$ (blue) and $(0.025 \pm 0.005)\,c$ (red) respectively. Since $\mathbf{k}_{\mathrm{m}} = \mathbf{k}_r + \mathbf{k}_z$ we are actually observing the oblique electron streaming instability. This is confirmed in the OSIRIS simulations. The streaming instability onset occurs in the x-y plane as expected but it quickly spreads in all three dimensions this in turn leads to the onset of the electron streaming instability in an oblique direction [76] that was observed. The unstable modes developed in OFI plasma will be discussed further in the next chapter. The reason why one can measure the density dependence of the plasma frequency using Thomson scattering in the LP case is that the onset of the two-stream instability happens almost 1 ps later when LP is used compared to when CP laser pulse is used. This is because the ionization process itself produces relative electron streaming in the CP case whereas the fastest He^{2+} electrons have to bounce off the plasma sheath to begin streaming in LP case [77].

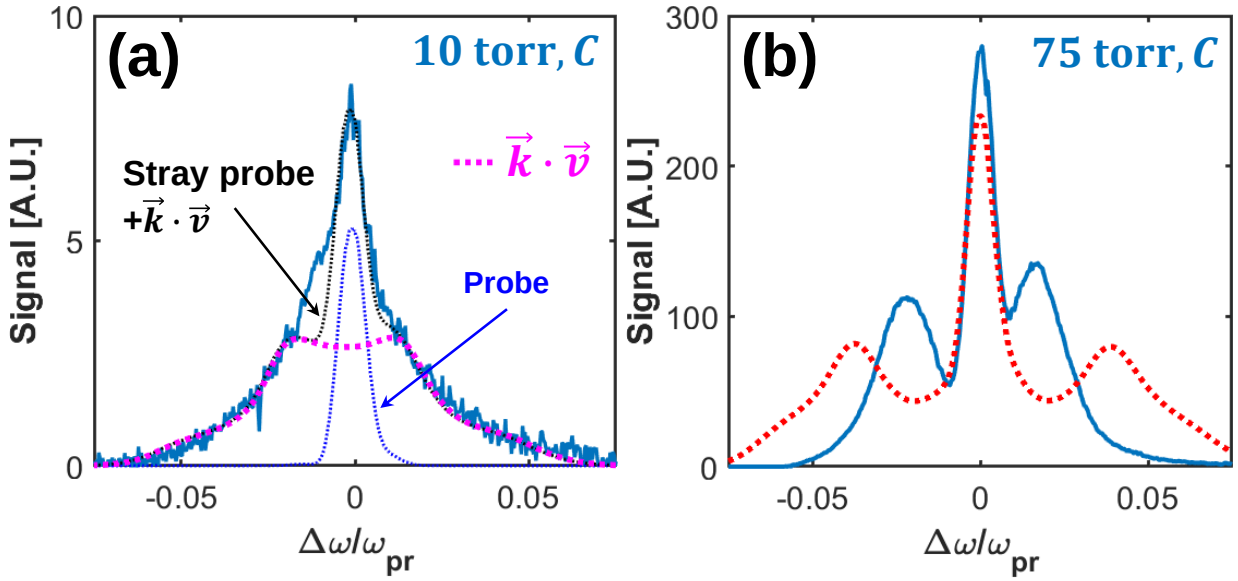

Figure 3.10: **Thomson scattering spectra for circular polarization averaged over 200 shots:** (a) the measured spectrum at 10 Torr He pressure and a fit that is the sum of the Doppler shifted spectrum (dotted pink curve) expected from the electron distribution shown in Fig. 2.7(c) and stray light spectrum of the probe beam (dotted blue curve). (b) The measured Thomson scattered spectrum at 75 Torr (blue curve) and the calculated spectrum (dotted red curve) using a distribution with two pairs of drifting Maxwellian counter streams (drift velocities of $\pm 0.015c$ and $\pm 0.046c$, widths of 87 and 79 eV, and a density ratio of $\sim 4:1$) deduced from the EVDF shown in Fig. 2.7(c).

3.4 Summary

In conclusion, OFI is demonstrated to be a possible method for controlling the initial EVDF in plasmas. Thomson scattering diagnostic is used to probe two such EVDF within 300 fs of their initialization by OFI in He plasmas using different polarization configurations. The scattered light spectra are consistent with the expected anisotropic distributions. The summary of the fitting is shown in Table 3.1. Until they are isotropized and thermalized such plasmas cannot be described by the fluid theory and thus present a new platform for studying kinetic effects and instabilities in laboratory plasmas.

Pol.	He^{1+}	He^{2+}	Fit distribution	Best-fit parameters
$L \perp$	8 eV	16 eV	Maxwellian	18 ± 2 eV
$L_{\parallel}$	54 eV	190 eV	Two-Maxwellian	20 ± 2 eV; 180 ± 20 eV
C	200 eV	780 eV	Non-Maxwellian	Extracted from sim.

Table 3.1: Fitting parameters of initial EVDF from different polarization configurations.

CHAPTER 4

Measurements of Kinetic Plasma Instabilities in OFI plasmas

In Chapter 2 and 3, anisotropic electron velocity distributions are shown to be initialized by optical field ionization of atoms using ultrashort laser pulses. Since such a plasma is not in a state of thermodynamic equilibrium, plasma dynamics should lead to increase the system entropy and the plasma may become unstable. The results of the collinear TS experiment using a CP laser pulse and a helium gas suggest that instabilities can grow very fast in certain conditions. Physically, kinetic instabilities arisen in plasma to bring the system closer the equilibrium state. For example, when there are beams (groups of charge particles) drifting relative to the rest of the plasma, an electrostatic instability commonly known as the streaming instability can be excited. The drifting beams transfer its kinetic energy to waves through the inverse Landau damping- a kinetic or collisionless process. For another example, when there is a temperature anisotropy in a plasma, electromagnetic instabilities may arise that induce a magnetic field in the plasma. The induced fields tend to decrease the anisotropy of the system. As the plasma is driven further away from the equilibrium, one can expect kinetic instabilities may grow faster or stronger in the plasma.

The unstable modes from polarization-dependent anisotropic EVDF are first studied by theory and PIC simulations. The fluid theory is useful to determine the regions of the parameters that drive the plasma unstable, but a kinetic theory is usually needed to acquire the correct growth rate of an instability. By taking the electron distribution functions from simulations, we model the initial growth rate of unstable modes from a kinetic theory. However, the actual OFI plasma system is very complicated and an exact kinetic theory is yet

to be fully developed. Even though the growth of instabilities is correctly predicted, the saturation and damping of unstable waves are not attainable in the current simple model. Therefore, the nonlinear behaviors of various kinetic instabilities are instead obtained by computer simulations. It is found that following the ionization but before collisions thermalize the electrons, the plasma undergoes streaming, filamentation, and Weibel instabilities that isotropize the electron distributions. These instabilities trigger density modulations in extremely short time scales (100s fs - 10s ps). To experimentally study these effects, a time-resolved short-pulse TS is used based on the technique introduced in Chapter 3. Transient enhanced collective TS signal from the density modulations induced by these unstable modes are measured. The polarization-dependent frequency and growth rates of these kinetic instabilities agree well with the theory and simulations.

4.1 Kinetic instabilities grown in an OFI plasma

Three type of kinetic instabilities thought to grow in an OFI plasma are studied here. It is known that when plasma electrons comprise of two or more co- or counter- propagating streams (beams), they can be unstable to both the streaming and filamentation instabilities [78, 79]. The streaming instability is electrostatic ($\mathbf{k} \times \mathbf{E} = 0$) which generates longitudinal waves- charge density modulations- on the beams via inverse Landau damping at the expense of the directional energy of the streaming electrons [80]. If the streams are symmetric, the two-stream instability is aperiodic which means it grows without oscillation, otherwise the instability has a nonzero oscillation frequency [1]. The filamentation instability grows simultaneously with the streaming instability. It begins with azimuthal magnetic fields surrounding noise current streams in the plasma. Attraction (repulsion) between co- (counter-) propagating currents causes the currents to coalesce and thereby amplify the magnetic fields that surround the filaments [16]. In the non-relativistic regime, the filamentation instability is electromagnetic ($\mathbf{k} \cdot \mathbf{E} = 0$) when the counter-propagating currents are symmetric so that they can pinch at the same rate [81]. The anisotropic EVDF of the plasma electrons also causes the Weibel instability to grow via a similar mechanism as the filamentation instabil-

ity [16, 15, 79], but the growth rates and the spectral evolution of the unstable modes are different.

4.1.1 Onset of the kinetic instabilities in simulations

Limited by available computational resources, 2D PIC simulations with higher resolutions were performed to model the evolution of the instabilities. The configurations of the simulations are similar the one shown in Fig. 2.6. In the simulations, the anisotropic EVDF are initialized by ionizing helium using either linearly polarized (LP) or circularly polarized (CP) 800-nm laser pulses. The bi-Gaussian pump laser pulse has a duration of 50 fs (FWHM) and a spot size of $w_0 = 8$ μm, and the peak intensity of the laser pulse is 1×10^{17} W/cm^2, sufficient to ionize the first He electrons early during the rising intensity of the laser pulse and the second He electrons approximately 10 fs later.

Snapshots of the phase space distribution of the He^{1+} and He^{2+} electrons for both the CP and LP case are shown in Fig. 4.1. In the CP case (Fig. 4.1(a)), the streaming motion of electrons is initiated directly by the ionization process. As shown in Chapter 2, there are radial streams at any position inside the bulk, so we can find four streams in any transverse direction. The streaming is not only between the counter-propagating He^{2+} electrons but also between the co- and counter-propagating He^{2+} and He^{1+} electrons. In the LP case (Fig. 4.1(b)), He^{1+} and He^{2+} electrons both have Maxwellian distributions but He^{2+} electrons are much hotter along the laser polarization. Hotter He^{2+} electrons initially distributed inside the double sheath (within ± 10 μm) later spread to the small region between two sheathes (between ± 10 and ± 12.5 μm) and eventually be reflected by the sheath fields. This causes a phase separation of He^{2+} electrons and counter-propagating streams appear as indicated by the pink arrows in Fig. 4.1(b). The streaming then occurs between the highest energy He^{2+} electrons that bounce off the sheath fields and the remaining quasi-stationary electrons.

An indication of the growing unstable waves can already be seen from the phase space shown in Fig. 4.1(a), where the red arrows show some He^{1+} electrons are trapped and accelerated by the transverse waves. At the same time, some He^{2+} electrons are deaccelerated

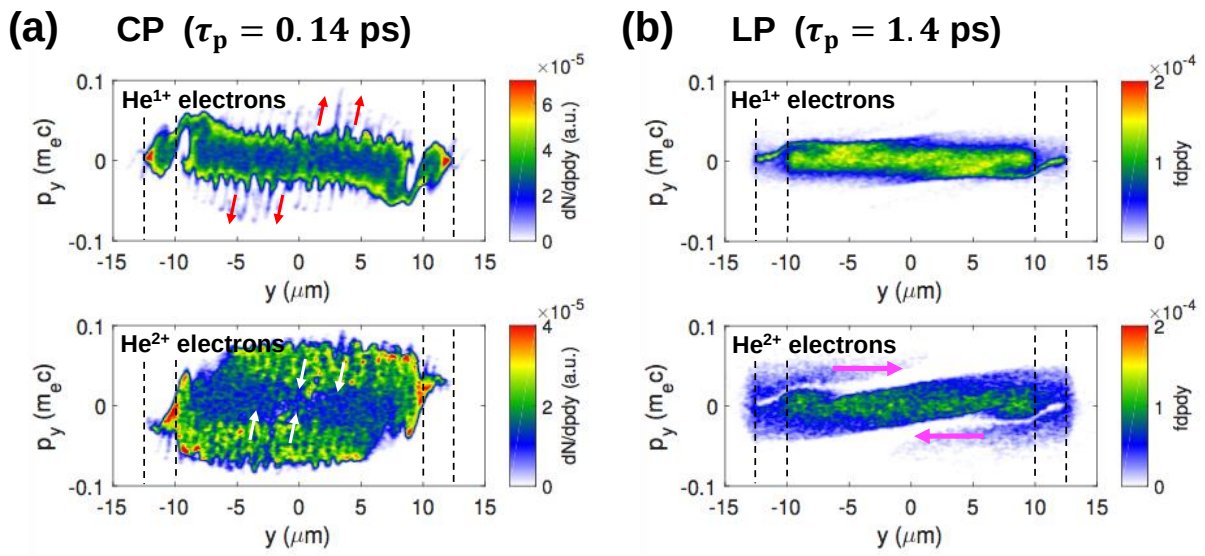

Figure 4.1: **Transverse phase space of He^{1+} and He^{2+} electrons inside a Δz = 2 μm slab at a later moment (τ_p) after being initialized.** Electrons ionized by (a) a circularly polarized (CP) pulse 0.14 ps after the laser leave the slab and (b) linearly polarized (LP) pulse 1.4 ps after laser leave the slab. The color bars represent the density of the electrons [in arbitrary units (a.u.)]. The black dashed lines mark the locations of the thin sheaths. The direction of the red (white) arrows indicates the acceleration (deceleration) of the trapped particles. The direction of the magenta arrows indicates the shift of the momentum distributions.

as indicated by the white arrows. The He^{1+} electrons are heated in this process at the expense of He^{2+} electrons. In the CP case, the streaming instability grows simultaneously everywhere in the plasma. Because the electrons produced by an LP laser are cooler than those produced by a CP laser and in any case the streams are not established until the He^{2+} electrons bounce off the sheath, we expect the streaming instability to grow at a later time in the LP case compared with the CP case.

4.1.2 Streaming instability

As the simulations of the phase space (Fig. 4.1) demonstrate, electron streams appear in OFI plasma as the results of initial EVDF and the boundary sheaths for both CP and LP cases. Those streams can trigger streaming instabilities at the location where the streams overlap. In this section, the growth of the electrostatic instability is analyzed by the non-relativistic fluid theory. Since both drifted Maxwellian electron groups in the CP case and the reflected He^{2+} electron groups have drift velocities much larger than the thermal velocity (the width of the beam), we may model each electron group as a cold electron beam. Consider there are several beams/species (ions included), the continuity equations and the fluid equation of motion for jth beams are

$$\frac{\partial n_j}{\partial t} + \nabla \cdot \left(n_j \mathbf{v}_j\right) = 0 \tag{4.1}$$

$$\frac{\partial \mathbf{v}_j}{\partial t} + \left(\mathbf{v}_j \cdot \nabla\right) \mathbf{v}_j = \frac{q_j}{m_j}\mathbf{E} \tag{4.2}$$

where n_j, $\mathbf{v}_j$, q_j and m_j are the density, velocity charge and mass of the jth beam. The ions that form the uniform background are considered as a stationary cold beam. The particles in the different beams are coupled through the Poisson's equation

$$\nabla \cdot \mathbf{E} = 4\pi \sum_j q_j n_j \tag{4.3}$$

Substitute the quantities $n_j = n_{0j} + n_{1j}$, $\mathbf{v}_j = \mathbf{v}_{0j} + \mathbf{v}_{1j}$, and $\mathbf{E} = \mathbf{E}_0 + \mathbf{E}_1$ into fluid equations, where n_{0j}, $\mathbf{v}_{0j}$ are the unperturbed quantities (assuming $\mathbf{E}_0 = 0$) and n_{1j}, $\mathbf{v}_{1j}$, and $\mathbf{E}_1$ are the first-order perturbation quantities that vary as $\exp\left[i\left(\mathbf{k}\cdot\mathbf{r} - \omega t\right)\right]$, linearized Eq. (4.1) and (4.2) can be solved for the first-order quantities

$$n_{1j} = \frac{i q_j n_{0j} \mathbf{k}\cdot\mathbf{E}_1}{m_j\left(\omega - \mathbf{k}\cdot\mathbf{v}_{0j}\right)^2} \tag{4.4}$$

$$\mathbf{v}_{1j} = \frac{i q_j \mathbf{E}_1}{m_j\left(\omega - \mathbf{k}\cdot\mathbf{v}_{0j}\right)} \tag{4.5}$$

Assuming charge neutrality in the zero-order equilibrium, the dispersion relation for longitudinal oscillations can be obtained by substituting Eq. (4.4) and (4.5) into the linearized Eq. (4.3),

$$1 = 4\pi \sum_j \frac{n_{0j} q_j^2}{m_j\left(\omega - \mathbf{k}\cdot\mathbf{v}_{0j}\right)^2} \tag{4.6}$$

For the simplest case, two electron streams of equal density are present with uniform ion background. The contribution of ion can be ignored by assuming $m_i/m_e \to \infty$ where m_i is the mass of the ion. Assuming the first and second beams have average velocities of $\mathbf{v}_{01}$ and $\mathbf{v}_{02}$, the dispersion relation can be written as

$$1 = \frac{\omega_\mathrm{p}^2}{2} \frac{\left(\omega - \mathbf{k}\cdot\mathbf{v}_{01}\right)^2 + \left(\omega - \mathbf{k}\cdot\mathbf{v}_{02}\right)^2}{\left(\omega - \mathbf{k}\cdot\mathbf{v}_{01}\right)^2\left(\omega - \mathbf{k}\cdot\mathbf{v}_{02}\right)^2} \tag{4.7}$$

where $\omega_\mathrm{p}^2 = 4\pi e^2 n_0/m_e$ and $n_0 = n_{01} + n_{02}$. Eq. (4.7) has solutions of

$$\left(\omega - \mathbf{k}\cdot\overline{\mathbf{V}}\right)^2 = \frac{\omega_\mathrm{p}^2}{2}\left[1 + 2X^2 \pm \left(1 + 8X^2\right)^{1/2}\right] \tag{4.8}$$

where

$$\overline{\mathbf{V}} = \frac{1}{2}\left(\mathbf{v}_{01} + \mathbf{v}_{02}\right)$$

$$X = \frac{\mathbf{k} \cdot (\mathbf{v}_{01} - \mathbf{v}_{02})}{2\omega_{\mathrm{p}}}$$

Two of the four roots of Eq. (4.8) are always real and they represent stable modes. The other two roots contain imaginary parts if $X^2 < 1$. The growth of the first-order quantities occurs when the imaginary part of ω is postive, so the growth rate for the two-stream case is

$$\gamma = \mathrm{Im}\,[\omega] = \frac{\omega_{\mathrm{p}}}{\sqrt{2}} \sqrt{\sqrt{1 + 8X^2} - 1 - 2X^2} \tag{4.9}$$

which has a maximum of

$$\gamma_{\mathrm{max,two\text{-}stream}} = \frac{\omega_{\mathrm{p}}}{2\sqrt{2}} = 0.35\omega_{\mathrm{p}} \tag{4.10}$$

at $X = \sqrt{3/8}$. Consider the one-dimensional case, the two beams have drift velocities v_{01} and v_{02} ($|v_{01}| \geq |v_{02}|$), the most unstable k and its frequency $\omega_{\mathrm{R}} = \mathrm{Re}[\omega]$ will be

$$k = \sqrt{\frac{3}{2}} \frac{\omega_{\mathrm{p}}}{v_{01} - v_{02}} \tag{4.11}$$

$$\omega_{\mathrm{R}} = \mathbf{k} \cdot \overline{\mathbf{V}} = \sqrt{\frac{3}{8}} \omega_{\mathrm{p}} \frac{v_{01} + v_{02}}{v_{01} - v_{02}} \tag{4.12}$$

Note that when counter-propagating streams are symmetric with equal drift velocities and densities ($v_{01} = -v_{02}$, $n_{01} = n_{02}$), oscillation frequency becomes zero. This situation can arise when a hydrogen gas is ionized by a CP laser pulse and aperiodic density modulations may develop. In the helium case, there exist asymmetric streams (e.g. the co-propagating He^{1+} and He^{2+} electrons in the CP case; the reflected He^{2+} electrons streaming against the majority of the quasi-stationary electrons in the LP case). Here asymmetric means the streams have nonzero average drift velocities, different densities, and different transverse temperatures. The fastest growing streaming mode is initially driven primarily by the co-propagating He^{1+} and He^{2+} electrons- the instability grows only in locations where co-propagating He^{1+} and

He^{2+} electrons overlap with one another. The average drift velocities of the two groups of electrons of helium ionized by a CP laser with $a_0 = 0.19$ and $\tau = 50$ fs extracted from simulations are $v_{01} \approx 0.06c$ and $v_{02} \approx 0.02c$. Substituting these numbers into Eq. (4.11) give us the values of the most unstable k and its frequency as

$$k \approx 30.6\frac{\omega_{\mathrm{p}}}{c}, \quad \omega_{\mathrm{R}} \approx 1.2\omega_{\mathrm{p}} \tag{4.13}$$

Note that the frequency of the most unstable k depends on the plasma frequency, however, the frequency for a fixed $k = k_{\mathrm{m}}$ is $k_{\mathrm{m}}\overline{V}$ which only depends on the average velocity of the two beams. A more realistic model that considers four streams with drift velocities $\pm 0.06c$ and $\pm 0.02c$ gives slightly different results. The most unstable k and its growth rate are obtained by calculating (4.6) using four streams.

$$k \approx 22\frac{\omega_{\mathrm{p}}}{c} \tag{4.14}$$

$$\gamma_{\mathrm{max,four\text{-}stream}} \approx 0.27\omega_{\mathrm{p}} \tag{4.15}$$

The fluid theory gives reasonable values of the growth rate and oscillating frequency of the streaming instability. However, there are issues about this simplified model. First, the beams are cold in the fluid model while actual beams have finite temperatures (width). Second, some key physical effects are not included, such as collisionless damping (Landau damping) and particle trapping. Therefore, theoretical growth rate from the fluid theory may be too crude to compare with experimental results and a kinetic theory is required. In kinetic theory, a plasma is modeled by the velocity distribution functions of different species and its collisionless dynamics is described by the Vlasov equation. For a plasma with an one-dimensional EVDF $f_e(v)$, the dispersion relation is given by

$$1 = \frac{\omega_{\mathrm{p}}^2}{n_0 k^2}\int \frac{f_e(v)}{(v-\omega/k)^2}dv \tag{4.16}$$

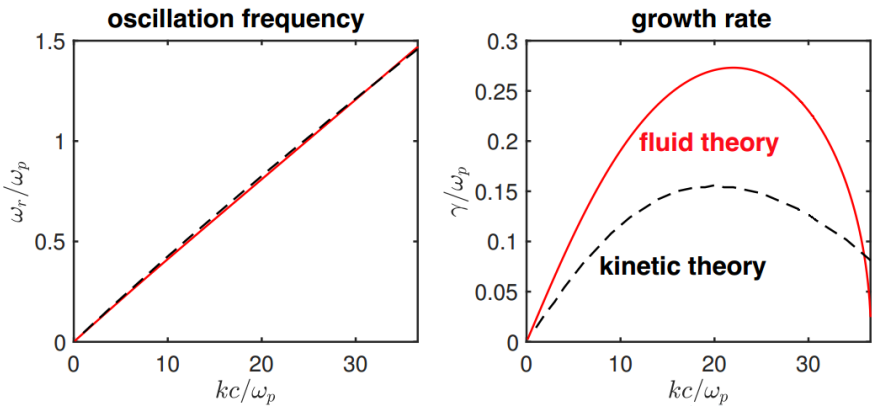

Figure 4.2: **Calculations of the oscillation frequency and growth rate of the streaming instability in the CP case.** Red curves- fluid theory using Eq. (4.6); Dashed black curve- kinetic theory using Eq. (4.17).

In our case, the dispersion function is well-approximated by drifting Maxwellian beams, it is then more convenient to express Eq. (4.16) using the plasma dispersion function $Z(\xi) = \pi^{-1}\int_{-\infty}^{\infty}\frac{e^{-t^2}}{t-\xi}dt$

$$1-\sum_j \frac{\omega_{\mathrm{p}j}^2}{2k^2v_{\mathrm{th},j}^2}Z'\left(\frac{\omega-kv_{0j}}{\sqrt{2}k^2v_{\mathrm{th},j}^2}\right)=0 \tag{4.17}$$

where $Z'(\xi) = -2[1+\xi Z(\xi)]$ is the derivative of the plasma dispersion function and ω_{pj}, v_{0j}, $v_{\mathrm{th},j}$ are the electron plasma frequency, the drift velocity, and the thermal velocity of the jth electron beam, respectively. Eq. (4.17) is numerically solved for the CP case using $v_{0,\mathrm{He}^{2+}} = \pm 0.06c$, $v_{\mathrm{th},\mathrm{He}^{2+}} = 0.015c$, $v_{0,\mathrm{He}^{1+}} = \pm 0.022c$, and $v_{\mathrm{th},\mathrm{He}^{1+}} = 0.01c$. Fig. 4.2 shows the solution of the dispersion relation from fluid theory (Eq. (4.6)) and kinetic theory (Eq. (4.17)). The most significant difference is that the growth rate from the kinetic theory is reduced, possibly due to the effect of the Landau damping.

$$\gamma_{\mathrm{max,\ CP,\ kinetic}} \approx 0.15\omega_{\mathrm{p}} \tag{4.18}$$

Next, we consider the plasma ionized by a LP laser, the transverse phase space of electrons in a 2D PIC simulation shows that most of the electrons ($\sim 80\%$) are approximately station-

ary and a small fraction of the electrons with high enough initial velocity are reflected by the ~ 2 GeV/m sheath field at the plasma-vacuum boundary and forms counter-propagating streams. The dispersion relation for the LP case in fluid theory is given by apply three streams into Eq. (4.6)

$$1 = \frac{(1-\eta)\,\omega_p^2}{2\,(\omega - k v_0)^2} + \frac{\eta \omega_p^2}{\omega^2} + \frac{(1-\eta)\,\omega_p^2}{2\,(\omega + k v_0)^2} \tag{4.19}$$

where v_0 is the drifted velocity of the reflected beams and η represents the fraction of the stationary electrons. By substituting $\eta = 0.8$ and $v_0 = 0.03c$, Eq. (4.19) is solved to get the most unstable k that gives the maximum growth rate and its corresponding frequency

$$\gamma_{\max,\mathrm{LP}} \approx 0.26\omega_p, \quad \omega_R \approx 0.8\omega_p \tag{4.20}$$

The density fluctuations associated with the streaming instability are demonstrated in PIC simulations as shown in Fig. 4.3. Even as early as 100 fs (30 μm) after the passage of the CP laser pulse a streaming instability already develops within the main body of the plasma (Fig. 4.3(a) and (b)). Here one can see density modulations in the transverse plane, i.e. perpendicular to the direction of the ionizing laser pulse. This is because the He^{2+} electrons are much more energetic than the He^{1+} electrons and their EVDF are well separated in phase space. In this case the streaming instability grows simultaneously everywhere in the plasma. The EVDF of He^{1+} and He^{2+} electrons in the LP case have an overlap Fig. 2.7(a)) so the streaming does not begin until the additional He^{2+} electron streams appear as shown in Fig. 4.1(a). This takes somewhat longer than 1 ps. Fig. 4.3(c) and (d) show that once the He^{2+} electrons are reflected by the sheath they counterstream against the rest of the lower energy electrons and the streaming instability begins at the plasma edge and spreads inwards (Fig. 4.3(d)). This is why Thomson scattering measurements demonstrated in Chapter 3 for LP case are different from the CP case- i.e. there is no streaming at 300 fs, only collective Thomson scattering from the Bohm-Gross mode.

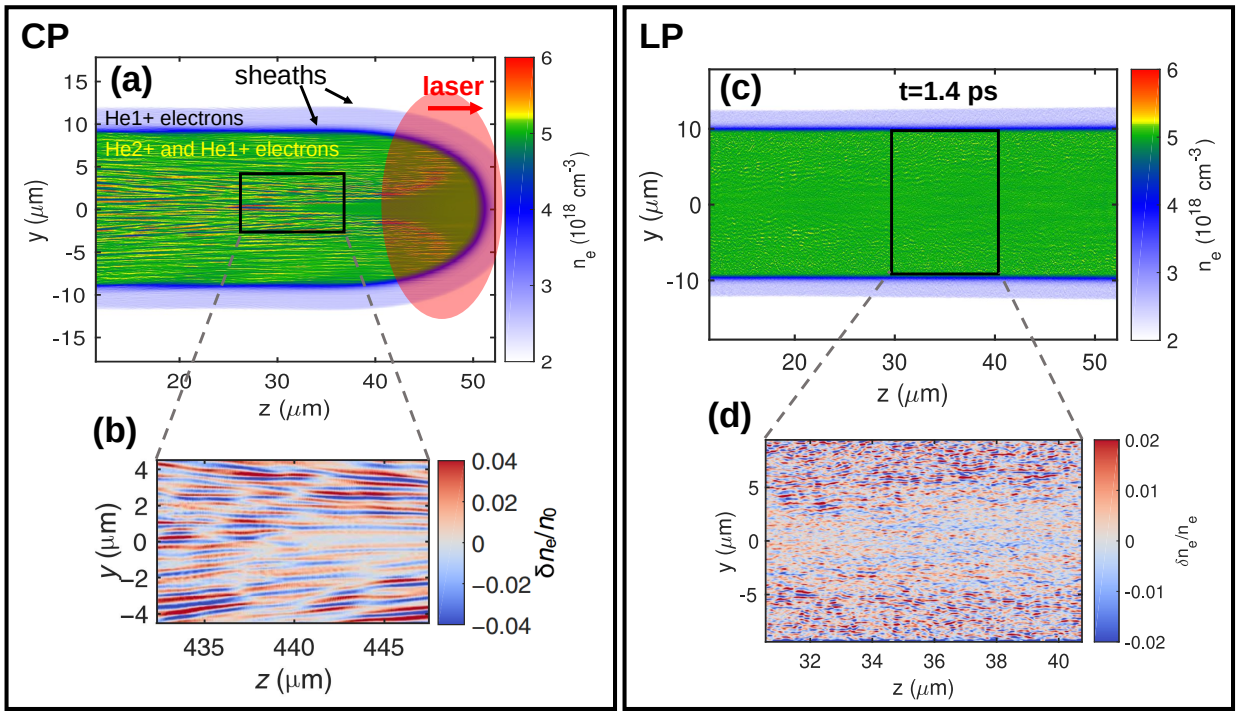

Figure 4.3: **Density fluctuations of OFI He plasma in simulations.** PIC simulations of OFI He plasmas at a density of 5×10^{18} cm^{-3} ionized using circularly (a, b) and linearly (c,d) polarized laser of . (a) Electron density right after plasma is formed by a CP laser pulse. (b) Zoom in of the regions marked by the box in (a). Electron density in the simulation box after the passage of a LP laser pulse. (d) An expanded view of a small region of the plasma density taken from (c) that shows relative density modulations near the outer region of the plasma. The unit and the color table of this subplot have been changed to emphasize the density fluctuations. The simulations use the laser pulses with the same pulse duration of 50 fs and normalized vector potentials of 0.19 (CP) and 0.27 (LP). (Courtesy to Dr. Chaojie Zhang)

4.1.3 Filamentation and Weibel instability

As stated earlier, the counter-streaming beams are also unstable to the filamentation instability due to the attraction (repulsion) between co- (counter-) propagating currents. One distinct feature of filamentation instability is the aperiodicity, which means the current (and magnetic field) fluctuations grow without oscillation. Therefore, the information of the filamentation is encoded in the zero-frequency mode. The electrostatic components of the filamentation instability driven by asymmetric streams make it possible to be probed using Thomson scattering which measures the density fluctuations.

In the nonrelativistic regime, the filamentation instability is transverse ($\mathbf{k} \cdot \mathbf{E} = 0$) when the counter-propagating currents have the same temperature so that they can pinch at the same rate. Otherwise, there will be charge separation due to the different pinching rate of the beams and the filamentation instability will contain electrostatic components [81, 82]. The dispersion relation of the filamentation instability is obtained by substituting beamlike distribution functions into the Vlasov equation and the Maxwell equations. For the electron beams (approximated by drifting Maxwellian distributions) drifting along the y direction and that have a finite temperature in the z direction, the dispersion relation for the filamentation modes is

$$\omega^2 = \omega_{\rm p}^2 + c^2 k_z^2 + \sum_j \omega_{pj}^2 \frac{v_{jy}^2 + v_{{\rm th},jy}^2}{2 v_{{\rm th},jz}^2} Z' \left(\frac{\omega}{\sqrt{2} k_z v_{{\rm th},jz}} \right) \tag{4.21}$$

where ω_{pj}, v_{jy}, $v_{{\rm th},jy}$, and $v_{{\rm th},jz}$ are the plasma frequency, the drift velocity, the beam's thermal velocity in the y, and z direction for the jth beam. The wavevector of the filamentation instability is primarily perpendicular to the streaming direction (i.e, $k_{\rm F} \approx k_z \hat{\mathbf{z}}$) but it will spread to the y direction in the k space after the induced magnetic fields drive streaming instabilities into the z direction.

The filamentation instability self-generates magnetic fields that isotropize the plasma, and along with the streaming instability quickly thermalize the non-Maxwellian structure in distribution functions. This left the anisotropic EVDV that can be approximated by

Maxwellian distributions in all directions. It is clear that Eq. (4.21) is no longer suitable for describing the later dynamics of the plasma. The mechanism of further isotropization is better being described as the thermal Weibel instability [16]. Assume the anisotropic EVDF at this stage has electron temperatures of $T_{\mathrm{th},x}$, $T_{\mathrm{th},y}$ and $T_{\mathrm{th},z}$ in the x, y, and z direction and $T_{\mathrm{th},x} = T_{\mathrm{th},y} > T_{\mathrm{th},z}$. The anisotropy is defined as $A \equiv \frac{T_{\mathrm{hot}}}{T_{\mathrm{cold}}} - 1$ where $T_{\mathrm{hot}} = T_{\mathrm{th},x} = T_{\mathrm{th},y}$ and $T_{\mathrm{cold}} = T_{\mathrm{th},z}$. The linear stability analysis gives the dispersion relation of the plasma as

$$\omega^2 = c^2 k_z^2 - \omega_{\mathrm{p}}^2 \left[A + (A+1) \frac{\omega}{\sqrt{2} k_z v_{\mathrm{th},z}} Z\left(\frac{\omega}{\sqrt{2} k_z v_{\mathrm{th},z}} \right) \right] \tag{4.22}$$

Here we have assumed that the wave vector is in the z direction and the $\mathbf{B}$ field is in the $x-y$ plane. By solving the dispersion relation, one can find the growth rate of thermal Weibel instability $\gamma = i\omega$ for unstable modes with wavevectors within the range of $0 < \frac{k_z c}{\omega_{\mathrm{p}}} < \sqrt{A}$ for any arbitrary $A > 0$. The wavevector of the unstable mode is predominantly along the low-temperature direction, i.e. $k \approx \hat{\mathbf{z}} k_z$. Thermal Weibel instability is transverse, therefore the magnetic field is predominantly along the transverse directions, namely $\mathbf{B} \approx \hat{\mathbf{x}} B_x + \hat{\mathbf{y}} B_y$ and $|B_x| \approx |B_y| \gg |B_z|$. This corresponds to the case where the plasma is ionized by a CP laser propagating along z direction. On the other hand, if the plasma is hot in one direction and cold in the other two orthogonal directions, for instance, $T_{\mathrm{th},x} > T_{\mathrm{th},y} = T_{\mathrm{th},z}$, the wavevector of the unstable mode will be $\mathbf{k} \approx \hat{\mathbf{y}} k_y + \hat{\mathbf{z}} k_z$ and the magneticfield is $\mathbf{B} \approx \hat{\mathbf{y}} B_y + \hat{\mathbf{z}} B_z$ with $\mathbf{k} \cdot \mathbf{B} = k_y B_y + k_z B_z$. This corresponds to the case where the plasma is ionized by a LP laser which polarizes along the x direction and propagates along the z direction.

Figure 4.4 shows the results of 2D PIC code simulations of the kinetic instabilities triggered by OFI in helium plasma in the CP case. These instabilities grow rapidly following the passage of the laser pulse (close to the right edge), and they are self-consistently seeded by the noise fluctuations in PIC simulations. The evolutions of electrostatic (E_y, Fig. 4.4(a)) and magnetic (B_x, Fig. 4.4(b)) fields show that both the streaming and the filamentation instabilities begin to grow soon after the plasma is created. In the linear regime that lasts for a very short time ($\ll 1$ ps), there is no coupling between these instabilities; therefore, they grow independently. The streaming instability saturates and damps very quickly (~ 1

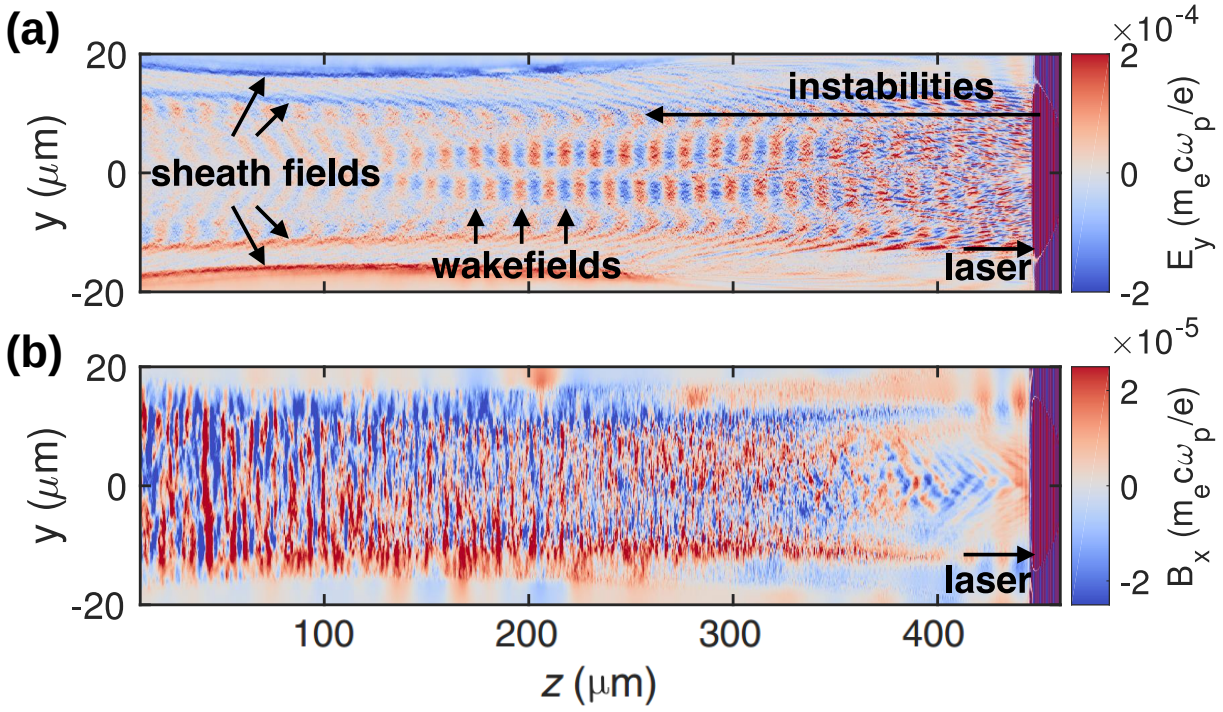

Figure 4.4: **2D simulations of OFI-triggered kinetic instabilities in a helium plasma.** (a) E_x field (b) B_x field in the He plasma ($n_e = 5 \times 10^{18}$ cm^{-3}) ionized by a CP laser (50 fs, $I = 1.6 \times 10^{17}$ W/cm^2).

ps or in ~ 300 μm in space) because of the isotropization of the counterpropagating streams caused by collisionless transverse phase space diffusion. We expect the filamentation instability which is also driven by these streams to have a similar temporal behavior. However, the magnetic field Bx continues growing past 1 ps as shown in Fig. 4.4(b), suggesting that at later time a Weibel-like filamentation instability driven by a reduced but finite anisotropy of the electrons begins to dominate in the plasma.

4.2 Short-pulse time-resolved Thomson scattering technique

In this section, a novel time-resolved Thomson scattering technique is introduced. Conventional time-resolve TS measurements are done by using a high-power long-pulse probe coupled with a time-resolved scattering light collection system, such as a spectrograph coupled with a streak camera [83]. Such a setup requires extremely high energy in the probe and special grating design to achieve a subpicosecond temporal resolution [84]. On contrary, our setup uses a short pulse with a few mJ energy as the probe and the temporal resolution is controlled by a mechanical delay line.

To match the wave vectors of unstable modes for the CP and LP cases, probe beams with two wavelengths (400 nm and 800 nm) were used with two different Thomson scattering setups (Fig. 4.5 and 4.6). In both setups, the pump pulse has a pulse duration of ~ 50 fs and a central wavelength of 800 nm. The polarization of the pump laser was changed to circular by sending the LP laser pulse through a quarter-wave plate before being focused down to a spot size w_0 of 8 μm by an F/6 OAP. The pump ionized neutral helium gas ejected from a supersonic nozzle with a diameter of 1 mm. The density of the plasma can thus be adjusted by changing the backing pressure of the jet.

After the pump beam was compressed, ~ 50% of the total energy (20 ± 4 mJ) of the pump was separated at a low-dispersion femtosecond beamsplitter (FABS) and sent out of the chamber. The use of the ultrathin beamsplitter can minimize the dispersion and self-phase modulation of the transmitted beam. Based on the desired wavelength of the probe,

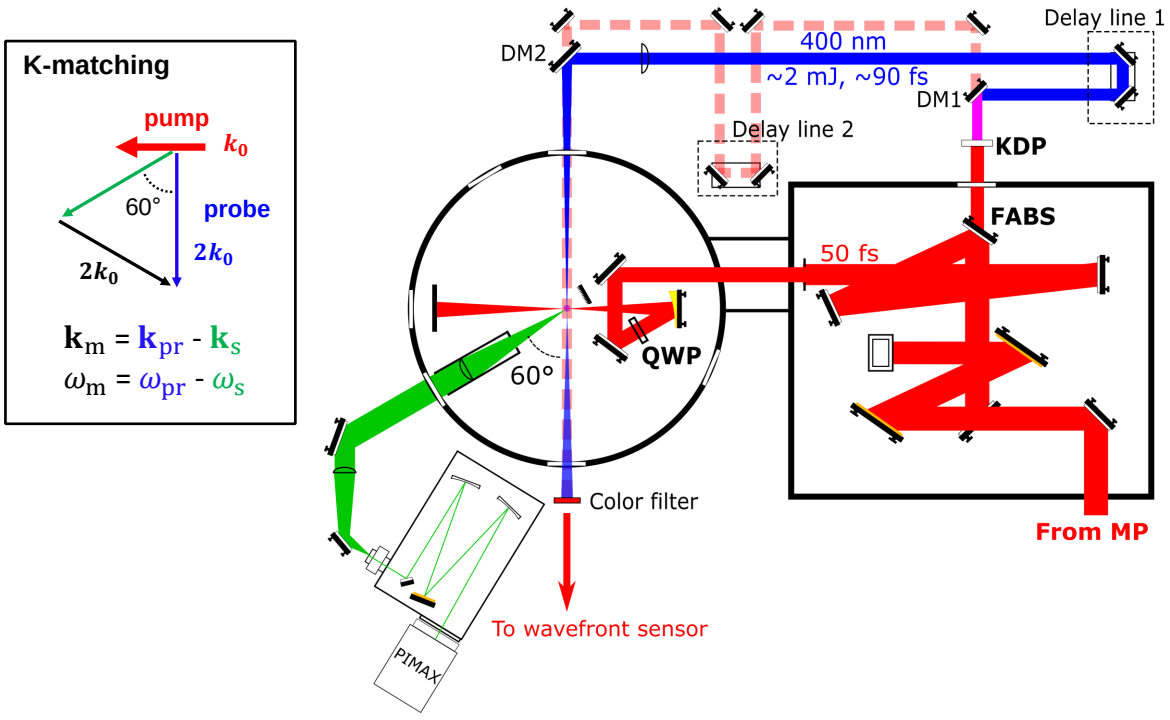

Figure 4.5: **Layout of 400 nm probe for the CP case.** Color lines: red- pump; blue- 400-nm probe; dashed light red- 800-nm auxiliary probe; green- scattering light. MP: multipass amplifier; FABS: low-dispersion femtosecond beamsplitter; QWP: quarter-wave plate; DM: dichroic mirrors.

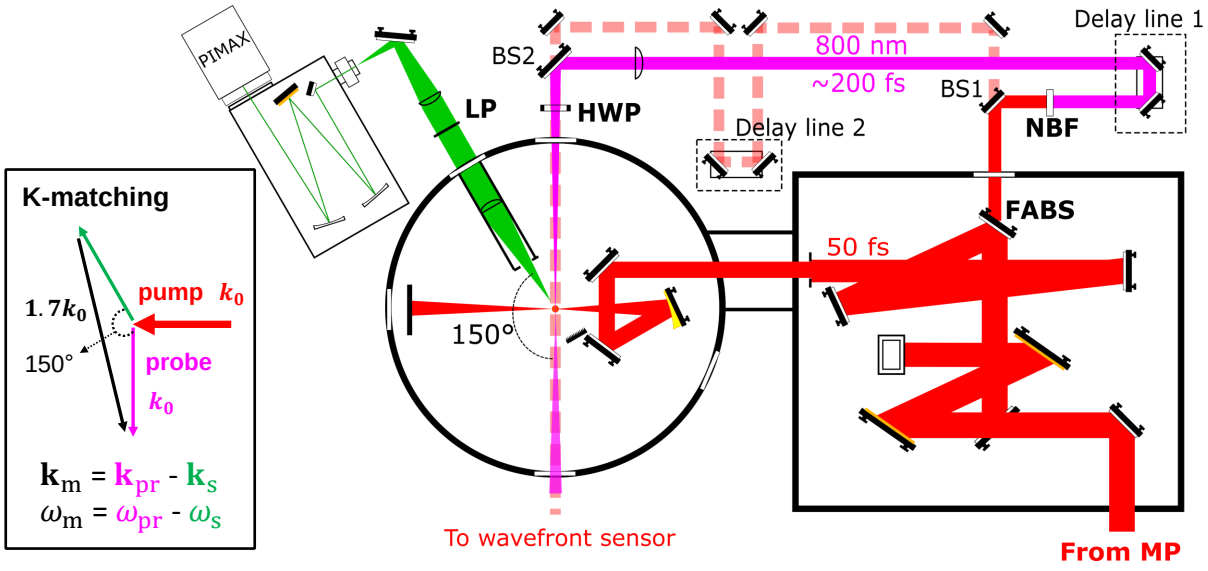

Figure 4.6: **Layout of 800 nm probe for the LP case:** Color lines: red- pump; pink- 800-nm probe; dashed light red- 800-nm auxiliary probe; green- scattering light. MP: multipass amplifier; FABS: low-dispersion femtosecond beamsplitter; NBF: narrow-band pass filter; HWP: half-wave plate; LP: linear polarizer; BS: beamsplitters. HWP and LP are inserted for mitigating stray light from the pump.

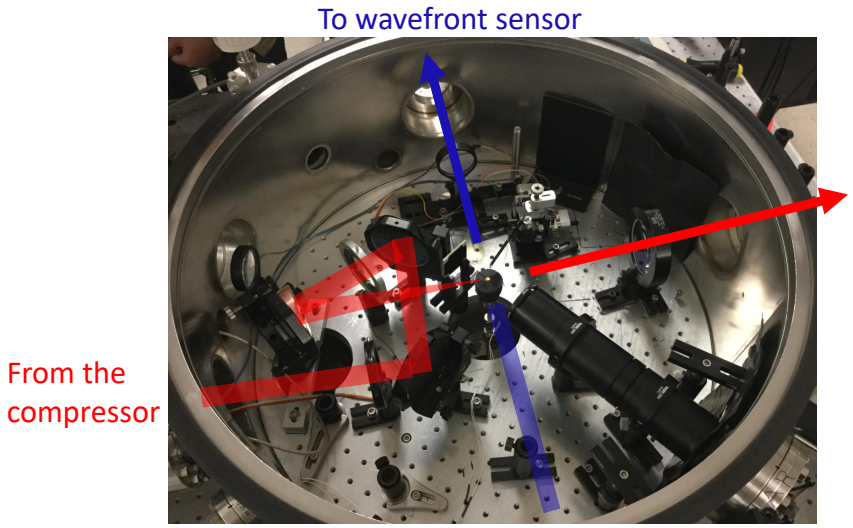

Figure 4.7: **Setup for the density measurement and synchronization inside the target chamber.**

the transmitted beam was either send through a 1.5-mm-thick KDP crystal to double its frequency or a narrow-band pass filter (NBF) centered at 800 nm to reduce the bandwidth to ~ 5 nm at the FWHM (but the pulse duration increases to ~ 200 fs). This is the primary probe beam, which is marked as the blue line in Fig. 4.5 or the pink line in Fig. 4.6, that was focused by a 75-cm lens on the plasma to generate scattered photons for diagnostics. The delay of the probe was controlled using a trombone arm (Delay line 1) with a motorized translation stage in the probe beamline. Due to the physical size of the motorized stage, the longest delay is around 100 ps. The inset of Fig. 4.5 and 4.6 show the sketch of the k-matching diagram for probing the instabilities used in our experiments. These probe wave vectors are chosen to give information about the kinetic instabilities but to avoid the effects from the wakefield.

An auxiliary probe beam (marked as dashed light red lines in Fig. 4.5 and 4.5) can be implemented if necessary. By inserting a longpass dichroic mirror or a beamsplitter into the probe beamline, a weak 800 nm beam was separated from the primary probe beam. This beam went through another trombone arm (Delay line 2) and passed the plasma without focusing. The second probe beam is versatile as it was used to measure the plasma density,

synchronize the delay time between the pump and the primary probe beam, and monitor the spatial overlap between the plasma and the probe.

In this experiment, the plasma was produced at a gas jet to reach a higher plasma density and minimize the spectral modulation of the primary probe beam from the ionization-induced frequency shift. The electron densities of the plasma produced from the jet were measured by a commercial wavefront sensor (WFS, PHASICS SID4-HR). Fig. 4.7 shows a part of setup inside the target chamber. The auxiliary probe beam with a central frequency of 800 nm and a beam size of $\sim$ 10 mm penetrates transversely through the plasma column generated by the pump beam. After passing through the plasma, the probe beam is magnified 10 times by a telescope system and sent to the camera of the WFS. Since the primary probe for TS also reaches the camera, it needs to be blocked or largely attenuated to prevent damaging of the camera. The WFS measures the phase distortion of the probe beam introduced by passing the plasma and derives the distribution of plasma density [85]. The value of the plasma density at full ionization varies with the backing pressure, the distance between the laser focus and the top of the jet, and the structure of the jet.

4.2.1 Synchronization of the pump and the probe

As demonstrated in Section 4.1, kinetic instabilities grow rapidly. Unlike the collinear setup shown in Chapter 3, there is no fixed delay between the pump and probe, so a critical issue of making a meaningful comparison between the theory and the experiment is to determine the delay between the pump and the probe. A scheme for synchronization is shown in Fig. 4.8 using a setup similar to Fig. 4.7. The top of Fig. 4.8 shows an image of the auxiliary probe captured by the WFS camera. Since the shadow of the plasma column does not extend across the field of view, the position of the pump laser can be approximated by the position of the ionization front. As shown in Fig. 4.5, two probe beams have independent delay arms and the delay between two probes (τ_{W}) can be controlled. The intensity of the focused primary probe is large enough to partially ionize gases. Once the auxiliary probe trails the primary probe ($\tau_{\mathrm{W}} > 0$), the shadow of the plasma produced in the longitudinal direction appears

as the white blob shown in the center of the image (Fig. 4.8). Therefore, we can easily find a relative delay that makes the two probes temporally overlapped ($\tau_W \approx 0$). When the two probes are synchronized, the delay between the pump and the probe can be approximated, $\tau_p \approx d_p/c$. By adjusting two delay lines to make $d_p = 0$, synchronization of the pump and the probe is achieved. We define the delay that makes $d_p = 0$ as the time zero. It should be noted that the time zero found in the experiment is not the same with the one used in simulations which is defined as the moment the pump laser passes. The difference is about 50 ± 25 fs, where the uncertainty comes from the pulse duration of the pump.

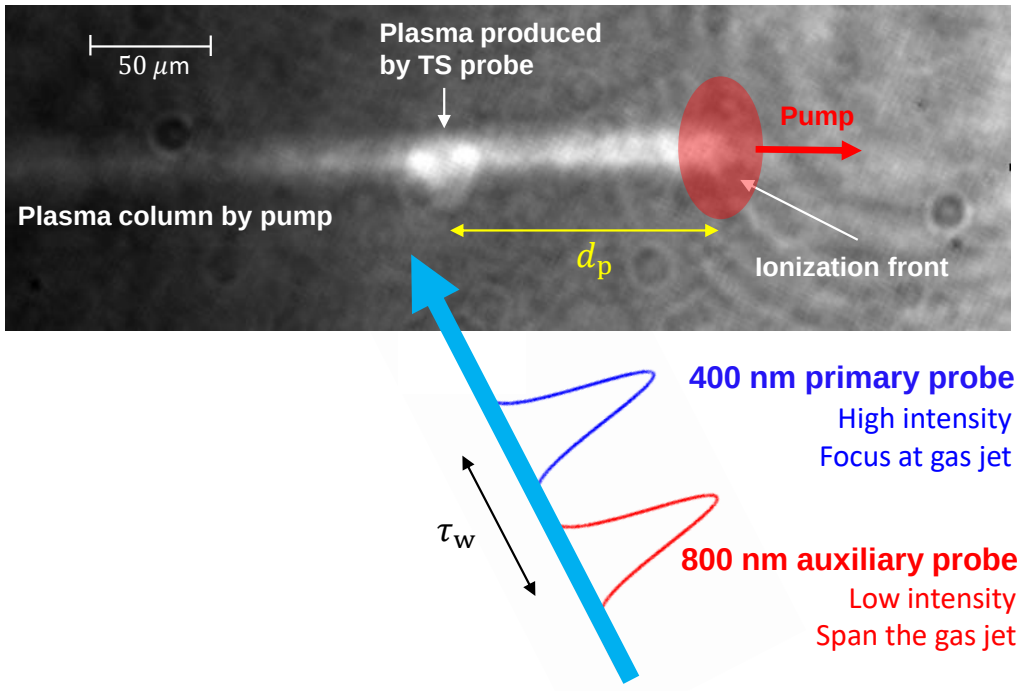

Figure 4.8: **Scheme for synchronization of the pump and probe.** The top image shows shadowgram captured by the camera. The shadow of the plasma column produced by the pump is shown as the long white band. τ_W is the delay between the primary and auxiliary probes. When $\tau_W > 0$, the shadow of the plasma produced by the primary probe appears near the center of the image. d_p is the distance between the ionization front and the position of the plasma produced by the probe.

4.3 Measurement of the growth rates of kinetic instabilities

The wave vector of the instability being measured, $\mathbf{k}_\mathrm{m}$, is determined by the k-matching condition, $\mathbf{k}_\mathrm{m} = \mathbf{k}_\mathrm{pr} - \mathbf{k}_\mathrm{s}$, as shown by the black lines in the insets of Fig. 4.5 and 4.6. The simulated signal strength is proportional to the average of$|\delta n_e(\mathbf{k})|^2$near the $\mathbf{k}_\mathrm{m}$ (blue and red dots in Fig. 4.9) where $\delta n_e(\mathbf{k})$ was calculated by 2D fast Fourier transform of the density perturbation $\delta n_e(y,z)$ inside a selected box. Fig. 4.9 shows $\left|\delta n_e\left(k_y,k_z\right)\right|$ at nearly time zero ($t = 0$ fs) and $t = 400$ fs. It can be seen from the k-space evolution of the density fluctuations that the wave vector of the instability is primarily parallel to the y direction (Fig. 4.9(a)) when the laser has just passed because the instability has the largest growth rate in the y direction. Nevertheless, after only 0.4 ps, the wave vector of the instability has spread along k_z, as shown in Fig. 4.9(b). Although the measured wave vector, $\mathbf{k}_\mathrm{m}$, is fixed by choosing a particular scattering angle, it is possible to simultaneously probe the streaming and the filamentation instabilities because they have different frequencies.

There is also a small wakefield induced by the laser pulse, as seen in Fig. 4.9(a), but it is irrelevant to the topic of this work as it simply adds an additional oscillating energy component to the longitudinal or transverse momentum of the electrons. This is so because the $\mathbf{k}$s being probed in this experiment are far off from that of the wake feature as illustrated.

4.3.1 Measure the growth of streaming instability

We first discuss the experimental results of the circular polarization case. The evolution of the TS spectra and the strength of the density fluctuation shown in Fig. 4.10 is measured with a CP pump and a 400-nm probe. In Fig. 4.10(a), each block represents a measured spectrum at a certain time delay that was controlled by Delay line 1 shown in Fig. 4.5. The temporal resolution is about 50 fs which is limited by the pulse duration of the 400-nm probe.

There are two major notable features of the spectra shown in Fig. 4.10(a). First, the electron feature grows to a saturated level and then damps in a time duration that is much

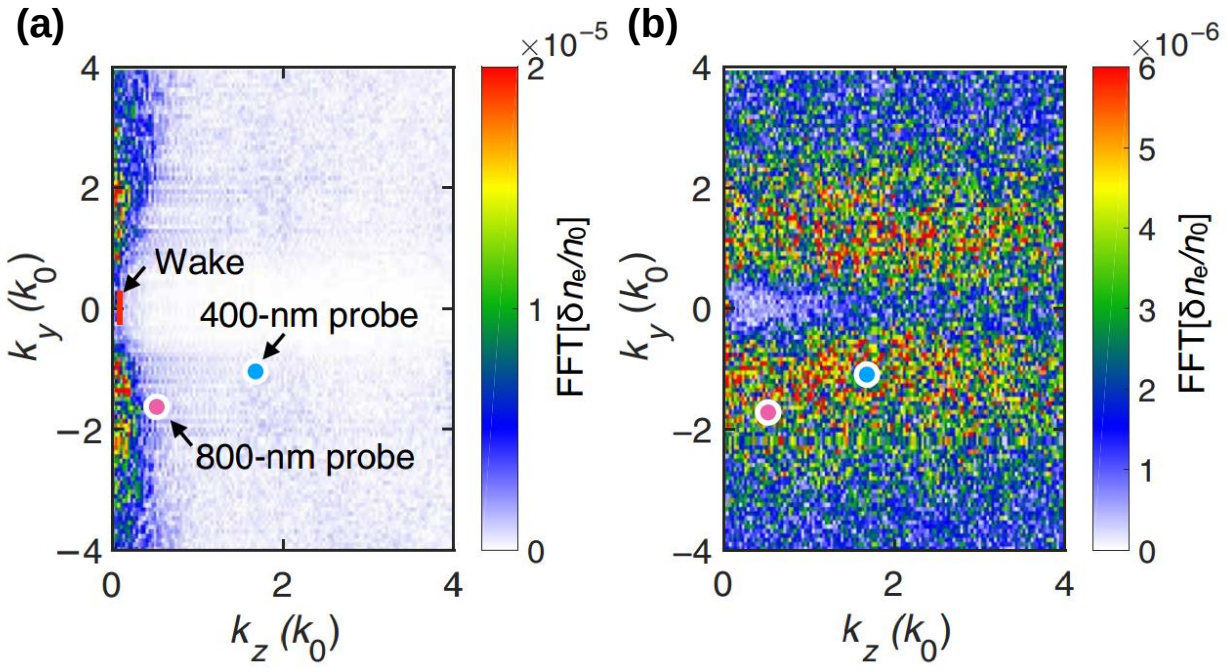

Figure 4.9: ***k*-space of the density fluctuations:** Fourier transform of the density fluctuations inside the same region but different time t after the passage of the laser pulse. (a) t = 0 fs; (b) t = 400 fs. The two dots mark the $\mathbf{k}_{\mathrm{m}}$ of the waves being measured in experiments using the 400-nm (blue dot) or 800-nm (pink dot) probes.

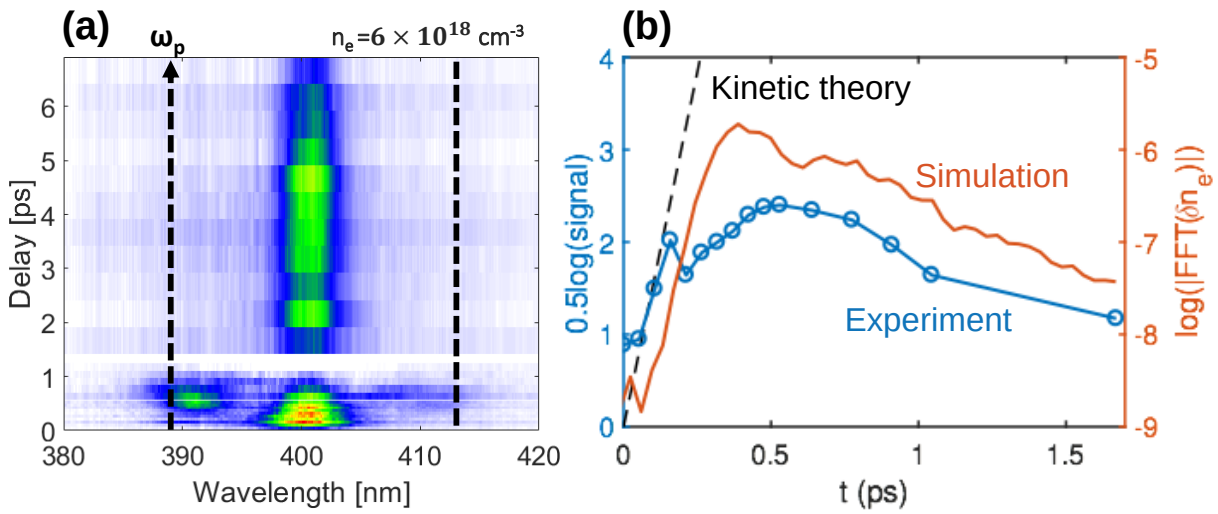

Figure 4.10: **Measurement of the growth rate of streaming instability for the CP case:** (a) The measured time-resolved TS spectra for the plasma density of 6×10^{18} cm^{-3}. (b) Comparison between the theory (dashed black), simulation (red), and experiment (blue circle).

shorter than the e-e collision time. Second, the spectral shift of the electron feature does not follow the familiar ω_p shift (black dashed lines) as would be the case if the probe photons were being scattered from the usual Bohm-Gross wave. The frequency spectrum is very broad extending from or even above ω_p all the way to the zero-frequency feature. The peak frequency of the electron feature and the existence of the zero frequency feature are essential evidence for the streaming and filamentation instabilities, respectively, while the longer-time behavior of the zero-frequency feature is consistent with the Weibel-like filamentation mode. One may also notice that the blue satellite of the electron feature is somewhat stronger than the red satellite. In other runs (Fig. 4.11(a)-(c)), the asymmetry also exists. Although the physical reason for this asymmetry is not yet understood, the signals of both satellites grow and damp as predicted from the theory.

The amplitude of the blue shifted electron satellite is plotted in Fig. 4.10(b) as a function of the probe delay in log scale (blue circles) for 0-1.7 ps. The signal (data in arbitrary units of counts) is raised to the power of 0.5 to obtain a quantity that is proportional to the wave

amplitude (density fluctuation) since the measured signal is proportional to the scattered power, which in turn is proportional to the square of the density fluctuations [72]. The red line shows the wave amplitude obtained from a 2D PIC simulation performed using the experimental parameters. The black dashed line shows the initial (exponential) growth rate predicted by the kinetic theory. We note that apart from an ~ 100 fs offset the temporal variation of the measured signal shows a very good agreement with the kinetic theory and simulations. Some of this discrepancy in the time of onset is due to an uncertainty in knowing the shape of the rising intensity of the laser pulse, the uncertainty in measuring the relative delay between the plasma pump and the probe (~ 50 fs) and differences in the noise level between the experiment and the simulations. The instability grows at the expense of the directional energy of the electrons; therefore, the growth rate of the instability decreases with time until it saturates at ~ 0.5 ps ($\sim 70\,\omega_{\mathrm{p}}^{-1}$) and then begins to damp. The nonlinear phase of the instability follows, when the change of the distribution function due to the interaction of the waves with electrons is significant, and lasts for about another 0.5 ps. During this phase some of the electrons' directional energy transferred to the electrical field energy of the unstable waves is returned back to the electrons via electron trapping. As a result of these wave-particle interactions the transverse phase space diffuses and the process of isotropization begins.

The measurements for three different plasma densities are shown in Fig. 4.11(a), (b), and (c). A similar transient appearance of the electron feature in TS spectra is observed. For each of these measurements we calculated the initial growth rate and the frequency of the fastest growing mode. The results are shown as magenta circles in Fig. 4.11(d) and (e), respectively. The blue lines show predictions of the kinetic theory calculated using Eq. (4.17). The green squares in Fig. 4.11(d) show the 2D simulation results of the growth rate of the instability at the measured wave vector $\mathbf{k}_{\mathrm{m}}$ (i.e., $k_y = -k_0$, $k_z = 1.7k_0$). The frequency of the instability shown in Fig. 4.11(e) is calculated using the spectral shift of the peak of the blue satellite (Fig. 4.10(a) and 4.11(a)-(c)) when the instability reaches a maximum. The measured initial growth rates show reasonable agreement with the theory. One of the

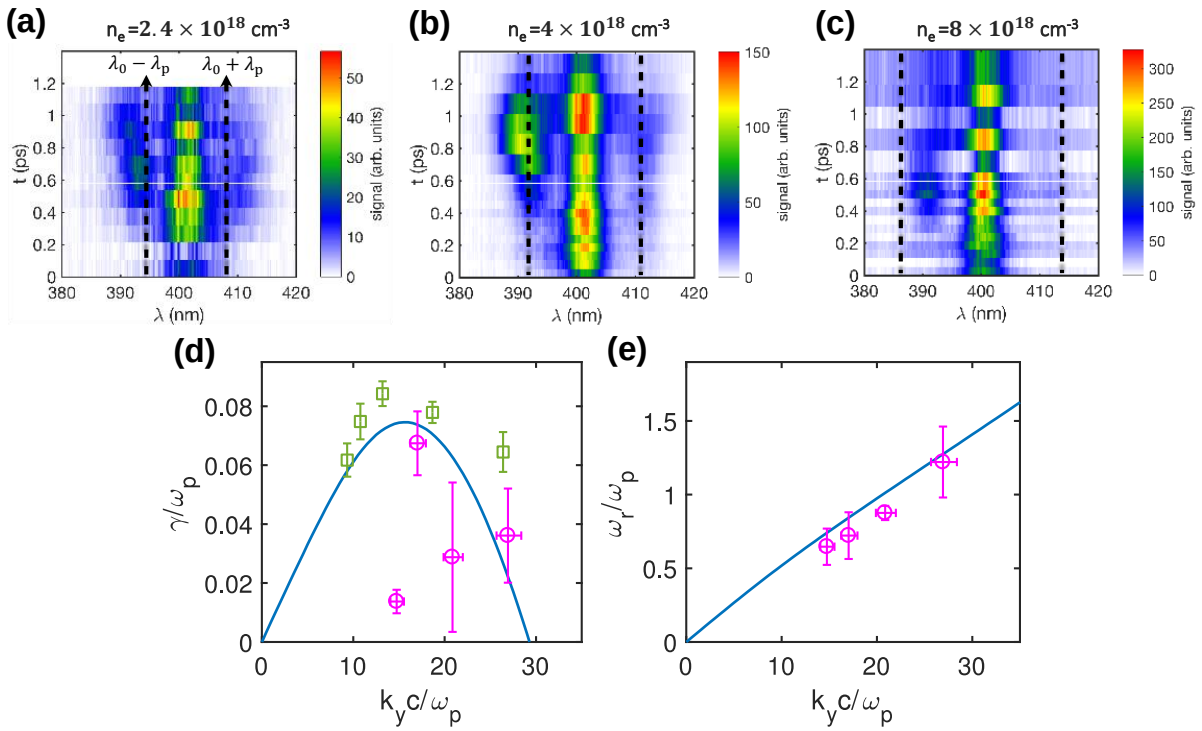

Figure 4.11: **Growth rate and oscillation frequency of the streaming instability**. Time-resolved TS spectra in the CP case for three plasma densities of (a) 2.4×10^{18}, (b) 4×10^{18}, and (c) 8×10^{18} cm^{-3}. These three cases, along the case shown in Fig. 4.10(a), are used to produce magenta circles in (d) and (e). (d) Measured (magenta circles), predicted (blue line), and simulated (green squares) growth rates of the instability. (e) Measured (magenta circles) and predicted (blue line) frequencies of the streaming instability.

possible reasons why the measured growth rate is smaller than the analytical prediction might be the competition between the streaming and the filamentation instabilities which would tend to reduce the former's growth rate. Collisions may also reduce the growth rate of the instability [86].

In contrast, the measured and predicted frequency (from the kinetic theory) of the streaming instability shows an excellent agreement for two reasons. First, the oscillation frequency of the filamentation instability is near zero so that it will not affect the frequency of the streaming instability even if there is a coupling between these two instabilities. Coupling will generate waves with additional ks and hence broaden the phase velocities of the coupled modes. Second, as explained before, the frequency of the streaming instability is given by $\omega \approx \mathbf{k}_\mathrm{m} \cdot \mathbf{v}_\mathrm{d} = k_y v_\mathrm{d}$ where $v_\mathrm{d} \approx 0.04c$ is the drift velocity between the co-propagating He^{1+} and He^{2+} electrons. Because of the large spread in both $\mathbf{k}_\mathrm{m}$ and $\mathbf{v}_\mathrm{d}$, a wide spread of unstable streaming modes is seen to grow in the TS electron spectrum (Fig. 4.10(a) and 4.11(b)). The frequency of the streaming modes driven by the counter-streaming He^{1+} (He^{2+}) species is zero because the two beams are symmetric, therefore they do not contribute to the measured electron feature.

The phase velocity of the streaming instability is $v_\phi \equiv \frac{\omega}{k} \approx v_\mathrm{d} \cos\theta_\mathrm{d}$, which is independent of the plasma density. Here θ_d is the angle between the wavevector $\mathbf{k}$ and the drift velocity $\mathbf{v}_\mathrm{d}$. This is confirmed in the experiment as shown in Fig. 4.11(e) where the measured oscillation frequency of the instability follows the analytical prediction, which is almost linear with a slope of v_ϕ. As described earlier, initially the wavevector of the streaming instability is primarily along the streaming direction so that $\cos\theta_\mathrm{d} \sim 1$ and therefore $v_\phi \approx v_\mathrm{d}$, thus strong resonance occurs between the co-propagating He^{1+} and He^{2+} electrons, as evidenced by the energy gained by He^{1+} electrons and energy lost by He^{2+} electrons seen in Fig. 4.1(a). This resonant interaction hastens the collisionless phase space diffusion from initially double donut-shaped distribution to a single quasi-Maxwellian distribution in approximately 1 ps, leaving a bi-temperature distribution (hot in the transverse plane but cold in the longitudinal direction) which is unstable to the Weibel-like filamentation instability.

4.3.2 Measure the growth of filamentation and Weibel instability

The non-oscillating filamentation and Weibel instabilities have near zero frequencies [78] (hereafter referred to as the zero-frequency feature). As explained earlier, the filamentation and Weibel mode will also have an electrostatic component [78, 81] that can be probed by the TS diagnostic. Kinetic theory (Eq. (4.21)) enables us to predict the frequency, and the growth rates of the unstable modes being probed as a function of time at different plasma densities so that a comparison can be made between the theory, simulations and the experiment.

In Fig. 4.12(a) we plot the measured growth of the zero-frequency feature (green squares) and the electron feature (blue circles) together, to illustrate the very similar behavior of these two signals. Following a rapid growth both decay within $\sim$ 1 ps. For the $\mathbf{k}$ being probed the zero frequency filamentation mode is actually first to appear above the measurement threshold followed by the streaming mode but both have similar growth rates. Following a rapid growth both decay within $\sim$ 1 ps, a time duration shorter than the ion plasma period ($2\pi\omega_{\mathrm{pi}}^{-1} \approx 3$ ps) which suggests that the zero-frequency mode corresponds to instabilities instead of the usual ion acoustic waves.

Fig. 4.12(b) shows the initial growth rate of the filamentation mode, where the magenta circles show the measurements (Fig. 4.10(a) and 4.11(a)-(c)) and the green line shows the prediction of the kinetic theory. Once again, a very reasonable agreement between the measurements and the kinetic theory is seen. We note that kinetic theory predicts that there may also be a non-oscillating branch of the streaming instability. The growth rates of the two is very comparable and therefore this non-oscillating branch of the streaming instability likely contributes to the measured zero-frequency feature. However, it is the recurrence of the measured zero frequency feature (see Fig. 4.12(c)) that the strongest indicator of the filamentation/Weibel instability since recurrence of the streaming mode is not expected once the streams no longer exist.

In Fig. 4.12(c) the green line shows the temporal evolution of the zero-frequency feature in our experiment (400-nm peak in the spectra shown in Fig. 4.10(a)), which clearly shows

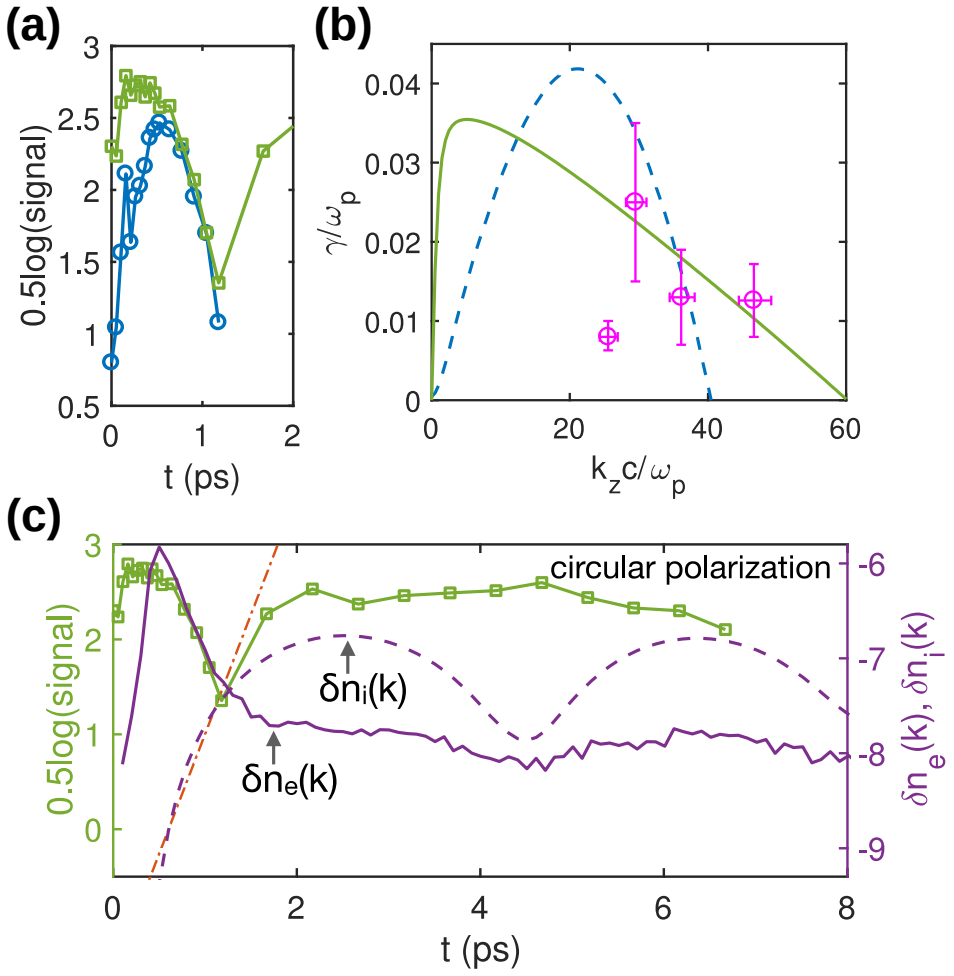

Figure 4.12: **Measurement of the filamentation-Weibel instability.** (a) Magnitude of the signals at zero-frequency (green) and of the electron feature (blue). (b) The measured (magenta dots) and calculated (green line) initial growth rate of the filamentation instability. The horizontal error bars show the uncertainty of density measurement, and the vertical error bars represent the standard error of the deduced growth rate. The blue dashed line shows the growth rate of the zero-frequency mode of the streaming instability. (c) The green line shows the measured magnitude of the zero-frequency mode as a function of time (Fig. 4.10(a)). The solid (dashed) purple line shows the evolution of the amplitude of the electron (ion) density fluctuation at the same k that is being probed in the experiment. The red dotted-dashed line shows the maximum growth rate of the Weibel instability calculated by the kinetic theory.

two distinct peaks. The first peak (0-1 ps) is likely due to the filamentation instability, which rapidly reduces the anisotropy of the EVDF. The second peak (1-7 ps) is shown in simulations consistent with a Weibel instability driven by the residual anisotropy in the distribution function. In our simulations we cannot model both ionization of He and ion motion at the same time. The latter is important for accurately determining the electrostatic component of the Weibel instability directly. Therefore, we performed a simulation where the plasma was pre-ionized and had an EVDF similar to that of the OFI plasma. In this simulation, the motion of He ions was self-consistently included. The amplitude of the density fluctuations of electrons (δn_e) and ions (δn_i) at $\mathbf{k}_\mathrm{m}$ as a function of time are shown in Fig. 4.12(c) by the solid and dashed purple lines, respectively. The evolution of electron density fluctuation $\delta n_e(\mathbf{k}_\mathrm{m})$ shows a peak at $t \approx 0.5$ ps, which tracks the first peak of the measured zero-frequency feature fairly well. Because there has not been enough time for the heavy ions to follow the motion of electrons, the filamentation instability contributes to the electron density fluctuations through the different pinching rates of the electron streams. However, as time progresses the scale length of these density fluctuations evolves to longer k allowing the Weibel instability to grow to detectable levels through the ion density fluctuations. In the experiment this manifests as the recurrence of the zero-frequency feature while in the simulations this is seen as the growth of the ion density fluctuations after the first ~ 2 ps as shown by the dashed purple line. After that $\delta n_i(\mathbf{k}_\mathrm{m})$ reaches a saturated level with small-amplitude oscillations. The oscillation period is 3.7 ps which is slightly longer than the ion plasma period (3 ps) but agrees with the ion acoustic wave frequency that corresponds to $T_e = 150$ eV. In Fig. 4.12(c) we also show the theoretical growth rate of Weibel instability by the red dot-dash line. This line represents the maximum Weibel growth rate ($\gamma \approx 0.02\omega_\mathrm{p}$) calculated using the simulated EVDF at $t = 1$ ps, which shows a good agreement with both the simulated and the measured ion density fluctuations. We should note that kinetic theory predicts that the unstable range of Weibel instability covers $0 < k < \sqrt{A}\omega_\mathrm{p}/c$ [87] which is much smaller than $|\mathbf{k}_\mathrm{m}|$. However, it has been shown that the unstable k of Weibel instability can extend to large k through turbulence cascade [88, 89].

4.3.3 Streaming instability in the LP case

In contrast to the CP case where electron streams are directly initiated by the ionization process, in the LP case the initial EVD consists of two 1D Maxwellian distributions that do not have a clear bump on tail distribution that is unstable to kinetic instability [90] and therefore the electron streams are established only after the hotter He^{2+} electrons have bounced off the sheath electric field at the plasma-vacuum boundary (see Fig. 4.1(b)). Fig. 4.13(a) shows the measured time-resolved TS spectra in the LP case. The electron feature becomes prominent ~ 1.5 ps after the passage of the laser pulse. The growth rate of the streaming instability in the LP case is smaller because only a small fraction of the electrons is reflected to drive the streaming instability. Therefore, it takes a longer time for the streaming instability to grow and saturate. This prediction was also confirmed in the experiment as shown in Fig. 4.13(b), where the blue circles show the measured magnitude of the streaming instability (blue satellite in Fig. 4.13(a)) whereas the red line shows the corresponding simulation result. A remarkable agreement is found between the measurements and the

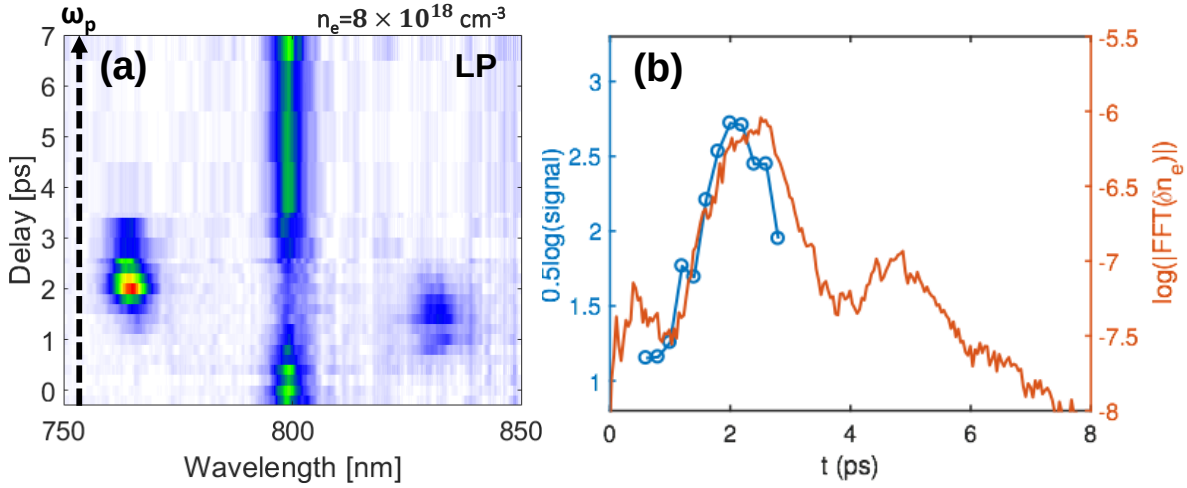

Figure 4.13: **Measurement of the growth rate of streaming instability for the LP case.** (a) The measured time-resolved TS spectra for the LP pump. (b) Measured (blue) and simulated (red) evolutions of the magnitude of the electron density fluctuations of the streaming instability.

simulation. When making this comparison, the fully kinetic PIC simulation can also be seen as giving the prediction of kinetic theory. In other datasets, we observed the recurrence of the streaming mode and the same phase relationship between the streaming and the zero-frequency mode.

In the LP case, the instability is driven by the reflected electrons as they propagate through the majority of slower moving electrons, therefore has a nonzero oscillation frequency of $\omega \approx \mathbf{k}_\mathrm{m} \cdot \mathbf{v}_\mathrm{d} = k_y v_\mathrm{d}$ where v_d is the drift velocity of the reflected electrons. The frequency spectrum of this mode is narrower than in the CP case since there are only two streams in the LP case. Fig. 4.14 shows the measured spectra at a fixed delay (t = 1.8 ps) where the shifts of the electron features of both colors are recorded for different plasma densities. As shown in Fig. 4.14(b), the shifts are clearly smaller than the shift from the plasma frequency but the oscillation frequency ($\omega \propto \Delta\lambda$) increase slightly with the densities. It suggests in this case there is a small positive correlation between the drift velocity and the plasma density. This could be the result of a stronger bounday sheath field as the plasma density becomes higher. One can also observe from the electron feature of the time-resolve spectra that the red satellite not only grows earlier but also saturates faster than the blue one. The reason for this phenomenon remains as a mystery.

4.4 The thermalization of an OFI plasma

The thermalization process of an OFI plasma is discussed in this section. The important role of kinetic instability in the evolution of an OFI plasma has been demonstrated in experiments and simulations. After the initialization of distribution functions, the non-Maxwellian and anisotropic plasma is subject to various kinetic instabilities. Two dominant mechanisms in early stage is the streaming and filamentation instabilities, which grow and damp nearly simultaneously in $\sim$ 1 ps ($\sim$ 6 ps in the LP case). Thereafter, the thermal Weibel instability becomes the dominant instability, isotropizing the anisotropic Maxwellian plasma. At this stage, the dynamics of an OFI plasma becomes more complicated because the effects of collisions and plasma expansion may need to be taken into consideration. Thermal Weibel

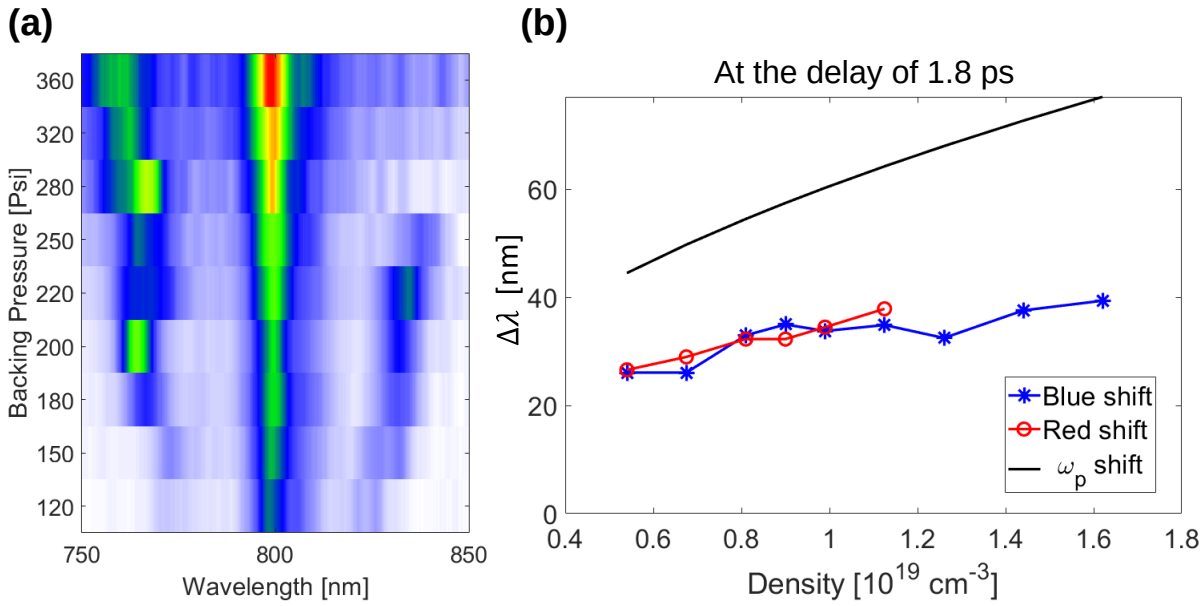

Figure 4.14: **Oscillation frequency of the unstable mode for different plasma densities in the LP case.** (a) The TS spectra with various backing pressures captured at a fixed delay t = 1.8 ps. The backing pressure 200 psi corresponds to a plasma density of 8×10^{18} cm^{-3}. (b) The peaks of the frequency shifts of the blue and red satellites at different plasma densities. The black line shows the shift of the plasma frequency in the range of experimental parameters.

instability and electron-electron collision are considered two competing thermalization mechanisms of plasma electrons. Even after the electron distribution is thermalized (becomes isotropic Maxwellian), because the electron temperature is expected be much higher than the ion temperature, the thermalization between electrons and ions will continue. At the same time, the expansion of the plasma further cools the plasma. These complicated and intertwined physical effects coexist in an experiment. However, we are able to separate and distinguish some of these effects in computer simulations. In the following, the results of PIC simulations and long-term TS spectra evolution are demonstrated and give us insight about the thermalization process of an OFI plasma ionized by a CP laser pulse.

4.4.1 Isotropization of the plasma electrons

We have tracked the evolution of the EVDF and the temperature anisotropy ($A \equiv \frac{T_\perp}{T_\parallel}$) of the OFI plasma in a 2D simulation and the results are shown in Fig. 4.15. In this simulation the ionization and evolution of the plasma was self-consistently modeled but Coulomb collisions were not included to isolate the effect of the instabilities on the temperature anisotropy. The left panel of 4.15 shows the transverse and longitudinal velocity distributions of electrons within a thin slab ($\Delta z = 2\ \mu$m) in the 2D simulation at $t = 0$, 1 and 10 ps. As can be seen in Fig. 4.15(a), the initial transverse distribution is highly nonthermal. The initial distribution has an extremely low temperature (~ 1 eV) in the longitudinal direction (py-px distribution). However, the multiple beam structure disappears in 1 ps (Fig. 4.15(b)) due to the collisionless phase space diffusion (Landau damping and particle trapping by the waves excited on/by the streams and the $\mathbf{v} \times \mathbf{B}$ motion of the electrons due to filamentation and Weibel modes). The distribution approaches to a quasi-Maxwellian within a few ps (Fig. 4.15(c)). Consequently, the rms temperature $T_\perp$ drops while the rms temperature $T_\parallel$ increases significantly.

As a result of these kinetic instabilities, the anisotropy of the plasma drops rapidly from an initial value of a few hundreds to ≈ 10 within 1 ps, as shown by the blue line in Fig. 4.15(d). Thereafter, the Weibel instability continues to isotropize the plasma but with a

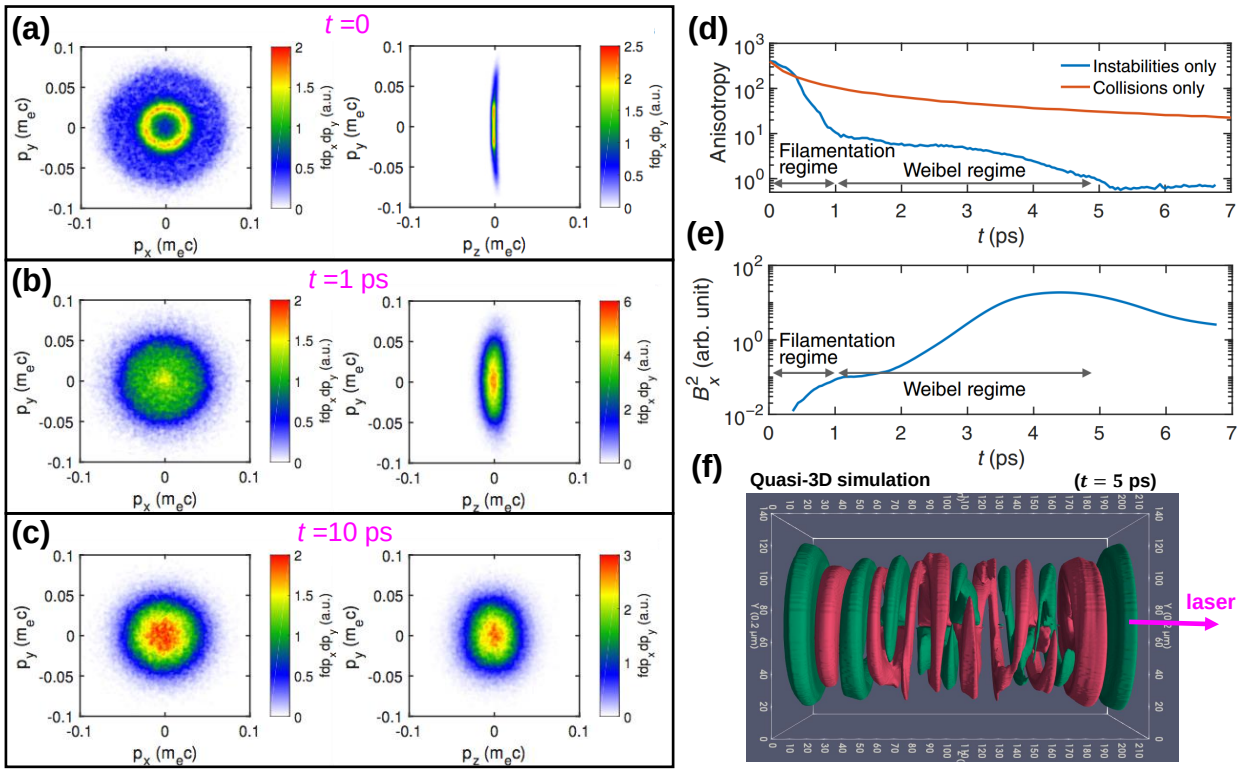

Figure 4.15: **Evolution of the temperature anisotropy and the self-generated magnetic field of the OFI plasma in the CP case.** The 2D EVDF in the plane $(p_y - p_x)$ perpendicular and the plane $(p_y - p_z)$ parallel to the laser propagation direction z at three delays of (a) $t = 0$, (b) $t = 1$, and (c) $t = 10$ ps. (d) The blue line shows the simulation of anisotropy evolution without collisions. The red line shows the simulation of anisotropy evolution of a preionized plasma with only Coulomb collisions. (e) The average magnetic field energy as a function of time shows two distinct growth phases corresponding to filamentation and Weibel regimes, respectively. (f) 3D isosurface plot of $\boldsymbol{B}_y$ field at 5 ps.

smaller rate to further reduce the anisotropy to be ¡1 in about 7 ps. The magnetic fields (Fig. 4.15(e)) also show two distinct growth phases that correspond to the filamentation and the Weibel instability, respectively. Simulation shows that, as the Weibel instability saturates, the magnetic fields self-organize to a quasi-static helical structure (Fig. 4.15(f)) as predicted in [87].

To ensure that such a rapid drop of the anisotropy is due to instabilities, we performed a simulation using a pre-ionized plasma with similar initial EVDF (represented by the red lines in Fig. 4.15(d)) and included only the Coulomb collisions (both e-e and e-i). Without the presence of the kinetic instabilities, electrons exchange their energy (momentum) efficiently through the e-e (e-i) collisions so that they isotropize and thermalize after tens of ps. It can be seen that except for the first a few hundred fs, the anisotropy in this collision-only simulation drops much slower than that in the simulation which only includes instabilities. Therefore, we confirm that the collisions do not play a significant role in the first ten ps after the formation of the plasma over the range of plasma densities used and that during this time, the isotropization of the plasma is dominated by the kinetic instabilities. Nevertheless, collisions will eventually thermalize the plasma.

4.4.2 Thermalization of the plasma electrons

Fig. 4.16 shows the Thomson scattering spectra evolution for OFI He plasmas produced by circularly polarized pump pulses. Each blue line represents the average spectrum of multiple shots measured at a delay τ_p. As we have discussed earlier, simultaneous growing of the sideband (electron) and zero-frequency features correspond to the streaming and filamentation instabilities respectively. Both signals damp within 1 ps, and then the second peak of the zero-frequency feature appears due to the Weibel instability. The saturation of this mode occurs at $\sim$ 5 ps agreeing well with the simulations (Fig. 4.15(e)). On contrary, the electron feature does not show up until $\tau_p > 50$ ps. The reappearance of the electron feature coincides with the saturation of the third phase evolution (10-100 ps) of the zero-frequency feature.

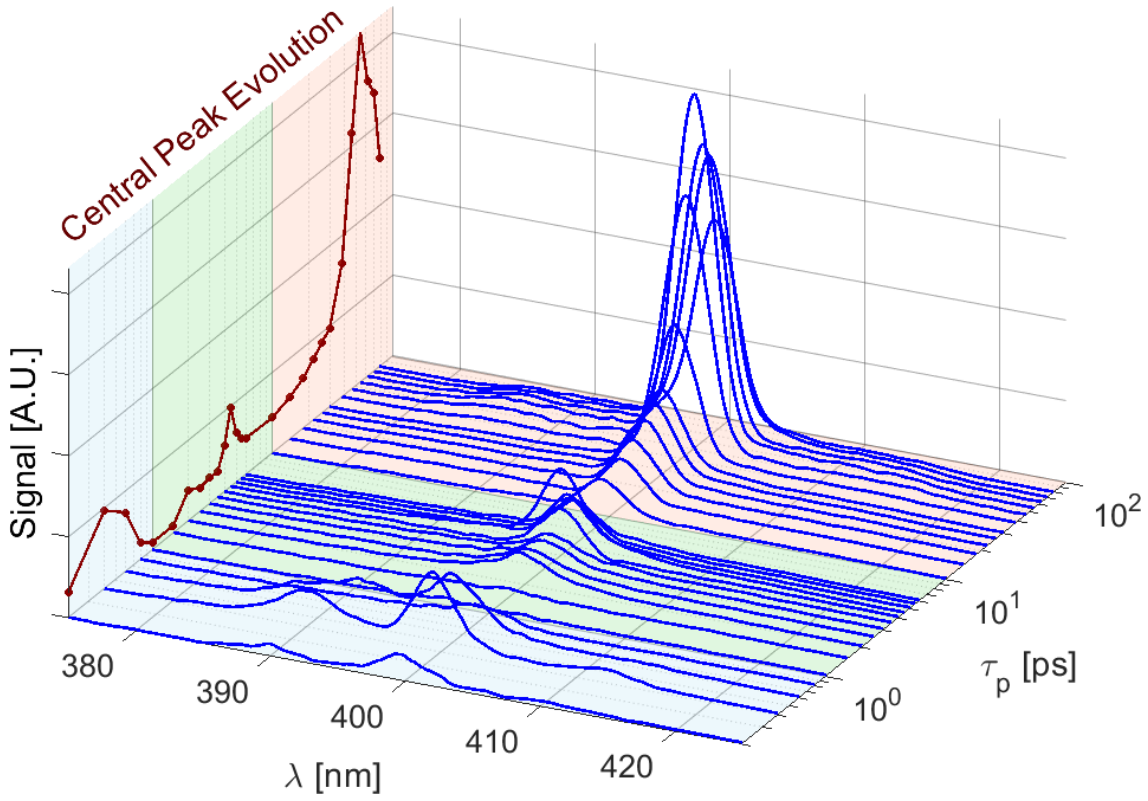

Figure 4.16: **Long-term evolution of TS spectra in the CP case.** TS spectra were collected from the helium gas jet ionized by CP laser pulses at a backing pressure of 150 psi ($\sim 6 \times 10^{18}$ cm^{-3} at full ionization). Each blue line represents the averaged spectrum of 10 shots at the same delay (0 ~ 97 ps). The brown curve traces the peaks of the zero-frequency feature at different delays.

The long-term evolution of the OFI plasma involves the self-generating magnetic fields. Shown in 3D PIC simulations, the magnetic fields self-organize into a quasi-static helical structure within a few ps [91]. Recent experiments using electron beams to probe the magnetic fields in OFI He plasmas show the magnetic structure lasts for tens of ps in underdense plasmas [92]. When a plasma is magnetized, TS spectra reflect the coupling of the longitudinal and transverse modes (hybrid resonance) [72]. The helical magnetic structure means

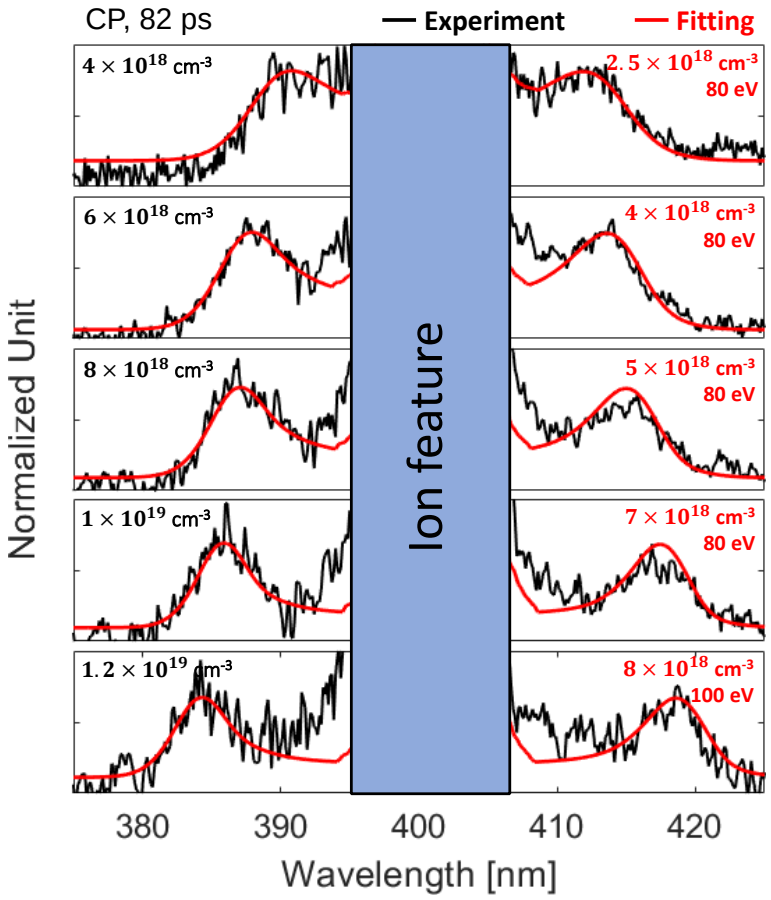

Figure 4.17: **Fitting the electron features of TS spectra at a late delay.** The experimental spectra (black) were taken for different backing pressures (values in black are plasma densities measured by PHASICS). The best fit for each case is shown as the red curve using the parameters (temperature and density) shown in red. The ion features of these spectra are not fitted.

there are many modes resonant at different frequencies. Mixing of these modes would result in the smoothing of any possible high-frequency TS feature. This may be the reason we can only see the collective Thomson scattering electron feature after tens of ps (after the magnetic field damps) even though plasma electrons are expected to become nearly thermalized earlier.

At the final stage of spectral evolution, the density-dependent collective Thomson scattering signature shows up and these spectra are fitted assuming a Maxwellian distribution. Fig. 4.17 shows the measured TS spectra and their fits at τ_p = 82 ps for different backing pressures. The results are consistent with that there is an fixed amount ($\sim 35\%$) of plasma density drop and a similar thermalized temperature of 80-100 eV. It should be noted that we did the same measurement for the plasma ionized by a linearly polarized laser, but a thermalized spectral feature has not been found at a later delay (up the limit $\sim$ 97 ps) in this case. This implies that it may take a longer time for OFI plasmas in the LP case to become thermalized or unmagnetized, despite its initial distribution is closer to a Maxwellian one.

4.5 Summary

In this chapter we have shown that an ultrafast OFI helium plasma with a known polarization-dependent anisotropic EVDF [93] is susceptible to kinetic streaming, filamentation, and Weibel instabilities. We have measured the growth rates and frequencies of these instabilities using time-resolved TS. The measurements are compared against self-consistent PIC simulations and theory with good agreements. In addition to these cases, it is possible to generate other EVDF as shown in Chapter 2. For instance, by using an elliptically polarized laser to ionize the He atoms, one can initialize counterpropagating streams along one direction (Fig. 2.7(b)). The drift velocity and the transverse temperature of these streams can be controlled by changing the polarization ellipticity and therefore can be used to suppress one of the (streaming or filamentation) instabilities. Because the EVDF are predominantly determined by the OFI process, one may expect similar instabilities even in solid density

plasmas. The growth of the instabilities will be faster ($\gamma \propto \omega_{pe}$), the wavelength of the predominant mode will be shorter ($\lambda \propto c\omega_p^{-1}$), and the lifetime may be shorter because of an extremely high collision rate. Therefore, one may require the use of femtosecond soft x-ray laser pulses to probe these instabilities in solid-state plasmas. Simulations show that the most unstable **k** of the instability changes as the plasma evolves, which can be confirmed by simultaneously collecting the scattered light from multiple angles. One can simultaneously measure the time evolution of the electron and ion features at several **k**s, which will enable the hierarchy of kinetic instabilities to be established [94] and track the evolution of the plasma from a quiescent to turbulent state [23].

CHAPTER 5

Effect of Optical Angular Momentum on Second-Harmonic Generation by an Intense Laser in Underdense Plasmas

A plasma is generally considered as a nonlinear medium. However, normally there is no second order nonlinearity when a plane electromagnetic wave propagates in an infinite, homogeneous plasma that acts as an isotropic medium. But by breaking this symmetry by using a finite diameter plasma with sharp density gradients or by using a tightly focused high intensity light pulse, a second harmonic (2ω) beam can self-generate when an intense laser pulse passes through the plasma. Second-harmonic generation (SHG) from a plasma has been considered as a potential light source and a diagnostic tool for the plasmas [95, 96]. In the Thomson scattering experiments using the 2ω beam generated from a nonlinear crystal as the probe, the self-generated 2ω radiation is a major source of stray light and its spectral signal has to be removed. It is also found that the self-generated 2ω light has some unique properties especially when the pump beam carries angular momentum. In this chapter, the angular momentum properties of 2ω light generated by an intense laser in a underdense plasma are extensively studied in the non-relativistic regime.

The total optical angular momentum of an optical beam, which is the sum of the spin angular momentum (SAM) and orbital angular momentum (OAM), is found to be conserved in this second order nonlinear process. Whereas energy and linear momentum conservation demand that two fundamental photons are required to generate one second harmonic photon and that the 2ω photons are emitted in the same direction as the fundamental photons in an underdense plasma, conservation of the total angular momentum requires the conversion

of spin angular momentum of a circularly polarized (CP) light pulse into the orbital angular momentum of the second harmonic. This is verified by measuring the helical phase of the 2ω radiation generated in an underdense plasma using a pump beam with a known spin and orbital angular momentum. The source of the 2ω photons are also determined by analyzing near field intensity distribution of the 2ω light. The images are consistent with these 2ω photons being generated due to the intensity gradients of the pump beam as predicted by the combined effect of spin and orbital angular momentum when Laguerre- Gaussian (LG) beams are used.

5.1 Interaction of beams with angular momentum and plasmas

A paraxial light beam can carry two types of angular momentum, commonly called spin angular momentum and orbital angular momentum. The former is due to the beam's polarization state while the latter arises from its spatial mode [97]. Such beams are known to produce distinct effects on mechanical objects. For instance, a circularly polarized beam is known to exert a torque on a suspended birefringent disc [48]. More recently, a vortex beam with a helical phase front has been shown to induce rotation of trapped particles [98, 99]. These effects are the result of angular momentum transfer from light to microscopic objects. While the beam polarization is associated with the rotation of particles about their own axis, the helical phase front of the beam makes particles rotate about the beam axis. This independent but simultaneous effect of spin and orbital angular momentum has been used in sophisticated manipulation of nanoparticles [100, 101, 102] and has enabled numerous applications [103, 104]. Unlike the interaction between SAM/OAM light and neutral matter, the interaction between such light and plasma is less studied, although the latter too is expected to be governed by the conservation laws for energy, momentum, and angular momentum.

While the transfer of energy and linear momentum in laser-plasma interactions has been extensively studied [105, 106], there are but a handful of theoretical studies on how the angular momentum is transferred from a laser beam to either the plasma electrons or secondary photons that may be produced during laser-plasma interaction. For instance, it has been

theoretically shown that OAM light can be effectively coupled to electron plasma/ion acoustic waves through stimulated Raman and Brillouin (parametric) instabilities respectively [107]. It has also been theoretically demonstrated that the angular momentum of light can be transferred to a plasma wakefield using a spatiotemporally shaped beam [108]. There are proposals to use intense OAM laser pulses for creating a suitable wake for electron/positron acceleration [109, 110, 111], ion acceleration [112], radiation emission [113], and magnetic field generation [114, 115]. Most of these applications require vortex beams with relativistic intensity. Ultrashort, high-intensity pulses that initially have no SAM or OAM can be converted to vortex beams that do, by passing them through a spiral phase plate [112, 116]. However, in order to avoid damaging optical materials or inducing phase distortion, large aperture optics are required. Furthermore, experimental outcomes are strongly affected by the temporal and spatial quality of the vortex beams. The focusing of a vortex beam is extremely sensitive to off-axis low-order aberrations [117], which leads to spatial inhomogeneity of the focal spot profile. These problems have limited the experimental verification of many of the theoretical proposals mentioned above.

Using a plasma medium to generate intense vortex beams is tempting since plasmas have no damage threshold. Various theoretical ideas have been proposed to generate vortex beams using plasmas, such as spin-to-orbital angular momentum conversion [118, 119], high harmonic generation from laser interaction using solid target plasmas [120, 121], and stimulated Raman scattering [122]. Despite these proposals, there are few experiments due to the highly nonlinear nature of these processes on the one hand and the experimental difficulties mentioned above on the other. Through an experimenter's point of view, the process of second harmonic generation in plasma as a platform to study the conversion of spin-to-orbital angular momentum and the conservation laws for spin, orbital and total angular momentum is attractive since it is arguably a well understood nonlinear process. Gordan et al. [118] proposed a scheme to generate 2ω pulses with equal units of OAM and SAM by converting circularly polarized, Hermite-Gaussian laser photons to second harmonic at the extremely sharp density gradients that exist at the sheath of a blown-out wake of a plasma accelera-

tor. Recently, preliminary studies [123] have purported to show the spin-to-orbital angular momentum conversion during second harmonic generation in an underdense plasma. In this work the authors assume a priori that the total angular momentum (the sum of SAM and OAM) is conserved during the generation process. The conservation of OAM and SAM has been demonstrated in high harmonic generation in noble gases [124, 125], the conservation rule for the total angular momentum has yet to be verified for plasmas.

5.2 Second-harmonic generation by laser pulses with angular momentum in underdense plasmas.

Second harmonic generation from a laser plasma source occurs when symmetry of the medium is broken. Second harmonic radiation has been detected from underdense plasmas (laser frequency ω_0 larger than the plasma frequency ω_p) in several experiments using relativistic laser intensity. For majority of these experiments, second harmonic light has been correlated with density gradients transverse to the propagation direction of the laser beam. When the laser intensity becomes ultrahigh, the ponderomotive force radially expel electrons and generate an electron density cavitation [126, 95, 127]. Second harmonic currents are induced as the quiver electrons (free electrons oscillating in the laser field) passing through density gradients. Also with ultrahigh laser intensity, the effect of the magnetic field becomes comparable to that of the electric field, leading to the nonlinear electron quiver motion and synchrotron-like harmonic radiations [128].

For non-relativistic intensity, the dominant sources of second order nonlinearity in an underdense plasma can be narrowed down to two first-order perturbation effects. Both effects come from the density perturbation δn induced by the electron quiver motion in the laser field but they have different physical interpretations. The first is associated with the crossing of the quiver electrons in the ionization induced density gradients. Initial density gradient can be found at the boundary of a plasma medium or the boundary layers between different ionic species in the case of optical-field multi-step ionization [129]. In this case, the

second harmonic current is directly proportional to the magnitude of the density gradient ∇n_0. The second, is associated with quivering electrons in the intensity gradient where the perturbed electron trajectories lead to second harmonic emission. The first source is referred as the density gradient (dg) contribution and the second as the intensity gradient (ig) contribution. It is usually hard to determine which of these two mechanisms is dominant in a given experiment. Due to their distinctly different physical origins, two contributions can be discerned by the spatial distribution of the 2ω photons within the plasma as well as the interplay between SAM and OAM as shown in this section.

5.2.1 Quiver electron model

The SHG mechanisms are studied by calculating the electron oscillatory motion of the plasma electrons in the laser field (also known as the quiver model). For a paraxial beam with arbitrary angular momentum, we may write the complex electric field near the focus ($z = 0$) in terms of Laguerre-Gaussian (LG) mode as

$$\mathbf{E} = (\hat{\mathbf{x}} + i\sigma\hat{\mathbf{y}})\, E_p^l(\rho)\, e^{i(kz-\omega_0 t+l\phi)} e^{i\psi(z)} \tag{5.1}$$

where

$$E_p^l(\rho) = E_0 \left(\frac{\sqrt{2}\rho}{w_0}\right)^{|l|} e^{-(\rho/w_0)^2} L_p^{|l|}\left(\frac{2\rho^2}{w_0^2}\right) \tag{5.2}$$

where k is the wave number, $\rho = \sqrt{x^2+y^2}$ is the radial coordinate, $\phi = \tan^{-1}(y/x)$ is the azimuthal coordinate, w_0 is the focal spot size, $\psi(z) = (|l| + 2p + 1)\tan^{-1}(z/z_\mathrm{R})$ is the Gouy phase, z_R is the Rayleigh range, E_0 is the peak electric field strength, and $L_p^{|l|}$ is the associated Laguerre polynomials with the radial index p and the azimuthal mode index l. The SAM value of the beam is determined by the polarization state, where $\sigma = 0$ for linear polarization (LP) and $\sigma = \pm 1$ for left-circular (LCP) and right-circular (RCP) polarization. The OAM value of the beam is determined by the azimuthal index (also known as the topological charge) $l = 0, \pm 1, \pm 2, \cdots$. The Gouy phase term is ignored in most calculations by assuming

$z \sim 0$.

Consider the free electron motion in an underdense plasma under the influence of the electric field described by Eq. 5.1. In this calculation, circular polarized ($\sigma = \pm 1$) beam and the radial index $p = 0$ are considered for simplicity. The resultant electron quiver velocity can be written as $\mathbf{v}_\mathrm{q} = i\left(\hat{\boldsymbol{x}} \pm i\hat{\boldsymbol{y}}\right) v_{\mathrm{q}0}\left(\rho\right) e^{i(kz-\omega_0 t+l\phi)}$ where $v_{\mathrm{q}0}\left(\rho\right) = eE_0^l\left(\rho\right)/m_e\omega_0$. The electron current density due to the quiver motion is $\mathbf{J}_\mathrm{q} = -en\mathbf{v}_\mathrm{q}$, where $n = n_0 + n_1$ is the electron density which includes the ambient plasma density n_0 and the density fluctuation n_1. Then assume that $n_1 = \bar{n}_1 \exp\left[i\left(kz - \omega_0 t + l\phi\right)\right]$ and linearize the continuity equation to obtain $n_1 = \left(i/\omega_0\right)\left(\nabla n_0 \cdot \mathbf{v}_\mathrm{q} + n_0 \nabla \cdot \mathbf{v}_\mathrm{q}\right)$. Note that here we have assumed $\nabla n_0 \gg \nabla n_1$ and $n_0 \gg \bar{n}_1$ which are valid only for non-relativistic limit.

The nonlinear components of the current density $\mathbf{J}_\mathrm{q}$ are found to be second-harmonic ($\propto E^2$) in the first-order perturbation and denoted as $\mathbf{J}_2$, which is

$$\mathbf{J}_2 = -i\frac{e}{\omega_0}\left(\nabla n_0 \cdot \mathbf{v}_\mathrm{q} + n_0 \nabla \cdot \mathbf{v}_\mathrm{q}\right)\mathbf{v}_\mathrm{q}. \tag{5.3}$$

The first term on the right-hand side of Eq. 5.3 describes the nonlinear current generated at initial transverse density gradients. Large density gradients are found in laser ionized plasmas at the plasma-neutral gas boundary layer or at the boundaries between different ionic species. As shown in Chapter 2, barrier suppression ionization (BSI) leads to an extremely sharp density gradient near the region where the laser exceeds the threshold intensity for ionizing a specific atom/ion [56]. In the present experiment He gas is ionized by a short, intense laser pulse. In this case, the plasma has large two "shells" density gradients- the first between the region of the doubly and singly ionized He ions (He^{2+}-He^{1+}) and the second between the singly ionized He and neutral gas (He^{1+}-He). We denote the second harmonic current density from the density gradient contribution by $J_{2\mathrm{dg}}$ and it is proportional to the magnitude of the density gradient and the local laser intensity. Unlike the density gradient contribution that only depends on the local value of the intensity, the spatial distribution of the 2ω current from the intensity gradient is modulated depending on the relative value of the beam's polarization (SAM) and helical phase front (OAM). This is because the quiver

electron motion in the field gradient will be azimuthally perturbed when there is an additional azimuthal phase term $e^{il\phi}$. The current density from this effect will be referred as $J_{2\mathrm{ig}}$.

It is illuminating to expand the two terms on the right-hand side of Eq. (5.3) separately in the cylindrical coordinate system (r, ϕ, z). For the density gradient contribution, we have

$$\mathbf{J}_{2\mathrm{dg}} = \left(-i\hat{\boldsymbol{\rho}} \pm \hat{\boldsymbol{\phi}}\right) C_{\mathrm{j}} \left(\partial n_0/\partial\rho\right) \left[E_0^l(\rho)\right]^2 e^{i[2k_1 z - 2\omega_0 t + 2(l\pm1)\phi]}. \tag{5.4}$$

For the intensity gradient contribution, we have

$$\mathbf{J}_{2\mathrm{ig}} = \left(-i\hat{\boldsymbol{\rho}} \pm \hat{\boldsymbol{\phi}}\right) C_{\mathrm{j}} n_0 \left[(|l| \mp l)\left(\frac{\rho}{w_0}\right)^{-1} - 2\left(\frac{\rho}{w_0}\right)\right] \left[E_0^l(\rho)\right]^2 e^{i[2k_1 z - 2\omega_0 t + 2(l\pm1)\phi]} \tag{5.5}$$

where $C_{\mathrm{j}} = e^3/m^2\omega_0^3$ is a constant, $k_1 = k_0\left(1 - \omega_p^2/\omega_0^2\right)^{1/2}$ is the wave number in the plasma, and the upper (bottom) signs correspond to the left (right)-handed CP. Eq. (5.5) shows a radial current distribution not only depending on the azimuthal index l but its relationship with the polarization. The calculations of the radial distribution of $\mathbf{J}_2$ from each contribution are shown in Fig. 5.2(a) (for the case $l = 0$) and 5.3(a) (for the case $l = +1$) by substituting a laser intensity of 1.5×10^{17} W/cm^2 and $w_0 = 3$ μm in Eq. (5.4) and (5.5).

5.2.2 Experimental setup and near-field images

In the experiments a short laser pulse with variable LG mode and polarization (certain well-known combinations of spin and orbital angular momentum) was focused to a "moderate" peak intensity inside a helium-filled chamber. The intensity of the pulse is high enough to create a fully ionized region by OFI in a finite region within and surrounding the laser spot but is well below the relativistic regime where the plasma electrons begin to oscillate close to the speed of light ($\sim 2 \times 10^{18}$ W/cm^2 for 800 nm). This way the relativistic effects are minimized on the one hand and a combination of relativistic self-focusing and ponderomotive force of the ultrashort laser pulse is not high enough to generate a significant transverse electron density depression on the other hand. The back-fill pressure of helium was set low

to avoid plasma-induced refraction of the pulse.

The experimental setup is shown schematically in Fig. 5.1. The pump laser pulse has a central wavelength of 800 nm and a pulse duration of ~ 50 fs (full width half maximum). The vacuum chamber was filled with a static fill-pressure of 10 torr of He gas. Helium was ionized by focusing the pump beam by an OAP with a f-number of 12. To ensure a full ionization at the focus, different pump energies were used for different input modes to keep the peak intensity larger than 1.5×10^{17} W/cm^2, which is far beyond the ionization threshold of He^{1+} ion. A blue glass (Newport BG40) was placed after the focus to block most of the 800 nm pump beam energy but allow the transmission of the 400 nm beam. The divergent 2ω radiation was then collimated by a lens pair and was guided into different detection systems. For most measurements, another band-pass filter (centered at 406 nm with a bandwidth of 40 nm) was inserted in front of the detector to block stray light and plasma line emission. SAM and OAM of the input beam were introduced by a zero-order quarter-wave plate (QWP) and a spiral phase plate (SSP). Since the incident beam had a top-hat (super-Gaussian) intensity profile, the output beam of the SPP is better described as a modified Laguerre-Gaussian beam. The modified LG beam has slightly different intensity profile at the focal plane compared with the fundamental mode [117].

The spatial locations where the density and intensity gradient contributions are expected to be dominant respectively are shown in Fig. 5.2(a) for a fundamental, $l = 0$ mode LG beam. The current due to the intensity gradient contribution $J_{2\mathrm{ig}}$ (blue curve) follows the intensity gradient (gray dashed curve) whereas the density gradient contribution is the largest near the positions where the BSI threshold intensities are reached for ionizing neutral He (brown dotted line) and He^{1+} (green dotted line). Fig. 5.2(b) shows the measured 800 nm beam profile of this mode and Fig. 5.2(c) and 5.2(d) show the measured near field 2ω images (color) and the expected positions of the of the largest intensity gradient (dashed circles) respectively for this case. There is an excellent agreement between the measured distributions of the 2ω photons and the expected contour of the peak emission assuming the intensity gradient contribution is dominant. These 2ω images have the expected annular

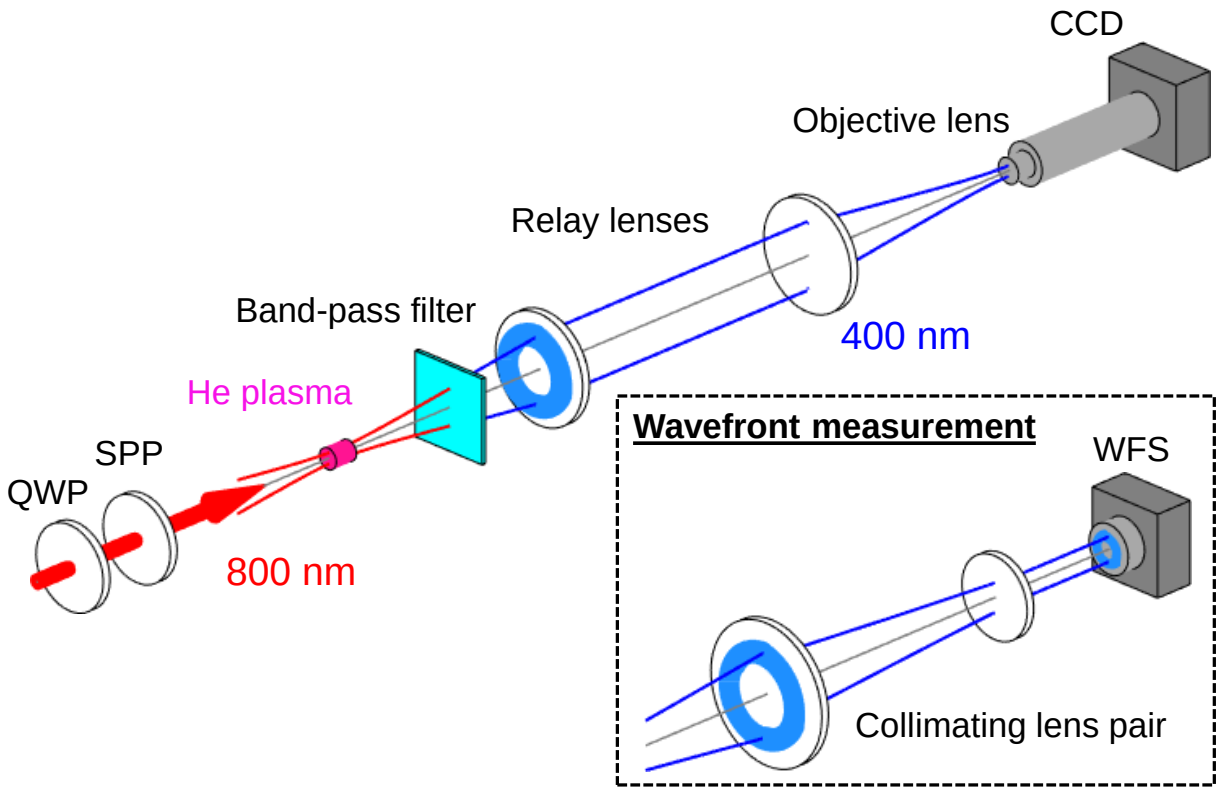

Figure 5.1: **Experimental setup.** Schematic of set-up used to characterize the second-harmonic generation near-field and the far field (inset). Relay lens pair images the plasma exit to the objective lens. An ultrashort (50 fs (FWHM)), 800 nm laser pulse, containing up to 10 mJ of energy with controlled amount of SAM and OAM generated second harmonic light in plasma formed by optical field ionization (OFI) of static helium gas to give a plasma density of $\sim 6.6 \times 10^{17}$ cm^{-3}. The 2ω light (400 nm) was transmitted by a band-pass filter and transported out of the chamber. QWP: quarter wave plate; SPP: spiral phase plate. The imaging system was replaced by the diagnostics shown in the inset for wavefront measurement. In this setup, the 2ω light was down collimated by a lens pair and then sent to a wavefront sensor (WFS).

shape from the intensity distribution but they have azimuthal inhomogeneities thought to arise from aberrations in the input beam. However, note that no detectable amount of 2ω radiation is observed where the density gradients are the largest.

When $l \neq 0$, the radial distribution depends on the value $(|l| - \sigma l)$ (as shown in Eq. 5.5) which is a quantity depending on both the SAM value σ and OAM value l. $J_{2\text{ig}}$ is calculated for $\sigma = \pm 1$ and $l = 1$ in Fig. 5.3(a), where the distributions of the intensity (black curve) and intensity gradient (gray dashed curve) of the LG_0^1 are also shown. However, the distributions of $J_{2\text{ig}}$ for the LCP and the RCP cases are quite different now compared to those for the $l = 0$ shown in Fig 5.2. When σ and l have the same sign, a broad ring (red curve) is expected that has a radius larger than radius of the peak intensity position of the LG_0^1 mode. On the other hand, when σ and l have opposite signs, two rings are expected to appear - one on either side of the intensity peak. The stronger inner ring should be accompanied by a weaker outer ring in contrast to the previous case. This feature has been confirmed in the corresponding 2ω images shown in Fig. 5.3(c) and 5.3(d). The excellent agreement between the measured emission and the calculated peak location further confirms that the 2ω photons are emitted from the plasma region where the laser intensity gradients are the largest rather than ionization induced density gradients.

High degrees of asymmetry of the intensity distribution were observed in the near-field images shown in Fig. 5.2(c)(d) and 5.3(c)(d). Minor asymmetry was also found in the focal spot profiles of the fundament beams (Fig. 5.2(b) and 5.3(b)), suggesting the inhomogeneity originated from the fundamental beams and that the nonlinear conversion process may have accentuated it. From other tests (not shown) using 800 nm beams with various azimuthal index l, the focal spot asymmetric distribution appears when a larger incident beam size is used. The aberraion is dependent on the sign of the azimuthal index and its effect increases with the larger mode values. This may be the reason why the Fig. 5.3(c) (larger $|l_{2\omega}|$, Case D in Table 1) has significantly poorer profile. Similar spatial inhomogeneities have been observed in other OAM experiments using high-power or/and large-aperture vortex beams [112, 121, 116, 130, 131]. Ohland et al [117] has studied this phenomenon and concluded

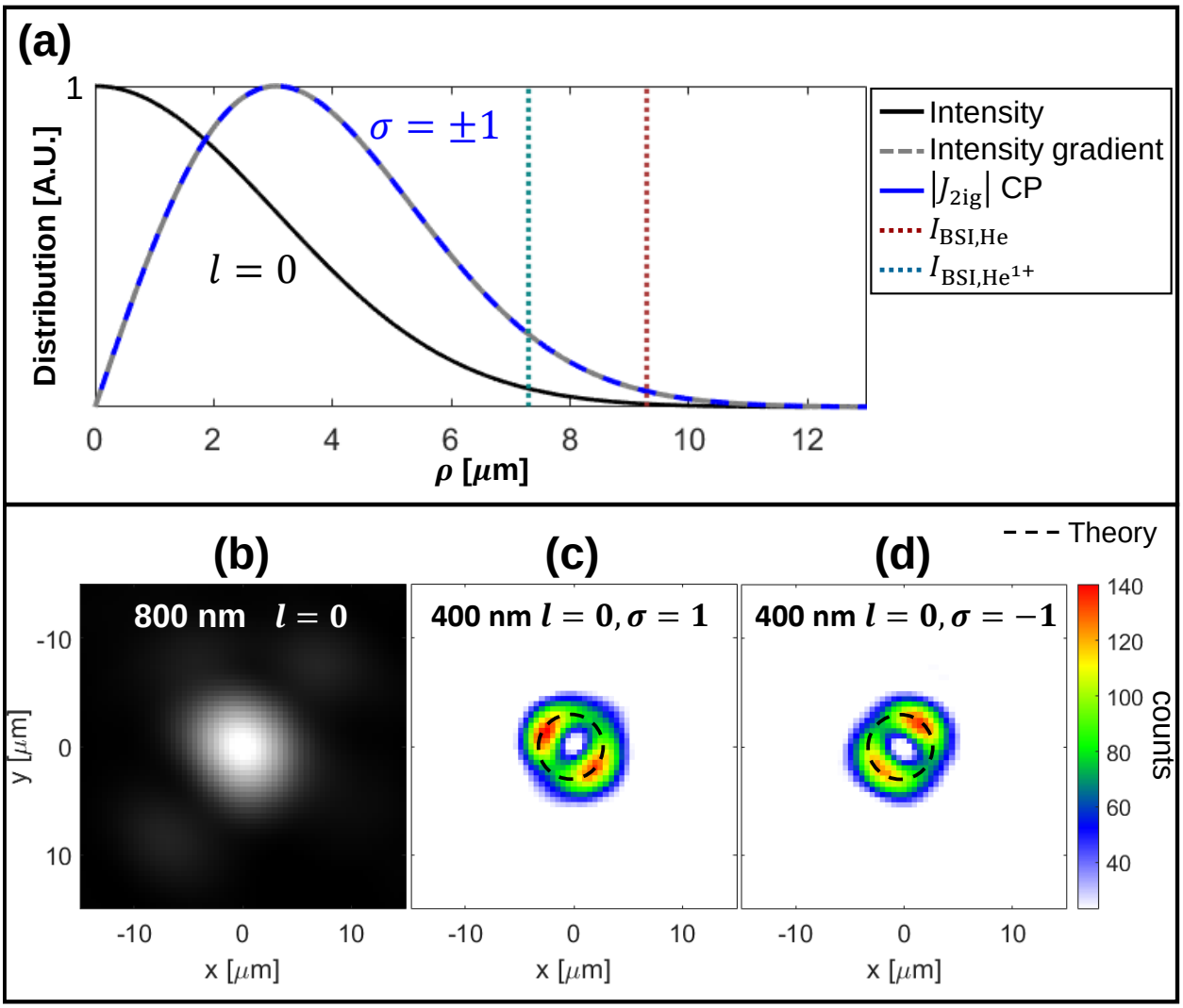

Figure 5.2: **Spatial 2ω current source and measured 2ω photon distributions from $l = 0$ LG beam:** (a) Normalized radial distributions of the pump beam intensity (black), intensity gradient (dashed gray), and intensity-gradient-induced 2ω current (blue) are calculated using laser pulses with a peak intensity of 1.5×10^{17} W/cm^2. The radial coordinates where the laser intensity reaches the barrier suppression ionization threshold are marked for He (dotted brown) and He^{1+} (dotted green) indicating the estimated position of the density gradients. (b) Measured 800 nm focal spot image was used to estimate the focal spot size $w_0 \sim 6$ μm and calibrate the scale in calculations. Measured 400-nm images from LCP and RCP are shown in (c) and (d) where the black dashed circles mark the estimated peak location deduced from the calculated radial distribution.

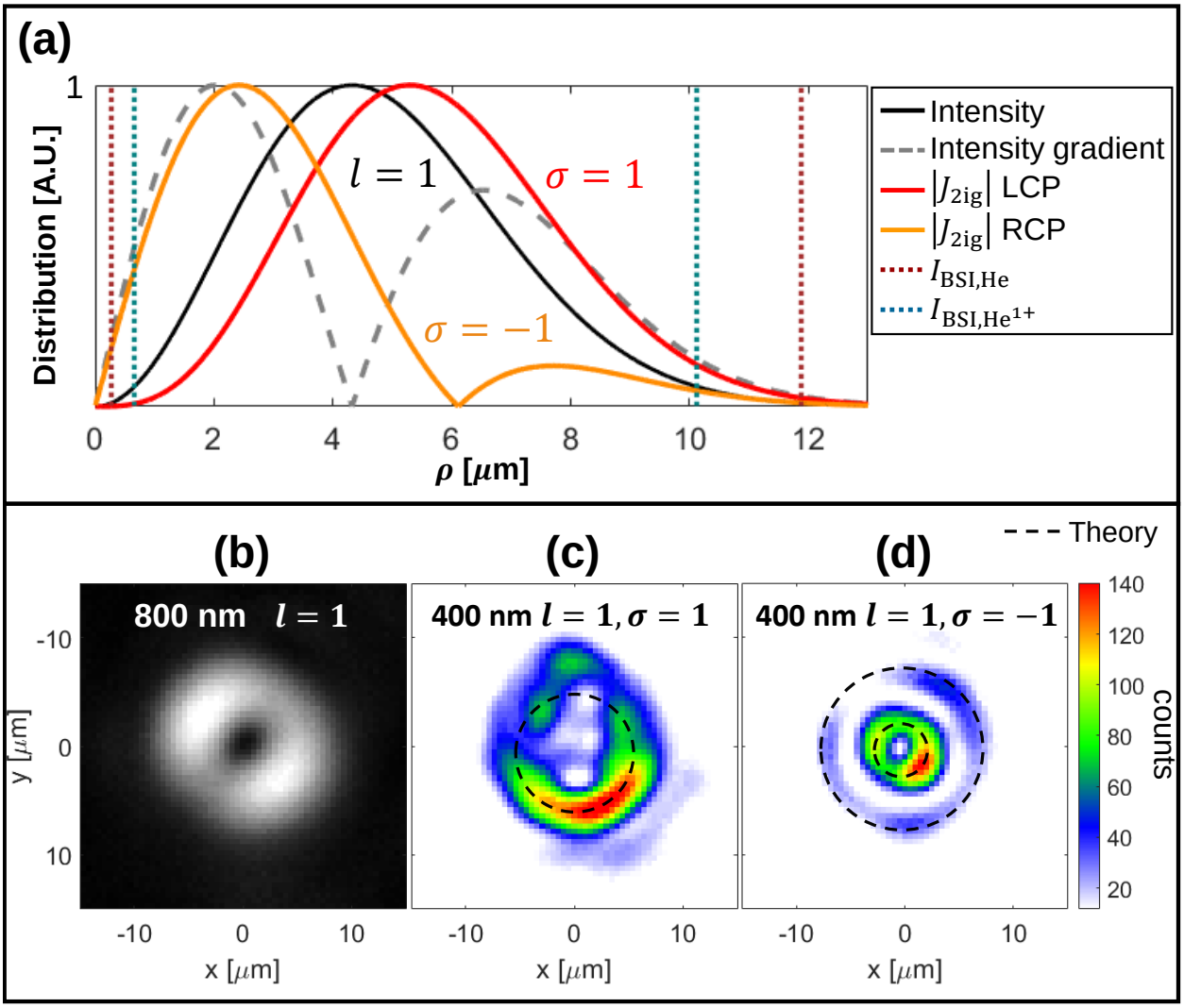

Figure 5.3: **Spatial 2ω current source and measured 2ω photon distributions from LG_0^1 beam:** (a) Normalized radial distributions of the pump beam intensity (black), intensity gradient (dashed gray), and intensity-gradient-induced 2ω current (red and orange) are calculated using CP laser pulses with a peak intensity of 1.5×10^{17} W/cm^2. BSI threshold intensities for He (dotted brown) and He^{1+} (dotted green) are reached on both sides of the peak intensity. (b) Measured 800 nm LG_0^1 mode. Measured 400-nm image from LCP laser is shown in (c) where the dashed circle corresponds to the peak of the red curve in (a). Measured 400-nm image from RCP laser is shown in (d) where two dashed circles correspond to the inner and outer peaks of the orange curve in (a).

that off-axis wave-front deformations are the main cause.

5.2.3 Far-field electric field and radiation patterns

The second harmonic current source can be approximated as an annulus which has the radial and azimuthal distribution given by Eq. (5.4) or (5.5) and a height on the order of the laser-plasma formation length, $L \sim 2z_{\mathrm{R}}$. The far-field radiation can be calculated by treating the current source as an antenna. Calculation is done with the two-step procedure [132] in the configuration that is described in Fig. 5.4. In the first step, the vector potential induced by second-harmonic current density is found from the integration

$$\mathbf{A}_2 = \iiint_V dV' \frac{\mathbf{J}_2(\rho', \phi', z')}{c} \frac{e^{ik|\mathbf{r}-\mathbf{r}'|}}{|\mathbf{r}-\mathbf{r}'|} \tag{5.6}$$

in far-field approximation. In the second step, the electric field $\mathbf{E}_2$ is calculated from the vector potential $\mathbf{A}_2$. The integration over the current density is done in cylindrical coordinates, but the components of the vector potential and the field are solved in spherical coordinates. The components of the vector potential are

$$A_r \approx 0,\ A_\theta = \frac{e^{ik_2 r}}{cr} N_\theta, \text{ and } A_\phi = \frac{e^{ik_2 r}}{cr} N_\phi \tag{5.7}$$

where

$$N_\theta = \iiint_V dV' \left[J_\rho \cos\theta \cos(\phi - \phi') + J_\phi \cos\theta \sin(\phi - \phi') - J_z \sin\theta \right] e^{-ik_2 r' \cos\psi}$$

$$N_\phi = \iiint_V dv' \left[-J_\rho \sin(\phi - \phi') + J_\phi \cos(\phi - \phi') \right] e^{-ik_2 r' \cos\psi}$$

and

$$r' \cos\psi = \rho' \sin\theta \cos(\phi - \phi') + z' \cos\theta \text{ and } dV' = \rho' d\rho' d\phi' dz'$$

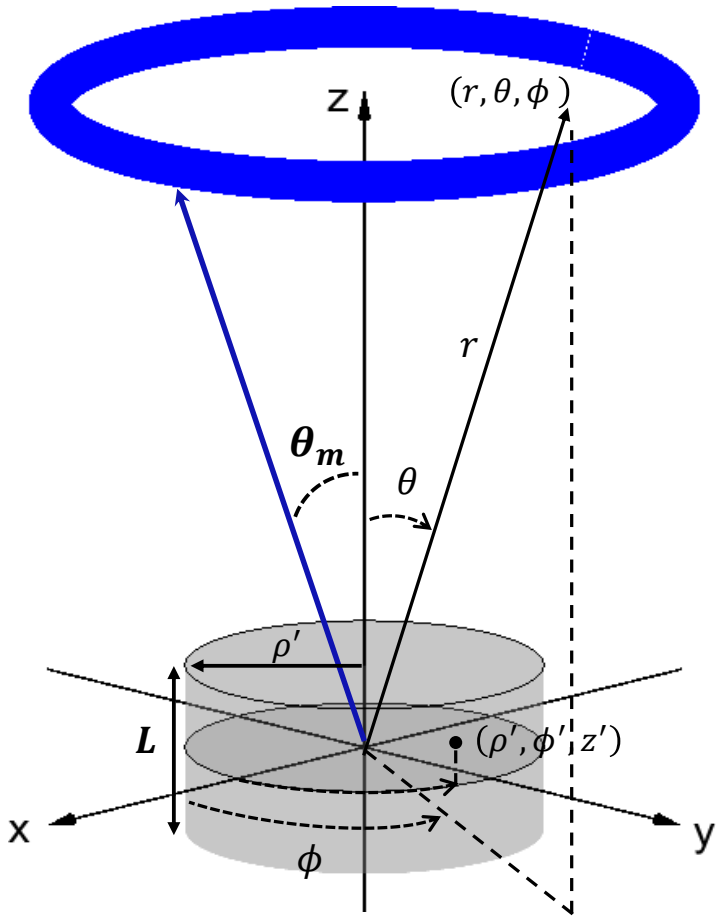

Figure 5.4: **Coordinate system for computing radiation field:** The shaded cylinder shows the geometry of the second harmonic current source. The blue ring shows the far-field radiation pattern with the maximum at the polar angle θ_{m}.

For the density gradient contribution, because of the steep density change induced by optical-field ionization, it is simpler to assume a region of density gradient as a delta function at $\rho = \rho_0$. Substitute $\partial n_0/\partial\rho = C_g\delta(\rho-\rho_0)$ into Eq. (5.4), where C_g is a constant. Substitute $\mathbf{J}_{2dg} = \left(J_{\rho,2dg}, J_{\phi,2dg}, 0\right)$ from Eq. (5.4) into (5.6). The integration over ρ' gives

$$\begin{aligned} N_\theta =& C_{dg,1}2^{|l|}\cos\theta e^{-i2\omega_0 t}\int_{-Z_R}^{Z_R} dz'\left[e^{i(2k_1-k_2\cos\theta)z'}\right]\times \\ & \int_0^{2\pi} d\phi'\left\{\left[-i\cos(\phi-\phi')\pm\sin(\phi-\phi')\right]e^{i2(l\pm1)\phi'}e^{-ik_2\rho_0\sin\theta\cos(\phi-\phi')}\right\} \end{aligned} \tag{5.8}$$

where $C_{dg,1} = C_j C_g E_0^2 \rho_0^{2|l|+1} e^{-2\rho_0^2}$ is a constant, k_1 and k_2 are the fundamental and the second-harmonic wave number in the plasma. The integral of z' leads to a sinc function that

$$\int_{-Z_R}^{Z_R} dz'\left[e^{i(2k_1-k_2\cos\theta)z'}\right] = 2z_R\mathrm{sinc}\left[(2k_1-k_2\cos\theta)z_R\right].$$

The integral of ϕ' in (5.8) can be rearranged as

$$\int_0^{2\pi} d\phi'\{\cdots\} = 2\pi i^{2l+1\pm1}e^{i2(l\pm1)\phi}B_{2l\pm1}(k_2\rho_0\sin\theta)$$

where $B_{2l\pm1}$ is the Bessel function of the first kind of order $2l\pm1$. In the last integral, the identity $-i\cos(\phi-\phi')\pm\sin(\phi-\phi') = -ie^{\pm(\phi-\phi')}$ and the Bessel's first integral

$$B_n(x) = \frac{i^{-n}}{2\pi}\int_0^{2\pi} d\phi' e^{in\phi}e^{ix\cos\phi}.$$

is used. Then by combining these components, we have

$$N_\theta = C_{dg,2}i^{2l+1\pm1}2^{|l|}\cos\theta\mathrm{sinc}\left[(2k_1-k_2\cos\theta)z_R\right]B_{2l\pm1}(k_2\rho_0\sin\theta)e^{i[-2\omega_0 t+2(l\pm1)\phi]} \tag{5.9}$$

where $C_{dg,2} = 4\pi z_R C_{dg,1}$ and $A_\theta = \dfrac{e^{ik_2 r}}{cr}N_\theta$ is readily achieved. The azimuthal components N_ϕ and A_ϕ are obtained by the same procedure. Therefore, the vector potential induce by the density gradient contribution can be expressed as

$$\mathbf{A}_{2\mathrm{dg}} = \left(i\cos\theta\hat{\boldsymbol{\theta}} \mp \hat{\boldsymbol{\phi}}\right)\frac{C_{dg,2}i^{2l\pm1}2^{|l|}}{cr}\mathrm{sinc}\left[\left(2k_1 - k_2\cos\theta\right)z_\mathrm{R}\right]B_{2l\pm1}\left(k_2\rho_0\sin\theta\right)e^{i[k_2 r - 2\omega_0 t + 2(l\pm1)\phi]}. \tag{5.10}$$

In the small θ limit ($\cos\theta \approx 1$, $r \to z$), the corresponding second harmonic electric field can be transformed into the Cartesian coordinate, i.e. $i\cos\theta\hat{\boldsymbol{\theta}} \mp \hat{\boldsymbol{\phi}} \to i\hat{\boldsymbol{\rho}} \mp \hat{\boldsymbol{\phi}} \to (i\hat{\mathbf{x}} \mp \hat{\mathbf{y}})\,e^{\mp i\phi}$, and

$$\mathbf{E}_{2\mathrm{dg}} = i\left(\hat{\mathbf{x}} \pm i\hat{\mathbf{y}}\right)\frac{C_{\mathrm{dg},l}}{z}\mathrm{sinc}\left[\left(2k_1 - k_2\cos\theta\right)z_\mathrm{R}\right]B_{2l\pm1}\left(k_2\rho_0\sin\theta\right)e^{i[k_2 z - 2\omega_0 t + (2l\pm1)\phi]} \tag{5.11}$$

where $C_{\mathrm{dg},l} = \frac{i^{2l\pm1}8\pi C_\mathrm{j}C_\mathrm{g}z_\mathrm{R}e^3\rho_0\left[E_0^l(\rho_0)\right]^2}{m^2c^2\omega_0^2}$ depends on the value of l and and upper (lower) sign corresponds to LCP (RCP).

For the intensity gradient contribution, far-field electric field can be obtained in the similar manner but the integration over ρ' goes from 0 to ∞ in this case. Substitute $\mathbf{J}_{2\mathrm{ig}} = \left(J_{\rho,2\mathrm{ig}}, J_{\phi,\mathrm{idg}}, 0\right)$ from Eq. (5.5) into (5.6) and use Eq. (5.9) so that for the intensity gradient contribution

$$\begin{aligned} N_\theta =& C_{\mathrm{ig}}i^{2l+1\pm1}2^{|l|}\cos\theta\mathrm{sinc}\left[\left(2k_1 - k_2\cos\theta\right)z_\mathrm{R}\right]e^{i[-2\omega_0 t + 2(l\pm1)\phi]}\times \\ &\int_0^\infty d\rho'\left\{\left[\left(|l| \mp l\right)\left(\frac{\rho'}{w_0}\right)^{-1} - 2\left(\frac{\rho'}{w_0}\right)\right]\left(\frac{\rho'}{w_0}\right)^{2|l|+1}e^{-2(\rho'/w_0)^2}B_{2l\pm1}\left(k_2\sin\theta\rho'\right)\right\} \end{aligned} \tag{5.12}$$

where $C_{\mathrm{ig}} = 4\pi C_\mathrm{j}z_\mathrm{R}n_0E_0^2$ is a constant. The integral of ρ' can be done analytically using a Bessel function integral identity involving the Whittakar function

$$\int_0^\infty x^\mu e^{-\alpha x^2}B_\nu\left(\beta x\right)dx = \frac{\Gamma\left(\frac{1}{2}\mu + \frac{1}{2}\nu + \frac{1}{2}\right)}{\beta\alpha^{\mu/2}\Gamma\left(\nu+1\right)}\exp\left(-\frac{\beta^2}{8\alpha}\right)M_{\frac{\mu}{2},\frac{\nu}{2}}\left(-\frac{\beta^2}{4\alpha}\right)$$

where α, β, μ, and ν are the parameters of this integral identity, Γ represents the Gamma function, and M represents the Whittaker function. Substitute $\alpha = 2$, $\beta = k_2\sin\theta$, $\mu = 2|l|$ or $2|l|+2$, and $\nu = 2l \pm 1$ into the Eq. (5.12), we have

$$N_\theta = C_{\mathrm{ig}}i^{2l+1\pm1}\cos\theta\mathrm{sinc}\left[\left(2k_1 - k_2\cos\theta\right)z_\mathrm{R}\right]e^{i[-2\omega_0 t + 2(l\pm1)\phi]}\Psi_{l,\pm1}\left(\theta\right) \tag{5.13}$$

where

$$\Psi_{l,\pm1}(\theta) = \frac{\exp\left(-\frac{k_2^2 w_0^2 \sin^2\theta}{16}\right)}{k_2 w_0 \sin\theta \Gamma(2l+1\pm1)} \times \left[(|l| \mp l)\,\Gamma\left(|l|+l+\frac{1}{2}\pm\frac{1}{2}\right) M_{|l|,l\pm\frac{1}{2}}\left(-\frac{k_2^2 w_0^2 \sin^2\theta}{8}\right) - \Gamma\left(|l|+l+\frac{3}{2}\pm\frac{1}{2}\right) M_{|l|+1,l\pm\frac{1}{2}}\left(-\frac{k_2^2 w_0^2 \sin^2\theta}{8}\right)\right].$$

The vector potential can be obtained using the same formalism as

$$\mathbf{A}_{2ig} = \left(i\cos\theta\hat{\boldsymbol{\theta}} \mp \hat{\boldsymbol{\phi}}\right) \frac{C_{\mathrm{ig}} i^{2l\pm1} 2^{|l|}}{cr} \mathrm{sinc}\left[(2k_1 - k_2\cos\theta) z_{\mathrm{R}}\right] \Psi_{l,\pm1}(\theta)\, e^{i[k_2 r - 2\omega_0 t + 2(l\pm1)\phi]} \tag{5.14}$$

and in the far field and small θ limit, the electric field in the Cartesian coordinate is

$$\mathbf{E}_{2\mathrm{dg}} = i(\hat{\mathbf{x}} \pm i\hat{\mathbf{y}}) \frac{C_{\mathrm{ig},l}}{z} \mathrm{sinc}\left[(2k_1 - k_2\cos\theta) z_{\mathrm{R}}\right] \Psi_{l,\pm1}(\theta)\, e^{i[k_2 z - 2\omega_0 t + (2l\pm1)\phi]} \tag{5.15}$$

where $C_{\mathrm{ig},l} = \frac{i^{2l\pm1} 8\pi z_{\mathrm{R}} e^3 n_0 E_0^2 w_0^2}{m^2 c^2 \omega_0^2}$ depends on the value of l, and upper (lower) sign corresponds to LCP (RCP).

Both the Bessel function $B_{2l\pm1}(k_2\rho_0\sin\theta)$ in Eq. (5.11) and the function $\Psi_{l,\pm1}(\theta)$ in Eq. (5.15) have characteristics of multiple ring pattern in the far-field, but the distribution is confined by the sinc function $\mathrm{sinc}\left[(2k_1 - k_2\cos\theta) z_{\mathrm{R}}\right]$. Therefore, the far-field intensity maximizes at an emission angle (measured from the incident direction) determined by

$$2k_1 - k_2\cos\theta = 0 \tag{5.16}$$

and the angle has value of

$$\theta_{\mathrm{m}} = \cos^{-1}\left(\frac{2k_1}{k_2}\right) = \cos^{-1}\sqrt{\frac{1-\omega_p^2/\omega_0^2}{1-\omega_p^2/4\omega_0^2}}. \tag{5.17}$$

Eq. (5.16) can be regarded as the phase matching condition and θ_{m} is the phase matching angle. Note that for $z \neq 0$, the Gouy phase term may need to be included and results in a

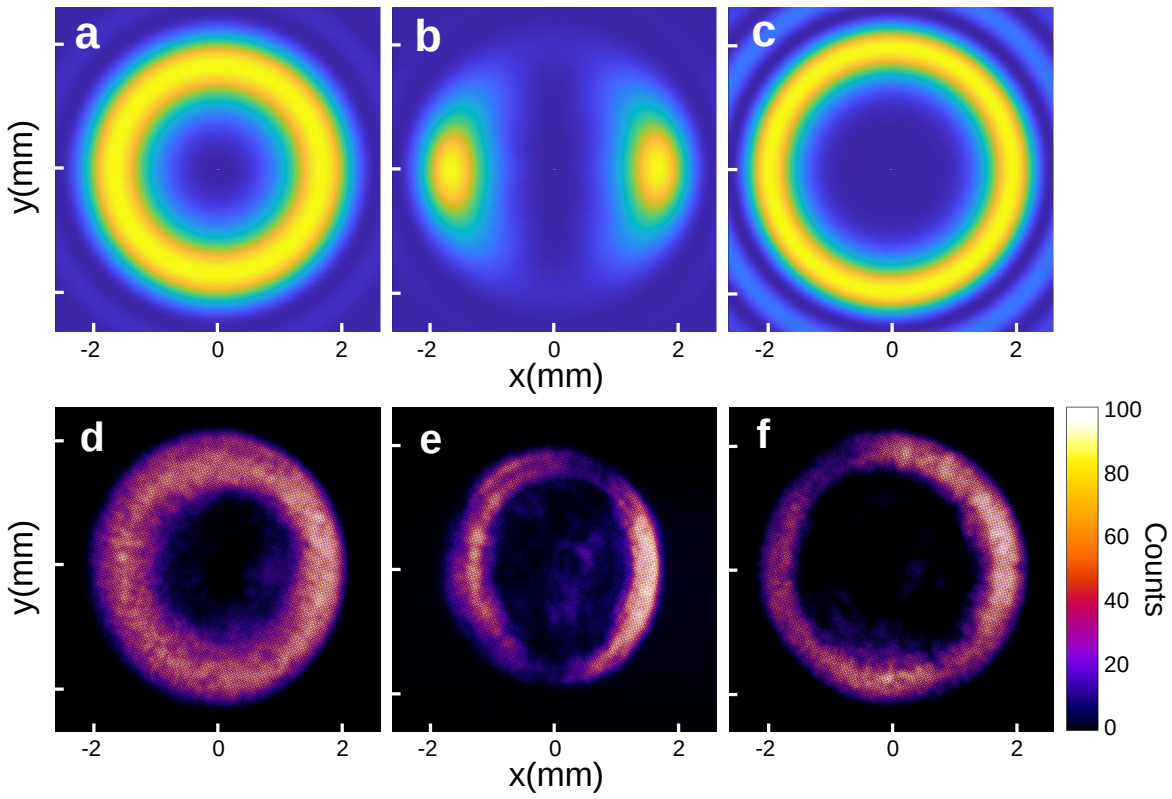

Figure 5.5: **Far-field radiation patterns.** The calculated (top row, a-c) and the measured (bottom row, d-f) far-field transverse intensity profiles of the 2ω radiation from (a, d) left-handed circularly polarized beam with l = 0, (b, e) linearly polarized LG beams with l = +1, and (c, f) left-handed circularly polarized LG beams with l = +1.

limitation to the coherence length of the SHG process especially for large $|l|$ values. Far-field radiation patterns calculated using Eq. (5.15) are shown in Fig. 5.5(a)-(c) for the cases of CP Gaussian ($\sigma = \pm 1, l = 0$), LP Laguerre-Gaussian ($\sigma = 0, l = \pm 1$), and CP Laguerre-Gaussian ($\sigma = \pm 1, l = \pm 1$). Measured patterns are shown in the same figure (d)-(f). Fig. 5.5(d) shows the expected 2ω annular intensity pattern using a LCP, Gaussian beam; Fig. 5.5(e) shows how this pattern changes when a LP, $l = 1$ beam is used instead and Fig. 5.5(f) shows the intensity pattern obtained when a CP LG_0^1 mode is used. The agreement is good, especially for CP cases.

5.3 Conversion rules of optical angular momentum

The angular momentum properties of the output second harmonic beam are inspected by extracting the relevant (polarization and azimuthal phase) terms from of the Eq. (5.11) and (5.15). For both density gradient and intensity gradient contribution, the same form is yielded for a fundamental beam with SAM value $\sigma = \pm 1$ and OAM value l as

$$\mathbf{E}_2 \propto (\hat{\mathbf{x}} \pm i\hat{\mathbf{y}}) \exp\left[i\left(2l \pm 1\right)\phi\right]. \tag{5.18}$$

where the upper and lower sign correspond to LCP ($\sigma = +1$) and RCP ($\sigma = -1$). By comparing the input and output beams, several conservation rules of optical angular momentum can be deduced. First, the polarization state is the same for small θ_{m}. In other words, the spin angular momentum is preserved in the second-harmonic generation process, that is

$$s_{2\omega} = s_{\omega} = \sigma \tag{5.19}$$

where s_{ω} and $s_{2\omega}$ represent the SAM values of the fundamental and the 2ω beams respectively. Second, the azimuthal phase factor of the 2ω beam becomes $2l \pm \sigma$. This relation gives

$$l_{2\omega} = 2l_{\omega} + s_{\omega} \tag{5.20}$$

where l_{ω} and $l_{2\omega}$ are the azimuthal mode indexes of the fundamental and the 2ω beam respectively. Using Eq. (5.19) and (5.20), rule for the conservation of the total angular momentum can be immediately obtained as

$$j_{2\omega} = 2j_{\omega} \tag{5.21}$$

where $j_n = l_n + s_n$ for respective harmonics n. Eq. (5.19)-(5.21) describe the conservation rules of spin, orbital, and total optical angular momentum in the second harmonic generation respectively.

Table 5.1 shows the combinations of angular momentum components of the fundamental and 2ω beams based on the conservation rules given by Eqns. (5.19), (5.20), and (5.21). For input beams with SAM values $(-1, 0, 1)$ and OAM values $(-1, 0, 1)$, these conservation rules give 5 combinations for the total, SAM and OAM of the 2ω photons as shown in Table 5.1. Case A simply describes the situation where no optical angular momentum is involved. This is just a LP, Gaussian mode. Case B demonstrates simplest case that involves the conversion of spin-to-orbital angular momentum- a circularly polarized Gaussian pump beam. Case C shows the complete transfer of OAM from the fundamental to the 2ω photons for a linearly polarized but $l = \pm 1$ pump beam. Cases D and E show the coupling of SAM and OAM in the second harmonic generation process. The SAM and OAM add up to either increase (case D) or decrease (case E) the orbital angular momentum.

When the plasma density is high, the small θ_m approximation may not be valid. Deduced from Eq. (5.10) and (5.14) with the substitution of the phase matching condition, the exact form of the angular momentum relevant terms in the electric field can be written as

$$\mathbf{E}_2 \propto \left(i\cos\theta_{\mathrm{m}}\hat{\boldsymbol{\theta}} \mp \hat{\boldsymbol{\phi}}\right) e^{i(2l\pm 2)\phi} = \left[\cos\theta_{\mathrm{m}}\left(i\hat{\boldsymbol{\theta}} \mp \hat{\boldsymbol{\phi}}\right) \pm (1-\cos\theta_{\mathrm{m}})\,\hat{\boldsymbol{\phi}}\right] e^{i(2l\pm 2)\phi} \tag{5.22}$$

Case	Fundamental (800 nm)			SHG (400 nm)		
	j_ω	s_ω	l_ω	$j_{2\omega}$	$s_{2\omega}$	$l_{2\omega}$
A	0	0	0	0	0	0
B	±1	±1	0	±2	±1	±1
C	±1	0	±1	±2	0	±2
D	±2	±1	±1	±4	±1	±3
E	0	∓1	±1	0	∓1	±1

Table 5.1: **Angular momentum conversion:** Combinations of angular momentum components of the fundamental and 2ω beams, for the input fundamental or pump beams with linear or circular polarization ($\sigma = 0, \pm 1$) and the azimuthal index $l = 0, \pm 1$. The last column shows the expected l of the output 2ω beam.

where the form is separated into two parts. The first part becomes circularly polarized when the beam is collimated, but the second part remains azimuthally polarized. The ratio of deviation from circular polarization is about $(1 - \cos\theta_\mathrm{m})^2$ which is generally a very small value (on the order of 10^{-7} for a plasma density of 6×10^{17} cm^{-3}) but the portion increases rapidly as θ_m increases. The azimuthally polarized component has the same spiral phase $e^{i(2l\pm1)\phi}$ (since $\hat{\boldsymbol{\phi}} e^{i\phi}$ represents a plane wave) as the circularly polarized component, and therefore the same OAM value is expected.

5.4 Measurement of the helical phase front of 2ω light

The conversion of optical angular momentum has been tested by characterizing the helical phase of the second harmonic radiation. By using various combinations of QWP and SPP we can control the SAM and OAM respectively, thereby generating the fundamental or pump beam that has a known polarization and azimuthal mode index. Two methods were used to measure the helical phase of the 2ω beams. First, the relative phase front from two beams with opposite helicities were compared in a wavefront sensor (WFS). WFS method has some issues when the spiral phase is being extracted from the beam directly, so it has

to be inferred from a relative measurement. Second, the azimuthal phase of a beam was measured by interferometry. The azimuthal mode can be determined in single shot but this method unlike the WFS method is not able to give the phase distribution of the whole beam. We show the expected values of the azimuthal index of the second harmonic light generated by the plasma for each setting shown in Table 5.1.

5.4.1 Wave-front sensor measurement

The emerging second-harmonic radiation was measured using the commercial wavefront sensor (PHASICS SID4 HR) using the setup shown in the inset of Fig. 5.1. The divergent 2ω light was collimated and sent to the WFS directly. Shack-Hartmann wavefront sensors have been shown to be useful in reconstruction of the helical phase of high-harmonic generation with optical vortices [131, 130] despite difficulties related to phase dislocation inherent in optical vortices. Numerical methods are often required to avoid the discontinuities in the phase front [131, 133]. Direct phase measurement could be possibly done by analyzing local Poynting vector [134]. However, this is not easy to do using a commercial wave front sensor whose output is processed using its own algorithm.

In this work, relative measurement is used to compared two beams with similar intensity profiles but with helical phase rotating in different directions (opposite helicities). One reason for using a relative measurement is that the lack of detailed information as a commercial WFS is used. Another main reason is to exclude the defocus and spherical aberration of the 2ω beam, which is constantly larger than 2π rad. The spiral phase information is present together with additional phase information that is sensitive to azimuthal index and laser intensity distribution. Since two beams with the same $|l|$ value have similar beam profiles, the subtraction of two images can mitigate the additional phase information. The WFS captures the far-field radiation intensity patterns (three examples are shown in Fig. 5.5(d)-(f)) as well as the spatial phase information. The helical phase structure is obtained from these recordings in the following way. For each case, an annular numerical mask matching the beam profile was applied and analyzed in Phasics software using a plane wave reference.

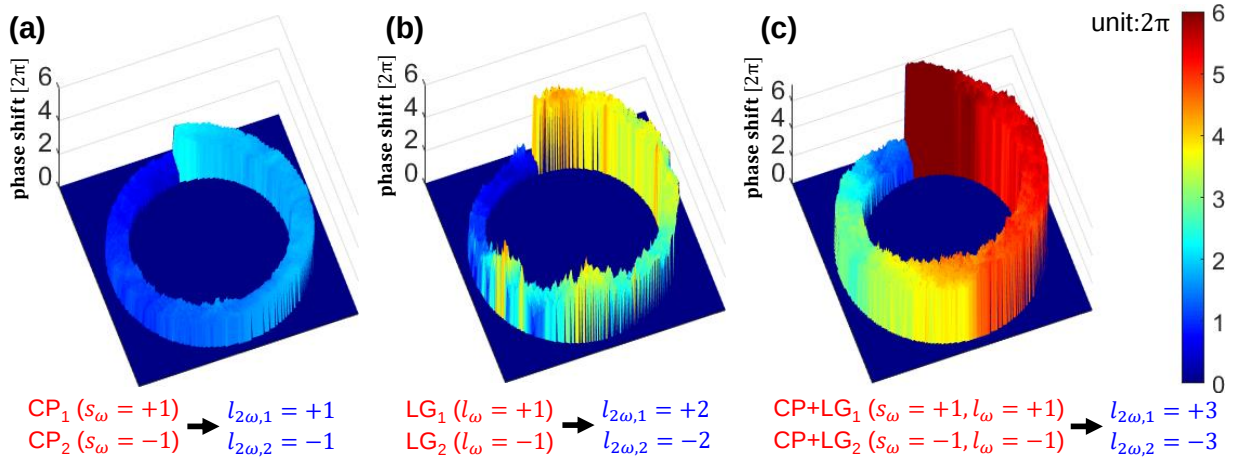

Figure 5.6: **Spiral phase measured by the wave-front sensor:** Relative helical phase distributions between two shots from (a) LCP and RCP beams ($CP_1 - CP_2$), (b) linearly polarized LG beams with opposite helicities ($LG_1 - LG_2$), (c) circularly polarized LG beams with opposite helicities (CP+LG_1-CP+LG_2).

The outcomes (phase distribution between the signal 2ω beam and a plane wave reference) from beams with opposite helicities were then subtracted to reconstruct a relative phase distribution. The procedure leads to azimuthally increasing relative phase distributions as shown in Fig. 5.6. The magnitude of the total phase change is $2\pi\,(l_1 - l_2)$ radians if two beams have azimuthal indexes of l_1 and l_2. Since in this case we compare two cases of beams with opposite helicities, $l_2 = -l_1$, we expect twice the phase shift, which leads to a total phase shift of $4\pi\,|l_{2\omega}|$ radians.

Figure 5.6(a) shows the azimuthal phase obtained when a circularly polarized fundamental LG beam was used. This is Case B in Table 5.1. Although the pump beam has no OAM we expect the 2ω beam to have $l_{2\omega} = \pm 1$ and a total azimuthal phase of 4π radians as seen in Fig. 5.6(a). Fig. 5.6(b) shows the phase shift distribution when the 2ω photons from LP LG beams with $l_\omega = \pm 1$ are measured. The expected magnitude of total relative phase shift (Case C in Table 5.1) is now 8π radians if there were twice the amount of OAM in the 2ω beam ($l_{2\omega} = \pm 2$) indicating OAM was completely transferred from the fundamental to the second harmonic. Now we discuss what happens when the SPP was used in tandem with

the QWP (for both case D and E in Table 5.1). The intensity profile is given by Fig. 5.5(f) in this case. In Fig. 5.6(c), OAM and SAM values of the input beams were set according to case D. A total relative phase shift of 12π radians is expected and observed since the 2ω output beam possesses $l_{2\omega} = \pm 3$. Even though this method only demonstrated a relative helical phase shift, the total phase shift implies the amount OAM carried by the output beams are as predicted in Table 5.1.

5.4.2 Young's double slit interferometry measurement

A second technique was used to confirm the results of the helical phase measurement obtained using the WFS. In this set-up the collimated second harmonic light was sent through a Young's double-slit interferometer for a direct measurement of the azimuthal mode index of the beams (Fig. 5.7). The beam passed through the center of a custom-made double-slit target and generated an interference pattern. A double slit mask with a slit width of 30 μm and a separation of 2.8 mm was used to retrieve the difference in the spatial phase from a range of azimuthal coordinates intercepted by the slits. A screen was placed about 1 m behind the mask. Contrary to the typical straight fringe pattern obtained when a plane wave traverses the two slits in Young's double slit experiment, a beam with a helical wavefront yields a kinked fringe pattern bent in a direction according to its helicity [135, 136].

The modulated fringe patterns are given by

$$I(y,z) = I_0 \cos^2\left(\frac{\pi x a}{\lambda D} + \frac{\Delta\Phi(y)}{2}\right) \tag{5.23}$$

where I_0 is the normalized peak intensity, a is the distance between two slits, λ is the wavelength of light, D is the distance between the slits and the screen, and $\Delta\Phi(y)$ is the phase difference between two slits along the vertical direction y. The vertical phase shift term $\Delta\Phi(y)$ is proportional to azimuthal index of the input light but modulated by a. It could be difficult to precisely determine arbitrary azimuthal index due to the inhomogeneous light intensity distribution [136]. However, one can estimate this value using $I(y,z)$ and mitigate

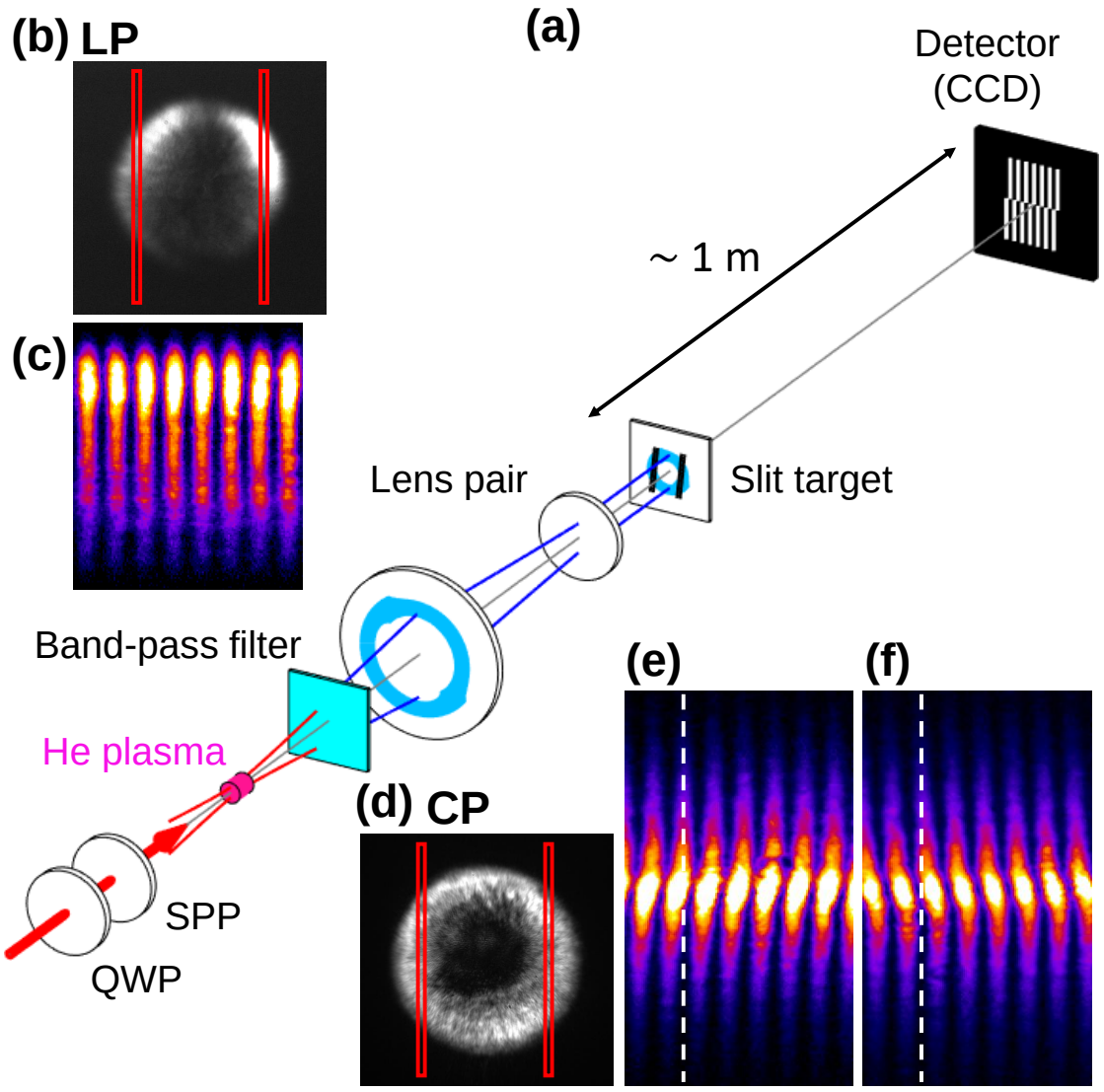

Figure 5.7: **Double-slit interferometry:** (a) Schematic setup of the interferometer. (b) 2ω radiation pattern from a LP beam and (c) the corresponding fringe pattern. (d) 2ω radiation pattern from a CP beam. (e) and (f) show the fringe patterns for LCP and RCP cases.The red rectangles in (b) and (d) indicate the approximate position of the slits. The white dashed line in (e) and (f) shows the relative bending of the fringes.

Case	Figure	Fundamental	Shift (avg)	Shift (std)	Estimated $l_{2\omega}$
A	Fig. 5.7(c)	$l_\omega = 0,\ s_\omega = 0$	0.047	0.017	0.08 ± 0.03
B	Fig. 5.8(a)	$l_\omega = 0,\ s_\omega = -1$	−0.59	0.022	-1.00 ± 0.04
C	Fig. 5.8(a)	$l_\omega = +1,\ s_\omega = 0$	1.094	0.043	1.85 ± 0.07
D	Fig. 5.8(a)	$l_\omega = +1,\ s_\omega = +1$	1.835	0.025	3.11 ± 0.04
E	Fig. 5.8(a)	$l_\omega = +1,\ s_\omega = -1$	0.608	0.026	1.03 ± 0.04

Table 5.2: **Measured OAM values from the interferometry.** The amount of the shift from the top to the bottom of the interference fringes from the 2ω radiation for different cases in Table 5.1 as well as in Fig. 5.7 and 5.8. In the fifth column, the azimuthal value $l_{2\omega}$ of the output beams are estimated.

the effect of inhomogeneity by using average amount of shift in the estimation. This double-slit interferometer setup was calibrated using the fringe patterns generated by 800-nm beams that carried different amounts of OAM. (Details of the calibration are demonstrated in the Appendix C.) The fringes in the top and bottom zone are found shifted by about $0.59 l_\mathrm{v} D_\mathrm{f}$, where l_v is the azimuthal index of the vortex beam and D_f is the distance between neighboring fringes.

Fig. 5.7 also shows the radiation and fringe patterns from 2ω beams without OAM and with opposite OAM values. For a linear polarized Gaussian beam (case A), its radiation pattern has two lobes along the polarization direction (Fig. 5.7(b)) and its interference pattern yields straight line fringes (Fig. 5.7(c)) showing that the output 2ω beam carries no OAM. For a circularly polarized Gaussian beam (case B, $s_\omega = \pm 1$), annular emission pattern (Fig. 5.7(d)) appears. Fig. 5.7(e) and 5.7(f) are results of double slit experiments from the LCP and RCP cases respectively. The fringe patterns for two cases now have kinks (bends) in opposite direction with nearly equal amount of shift.

Single-shot measurements of the interference pattern using different polarizations and spatial modes of the 2ω beams are shown in Fig. 5.8(a) for the cases B, C, D, and E listed in Table 5.1. For different cases, different magnitudes of shift of the fringes were observed. Fig.

5.8(b) shows a series of calculated fringe patterns (synthetic interferograms) by using the slit width and the slit-screen distance in the experiment and assuming a homogeneous input light with different index l. The exact value of OAM carried by the beam can be evaluated measuring the shift for a fringe from the top to bottom and by comparing the experimental interference pattern with the synthetic pattern. Contrary to the calculated results, the actual patterns have inhomogeneous intensity distributions due to the local variations of intensity on the slits.

The average amount of the shift and the standard deviation are calculated for the fringe patterns in Fig. 5.7 or 5.8. The results are shown in the Table 5.2, where each row cor-

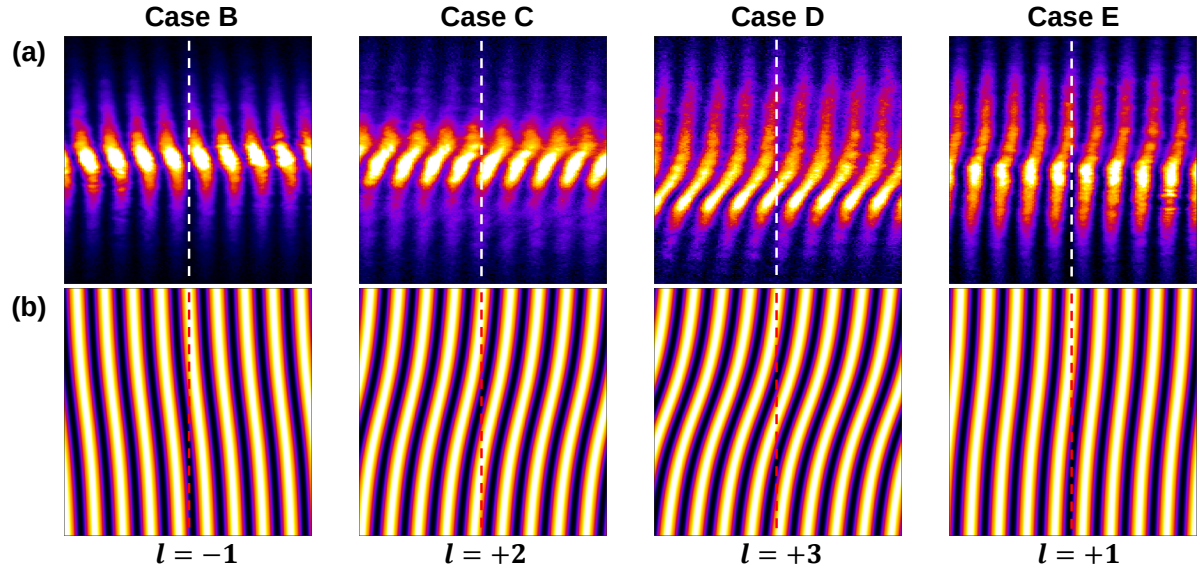

Figure 5.8: **Interference patterns from spiral phase fronts.** (a) Observed and (b) calculated interference fringe patterns for different cases in Table 5.1. The input beam parameters from left to right: Case B ($s = -1, l = 0$), Case C ($s = 0, l = +1$), Case D ($s = +1, l = +1$), Case E ($s = -1, l = +1$), where s and l are the spin and orbital angular momentum value of the fundamental beams. The white and red dash lines in (a) and (b) overlap with one of the bright fringes at the top for each case B-E for measuring the phase shift. The experimental patterns shown were selected from sets of 10 consecutive shots (shown in Appendix C).

responds to a case measured in experiments. For cases shown in Fig. 5.8, the estimated values of $l_{2\omega}$ are $-1.00 \pm 0.04\,(-1)$, $1.85 \pm 0.07\,(+2)$, $3.11 \pm 0.04\,(+3)$, and $1.03 \pm 0.04\,(+1)$ where the predicted values are shown in parentheses. Similar magnitudes of shift between the experimental and calculated fringes are also demonstrated by the white and red dashed lines in Fig. 5.8(a) and 5.8(b). These results are strong indications that the conservation law for OAM given by Eq. (5.20) is obeyed.

5.5 Measurement of polarization of 2ω light

The polarization states of the fundamental and 2ω light were both measured using a polarimeter based on the Mueller matrix formalism [137]. In this method, the polarization state of a beam is described by a four-vector (the Stokes vector) and a polarization element is described by a 4×4 matrix (the Mueller matrix). The changing of polarization state in polarization elements is then demonstrated by matrix calculations. Compare with another well-known matrix formalism method, the Jones calculus, Mueller's formalism has advantages that it is easier to be implemented by measuring the intensity and it can be applied to unpolarized or partially polarized beam.

The polarization state of a partially polarized beam is expressed by a Stokes vector $\mathbf{S}$ as

$$\mathbf{S} = \begin{bmatrix} S_0 \\ S_1 \\ S_2 \\ S_3 \end{bmatrix} = I_0\,(1-P) \begin{bmatrix} 1 \\ 0 \\ 0 \\ 0 \end{bmatrix} + I_0 P \begin{bmatrix} 1 \\ S_\alpha \\ S_\beta \\ S_\gamma \end{bmatrix} \tag{5.24}$$

where S_0, S_1, S_2, and S_3 are the Stokes parameters associated with the total intensity, the component of horizontal linear polarization, the component of linear polarization at 45° to the horizontal axis, and the component of circular polarization (±1 for left-handed/right-handed), I_0 is the intensity of the beam, and P is the degree of polarization (the ratio of polarized light and total intensity) where $P = \sqrt{S_1^2 + S_2^2 + S_3^2}/S_0$. S_α, S_β, and S_γ are the

normalized Stokes parameters for the polarized component of the beam and the relation $S_\alpha^2 + S_\beta^2 + S_\gamma^2 = 1$ should be fulfilled.

The ellipticity of the polarization of a beam is defined as the ratio of the major and minor axes of the polarization ellipse which is the locus of the electric vector at a fixed point in space. A circularly polarized beam has an ellipticity of ±1 and a linearly polarized beam has an ellipticity of 0. By definition, the SAM value equals to the ellipticity, i.e. $s = \sigma$. The ellipticity of the polarization entirely depends on the value of the parameter S_γ with the relation

$$\sigma = s = \frac{S_\gamma}{\sqrt{1 - S_\gamma^2} + 1} \tag{5.25}$$

Equation 5.25 shows the transformation between the third Stokes parameter and the ellipticity (the SAM value) is nonlinear. A small change in S_γ can lead to a large change in σ when $|S_\gamma| \sim 1$. For examples, $\sigma = \pm 1$ when S_γ equals to ±1; $\sigma = \pm 0.72$ when S_γ equals to ±0.95.

The Stoke parameter S_γ is measured by the setup shown in Fig. 5.9. The incident beam first passes through a quarter-wave plate whose fast axis is set at 45° to the horizontal plane. Then the beam passes through a linear polarizer whose transmission axis is at a variable angle ϑ and becomes linearly polarized. Finally, the output beam is measured by a CCD camera. The Mueller matrix for this setup is written as

$$\mathbb{M} = \frac{1}{2}\begin{bmatrix} 1 & 0 & \sin 2\vartheta & -\cos 2\vartheta \\ \cos 2\vartheta & 0 & \sin 2\vartheta \cos 2\vartheta & -\cos^2 2\vartheta \\ \sin 2\vartheta & 0 & \sin^2 2\vartheta & -\sin 2\vartheta \cos 2\vartheta \\ 0 & 0 & 0 & 0 \end{bmatrix} \tag{5.26}$$

where ϑ is the rotate angle of the linear horizontal polarizer.

The Stokes vector of the beam at the detector for this setup is calculated by $\mathbf{S}' = \mathbb{M}\mathbf{S}$ and

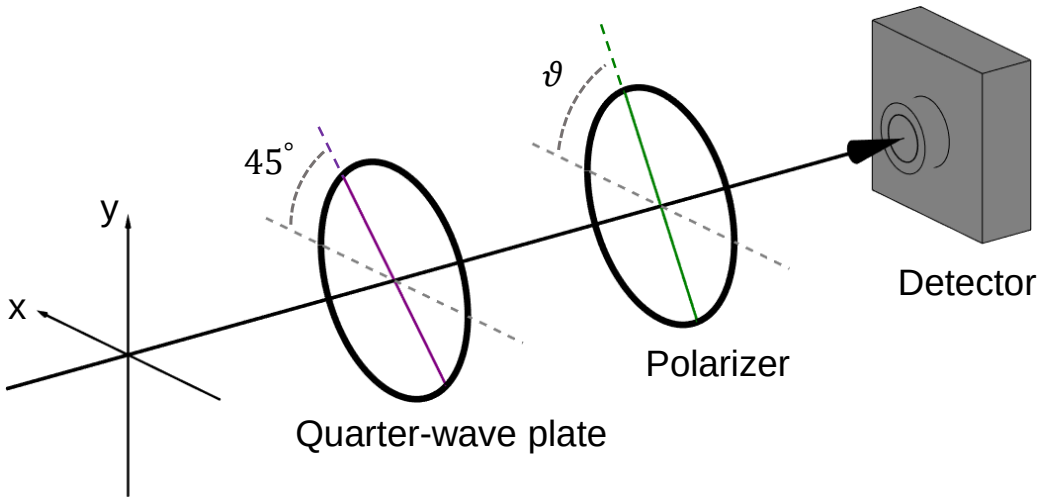

Figure 5.9: **Setup of the polarimeter:** The collimated beams were sent through a quarter-wave plate at 45° to the horizonal plane, a linear polarizer at a various angle ϑ, and a detector (CCD). The additional band-pass filter (not shown) is required for measuring 2ω light.

$$\mathbf{S}' = \frac{I_0\,(1-P)}{2}\begin{bmatrix} 1 \\ \cos 2\vartheta \\ \sin 2\vartheta \\ 0 \end{bmatrix} + \frac{I_0 P}{2}\begin{bmatrix} 1 + S_\beta \sin 2\vartheta - S_\gamma \cos 2\vartheta \\ \cos 2\vartheta + S_\beta \sin 2\vartheta \cos 2\vartheta - S_\gamma \cos^2 2\vartheta \\ \sin 2\vartheta + S_\beta \sin^2 2\vartheta - S_\gamma \sin 2\vartheta \cos 2\vartheta \\ 0 \end{bmatrix} \tag{5.27}$$

The first element of $\mathbf{S}'$ in (5.27) represents the total intensity measured by the detector of the polarimeter and it can be written as

$$S_0'(\vartheta) = \frac{I_0}{2}\left[1 + P\left(S_\beta \sin 2\vartheta - S_\gamma \cos 2\vartheta\right)\right]. \tag{5.28}$$

By measuring how the total signal modulates with ϑ, the value of S_β and S_γ can be inferred by fitting Eq. (5.28). For a horizontally linearly polarized input beam, $S_0'(\vartheta)$ is expected to have no ϑ dependence because the parameters S_β and S_γ are both zero. On the other hand, the circularly polarized input beam will be changed to linearly polarized by the quarter-wave plate depending on the initial handedness (LCP to vertical LP; RCP to horizontal LP), and $S_0'(\vartheta)$ is a sinusoidal function of ϑ.

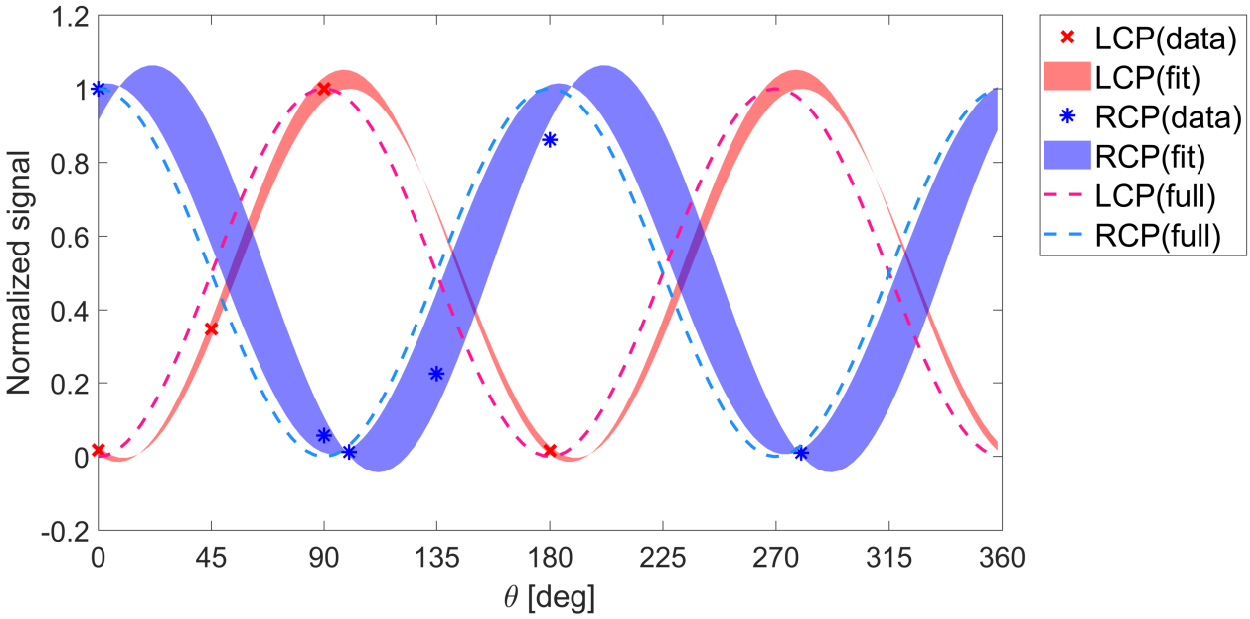

Figure 5.10: **Intensity measurement from the polarimeter:** The data points (×, ∗) represent the measured signal $S_0'(\vartheta)$ for cases of left- and right-handed circular polarization. The color bands show the fit (within the standard error) for each case using Eq. (5.25). The dashed curves show the functions for fully circularly polarized light.

The fundamental beams were found to be very close to linearly or circularly polarized for the corresponding cases, but the 2ω beams were found to be slightly depolarized (change of polarization state). Fig. 5.10 and Table 5.3 show the results from the 2ω light. In Fig. 5.10, the value of vertical axis (normalized signal) is proportional to the total counts of output beam in the CCD. The color bands show the range of curves generated by the fit parameters within the standard errors. For the two cases (LCP and RCP), the fitted curves have the features of circularly polarized beams as the two sinusoidal waves have $\pi/2$ phase shift due to helicities of the beams. However, both sinusoidal curves shift horizontally from the ideal LCP/RCP curve, indicating a decrease of the ellipticity. The table gives for the two cases OAM and SAM values of the fundamental beam, the inferred parameter S_γ , and the resultant SAM value $s_{2\omega}$ calculated using Eq. 5.25 (margin of error for the fitting shown in parentheses).

Case	Fundamental	Fitted S_γ	$s_{2\omega}$
LCP	$l_\omega = +1$, $s_\omega = +1$	+0.97 (0.95 ~ 0.99)	+0.77 (0.71 ~ 0.87)
RCP	$l_\omega = -1$, $s_\omega = -1$	−0.89 (−0.79 ~ −0.98)	−0.61 (−0.47 ~ −0.82)

Table 5.3: The expected OAM and SAM of the fundamental beam for two cases and the derived value of S_γ and the SAM value $s_{2\omega}$.

5.5.1 Possible causes of depolarization

The results show that the SAM of the 2ω light derived from the polarization measurement is significantly less than ± 1. There are several issues might contribute the variations in SAM measurement. First of all, as Eq. (5.25) and Table 5.3 show, small variation of the S_γ measurement can lead to a large difference in the inferred SAM of the 2ω light. It suggests there is a small but definite change of polarization between the fundamental and 2ω beams. The question is what causes the depolarization in the 2ω light measurement. There are several possibilities.

1. Errors in measurement

   (a) There are systematic errors due to the limited accuracy of orientation of the linear polarizer, and random errors caused by shot-to-shot fluctuations due to small but finite thermal lensing in the amplifier crystals.

   (b) Effect of plasma emission on polarimetry: even though the intensity of the plasma emission within the spectral component that can penetrate the band-pass filter is much less than that of the self-generated 2ω beam from the plasma, the plasma emission lasts much longer (10s ns versus ~ 50 fs for the 2ω beam) and therefore can contribute to the total photon count (exposure time of the CCD camera was on level of ms). The plasma emission is thought to be initially polarized but becomes unpolarized with the thermalization of the electron distribution function [138]. The duration of polarized plasma emission may vary with the input beam parameters and the plasma density.

(c) Effect of plasma emission on spiral phase measurement: generally, the spiral phase measurements are less susceptible to the contributions from plasma emission and shot-to-shot fluctuations. Any contribution from plasma emission that reaches the detector which is longer lasting but much weaker does not interfere with the phase measurement of the emergent 2ω beam. In the wave-front sensor measurement, the stray light adds a nearly uniform phase on top of the existing phase of the beam. In the doubleslit interferometer, the stray light without OAM would at worst result in a weak straight fringe pattern which can be easily distinguished from a twisted fringe pattern. The singleshot interferometry can also avoid the influence from the shot-to-shot fluctuations and therefore provides a more reliable measurement.

2. Depolarization of the 2ω radiation

There are physical mechanisms, which are not included in our model, that may depolarize the 2ω radiation in the plasma itself.

(a) As we mention in preview chapter, the light with angular momentum can generate axial magnetic field in plasmas through inverse Faraday effect from both a CP pump beam or a LP vortex pump beam [139, 114]. Axial magnetic field in turn can depolarize the radiated 2ω emission via the Faraday effect.

(b) Laser-ionized plasmas are known to have non-thermal electron velocity distributions and are susceptible to plasma kinetic instabilities [93, 140]. The axial helicoidal magnetic field induced by electron filamentation/Weibel instability can cause depolarization of the 2ω radiation and plasma emission.

(c) Refraction from the density gradients (He^{1+}-He^{2+} and He^{1+}-He) can rotate the polarization plane for a fraction of emitted 2ω light and cause depolarization.

These physical effects are complicated and depend on various parameters such as gas type, plasma density, laser pulse energy, laser pulse duration, and azimuthal mode number. It requires a further study to understand how these effects quantitatively

change the polarization. The opposite but similar amount of shift amount that all these effects suggest the depolarization might occur after the 2ω light has been generated.

5.6 Summary

The results from two different diagnostics indicate that the helical phase structure and the OAM mode index of the second harmonic radiation emitted from an optical-field ionized helium plasma matches the value predicted by the conservation rule Eq. (5.20) for the input SAM and OAM values of 0 or ±1. It is then reasonable to suppose that the conservation rules can be extended to other integer OAM values $l = \pm 2, \pm 3, \pm 4, \ldots$. Therefore, variable orbital angular momentum can be generated this way using the spin-to-orbital angular momentum conversion. It should be noted that the coherent nature of the single-shot double slit measurement provides a better measurement than the azimuthal phase deduced from the WFS which requires subtraction of two independently obtained shots that have equal but opposite mode index. The agreement between the experimental results and theoretical predictions provides strong support that Eq. (5.21) is valid for our experimental parameters.

In conclusion, the source and the conservation of total optical angular momentum in the second harmonic generation from optical-field ionized plasmas has been verified experimentally. The conservation law is accompanied by conversion of the spin-to-orbital angular momentum. The results agree with the conservation rules of angular momentum, which have been derived using the simple electron quiver motion model. In the model, free electrons absorb both spin and orbital angular momentum from the input beam and move accordingly. When these electrons pass through density or intensity gradients, second harmonic currents with the same polarization and phase factor of the beam are generated and angular momentum is transferred to the resultant radiation. In our experiment 2ω radiation originates from plasma regions in the vicinity of the largest intensity gradients of the pump laser. We note that the present mechanism for the current source assumes no dissipation (collisions) or coupling to a plasma mode and the plasma electrons simply catalyze this conversion of the OAM in the harmonic generation process unlike in the case of parametric instabilities

where energy, momentum, and angular momentum conservation involves a collective mode of the plasma.

CHAPTER 6

Conclusions

In this dissertation, several aspects of plasma effects in optical-field ionization (OFI) of gases have been investigated for the first time. This has led to many discoveries. We summarize these first and then elaborate on them.

First, we have used Thomson scattering (TS) diagnostic to confirm the existence of highly non-Maxwellian and anisotropic electron velocity distribution functions as a consequence of the ionization process itself that had been predicted but never been directly measured. We accomplished this goal by using a collinear short-pulse pump-probe Thomson scattering technique.

Second, unexpected observations from the TS experimental data led to further discoveries. With the help of PIC simulations, we were able to connect the enhanced transient spectral feature of Thomson scattering spectra to the unstable modes induced by various kinetic instabilities developed from the highly non-Maxwellian electron distributions. We were able to determine the growth rates of the streaming and the current-filamentation instabilities occuring on a picosecond timescale. Serendipitously, in these measurements, a major source of stray light was the second harmonic light generated from the interaction of the pump beam and OFI plasmas. This gave us a unique opportunity to determine both the origin of this radiation and use it to investigate the conservation laws for the total angular momentum in this nonlinear process in a plasma.

We discovered that the self-generated second-harmonic beam preserves the spin angular momentum properties of the pump beam but in the process acts as a spin-to-orbit angular momentum transformer to conserve the total optical angular momentum. These results

demonstrate the significance and complexity of the plasma effects in ionized gases as well as the powerful combination of simulations and experiments for plasma physics research.

Using a femtosecond laser pulse with different polarization configurations to ionize a helium gas, we are able to produce different types of non-thermal electron velocity distribution functions. Unlike in previous works [43, 41, 42, 141], the non-Maxwellian and anisotropic distributions were directly measured by short-pulse Thomson scattering. When the linear polarization was perpendicular to the scattering plane, a Maxwellian plasma with a cold temperature of 18 ± 2 eV was measured. When the linear polarization was parallel to the scattering plane, we fitted the TS spectra with two-temperature Maxwellian distributions. Fitted temperatures of 20 ± 2 and 180 ± 20 eV are close to the simulated electron temperatures of the He^{1+} and He^{2+} electrons. When the pump laser was circularly polarized, the TS spectra were inconsistent with expected collective scattering for a high density plasma. Instead of observing the usual narrow scattered light features at the Bohm-Gross frequency, we observe much broader features that were almost independent of the plasma density. These were explained in terms of the broad range of unstable frequencies characteristic of the streaming instability. Only when the plasma density was low enough ($\sim 6.6 \times 10^{17}$ cm^{-3}), rather weak but symmetric about the pump frequency TS feature was observed. Both wings of TS spectra could be fitted using the distribution function extracted from the simulation. Even though the measured distributions are the 1D projections of the non-thermal electron distributions on the wave vector defined by TS geometry, strong non-Maxwellian and anisotropic features were demonstrated.

Time-resolved TS measurements at high plasma density show that the non-Maxwellian and anisotropic electron distributions can rapidly drive plasma kinetic instability. This novel TS technique is shown to be an effective tool to study the fast plasma dynamics with a subpicosecond temporal resolution. We measured the growth rate of the electrostatic streaming instability mode from the enhanced electron feature of collective TS. The enhanced signals were extremely transient, lasting for ~ 1 ps for a circularly polarized pump and ~ 5 ps for a linearly polarized pump. We also measured the growth rates of the unstable modes

associated with the filamentation and Weibel instabilities from the enhanced zero-frequency feature of collective TS. While the filamentation mode followed the streaming mode, the Weibel mode grew slowly and lasted much longer. The measurements were compared against self-consistent PIC simulations and theory with good agreements. It was found through experiments and simulations that the thermalization dynamics of OFI helium plasma follows rapid isotropization due to kinetic instabilities followed by the electron-electron, electron-ion collisions, and on an even longer timescale plasma expansion. Thermalized OFI He Plasmas from ultrashort circularly polarized pump lasers were measured for the first time and a thermalized temperature of ~ 80 eV was measure by fitting the TS scattered light. Before the thermalized Maxwellian distributions can be measured at the late delay, we observed from simulations self-organized magnetic fields with helical structures arising due to the Weibel instability, whose temporal evolution and field structure were measured in a recent experiment using electron beams radiography [92].

The second harmonic (2ω) generation from the interaction of underdense plasmas and beams with optical angular momentum has been studied in the non-relativistic limit. The imprints of the angular momentum properties from the pump beam were shown in the measured near-field and far-field 2ω images. The 2ω radiation patterns were consistent with these photons being generated from the intensity gradients of the pump beam in the plasma. Also observed were the combined effects of the spin and orbital angular momentum on the 2ω light source. The observed near-field modes were consistent with the measured values of azimuthal mode index of 2ω beams at the far field. By measuring the helical phase of the 2ω beam using a known spin and orbital angular momentum pump beam, we observed the conversion of spin to orbital angular momentum. These results suggest the total optical angular momentum is conserved in the second-order nonlinear conversion in underdense plasmas. A second independent method that measured the polarization of the second harmonic photons showed that there was some processes that partially depolarized the second harmonic but this does not mean that spin angular momentum is not strictly conserved. Only that photons suffered depolarization after they were produced inside the

plasma. Several possible sources of depolarization were considered.

There is plenty of low hanging fruit (new physics) that still remains to be discovered with the OFI plasma platform. We give three examples here. First, asymmetric distributions such as the ones shown in Fig. 2.7(d) and 2.8(e) are predicted to give bump-on-tail distributions. These distributions are inherently unstable to plasma wave growth due to inverse Landau damping. Second it would be very interesting to show that it is indeed possible to produce a plasma that has a designer distribution functions specially tailored to optimize a particular plasma kinetic instability. Finally, OFI plasmas produced by a circular polarized beam or a vortex beam can absorb angular momentum just like the residual energy from the pump laser. However, how a plasma responds to the acquired angular momentum is still unclear. It is suggested that angular momentum may induce an azimuthal current and result in the axial magnetic field generation that is closely associated with the inverse Faraday effect. Although the inverse Faraday effect has been purported to have been measured in plasmas at relativistic laser intensities, the OFI plasmas will allow careful measurements of this phenomenon to be made for the first time.

APPENDIX A

Additional Thomson Scattering Spectra

A.1 Static-filled helium

Measured spectra and fitting temperatures for other plasma densities in Fig. 3.9.

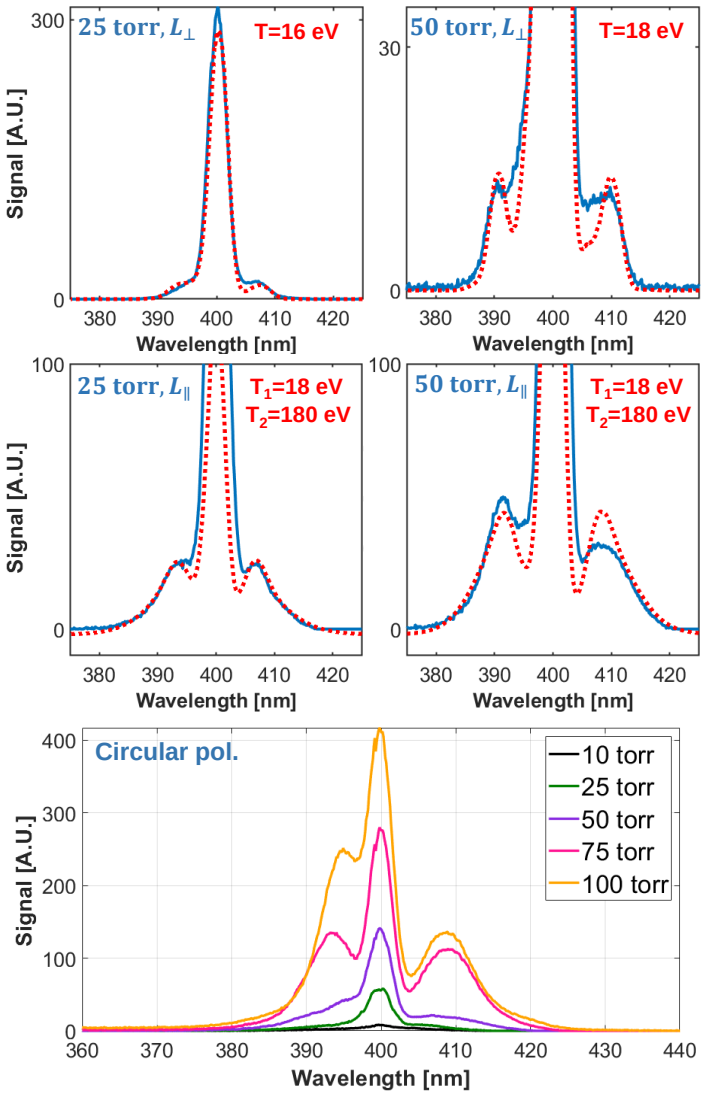

A.2 Gas jet helium

Collinear pump and probe Thomson scattering experiments were also performed using helium gas jet with various backing presures. Although no fitting attempt has been made, the same trend of spectral evolution is observed (as shown in Fig. A.2). In other words at low backing pressures the spectrum is dominated by an intense zero frequency "ion" feature with wings that are due to the onset of collective electron oscillation. At higher backing pressures however, a density dependent electron feature shift is observed with little evidence of the kinetic instabilities observed in plasmas produced in a static fill.

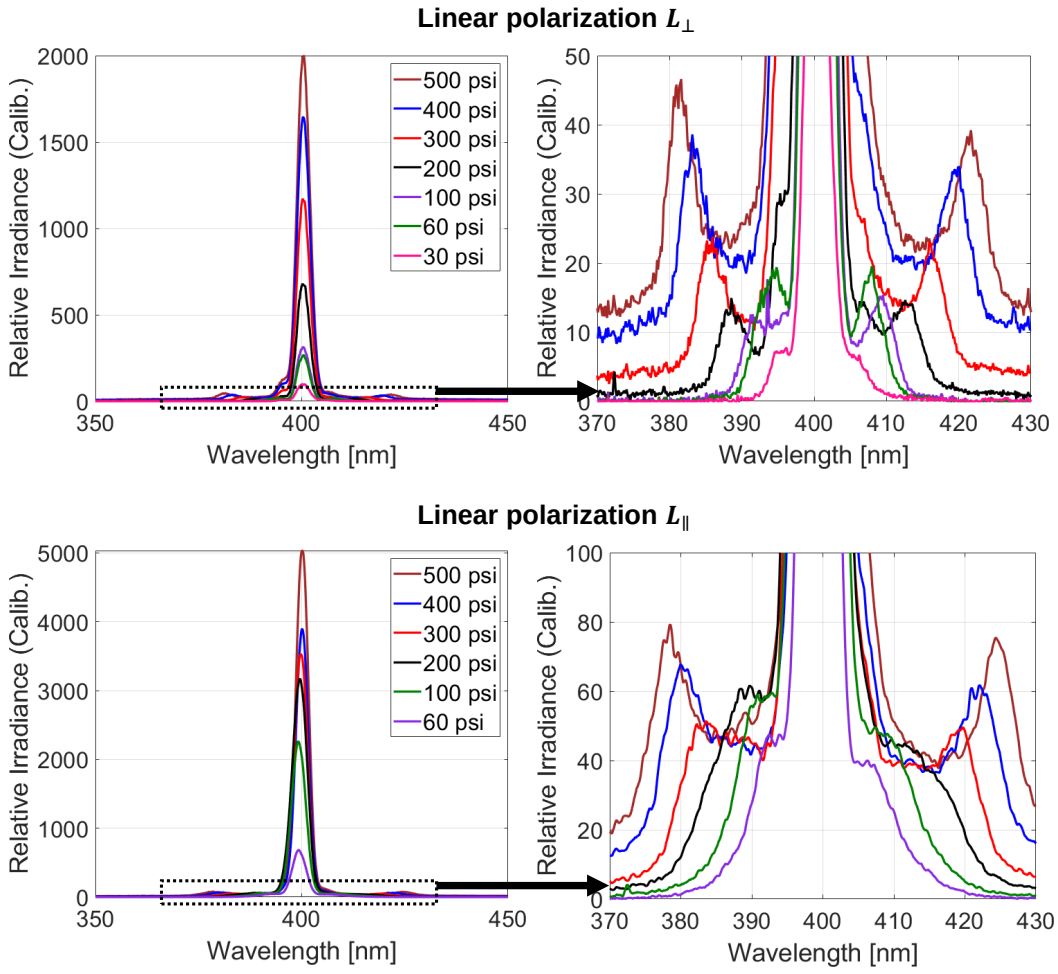

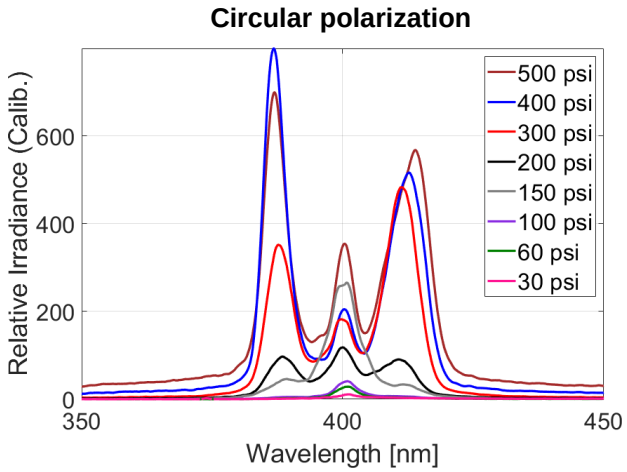

Figure A.1: For circular polarization case, the electron feature of the TS spectrum is dominated by the kinetic instabilities.

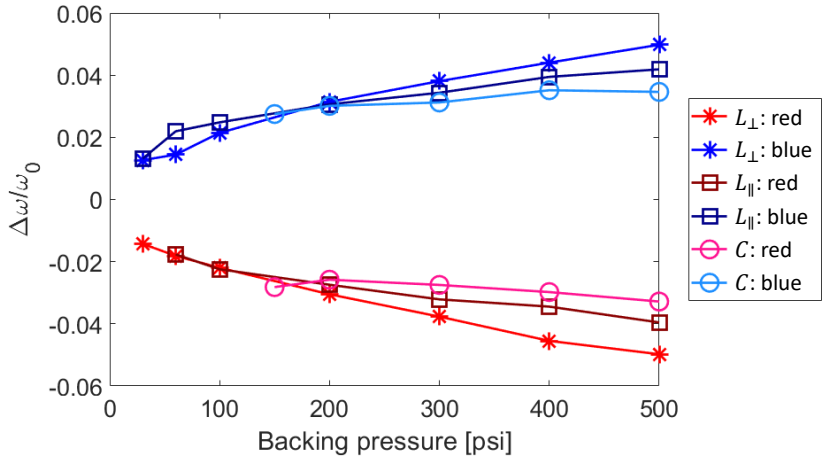

Figure A.2: The measured spectral peak shifts of the electron feature for different backing pressures of the gas jet and different laser polarization ($L_\perp$, $L_\parallel$, C).

A.3 Static-filled hydrogen

Thomson scattering spectra from OFI hydrogen plasmas ionized by linearly and circularly polarized 800-nm lasers are shown. The electron feature of the measured spectra infer similar cold electron distributions as expected for both cases.

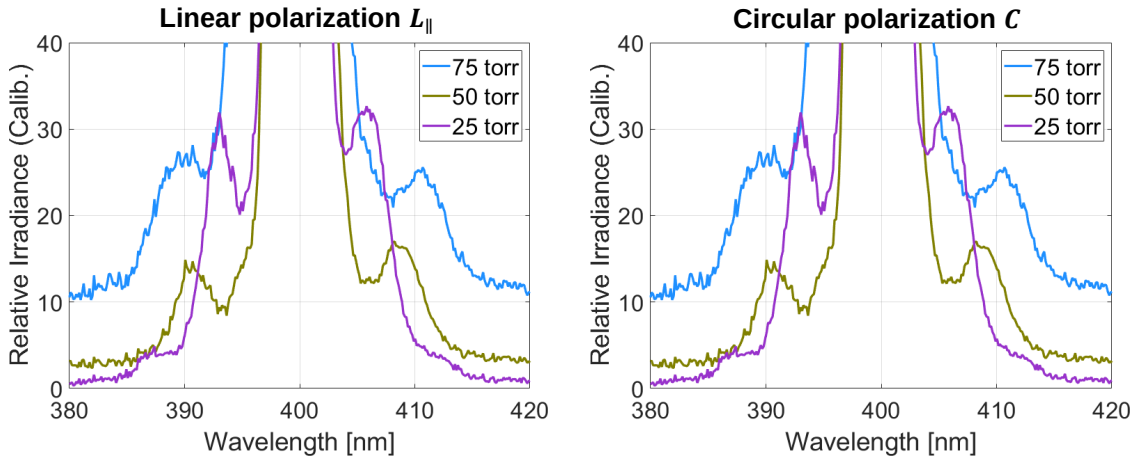

APPENDIX B

Reconstruction of Spiral Phase Distributions

The procedure of generating relative spiral phase distributions (examples are shown in Fig. 5.6) is demonstrated in Fig. B.1. The raw images were recored by the wave-front sensor (PHASICS) and analyzed by the PHASICS software. Several annual masks with different shapes were applied. In the last step, the analyzed segments were spliced to form a complete phase distribution. All collected data and analyzed results are stored in the auther's Dropbox.

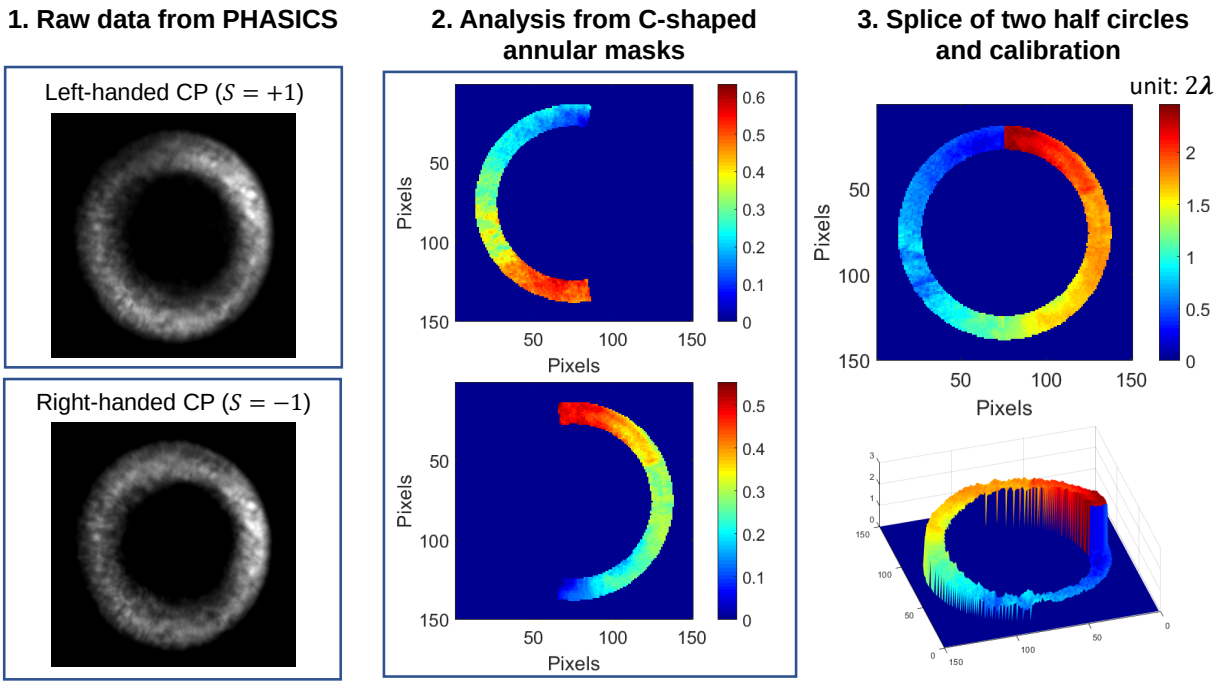

Figure B.1: Construction of the relative spiral phase distribution between SHG beams from left- and right- handed circularly polarized beams.

APPENDIX C

Calibration and Additional Results of the Double-slit Interferometry

C.1 Calibration of the interferometer

The double-slit interferometer setup was calibrated using the fringe patterns generated by 800-nm beams that carried different amounts of OAM. The setup of the plates was set to generate exact azimuthal index $l = 0, +1, +2$. The fringe pattern is shown in Fig. C.1. In these measurements, the fringes at the bottom zone are shifted by about $0.59 \times l$ interference order (the amount of shift from the top to the bottom/the distance between neighboring fringes) to the left compared with the ones at the upper zone.

C.2 Complete sets of measured fringe patterns

The fringe patterns shown in Fig. 5.7 and 5.8 are selected from sets of 10 consecutive shots. The complete sets are demonstrated in Fig. C.2 and C.3 for cases B-E in Table 5.1. The double-slit interferometer measurements are more stable than the WFS measurements.

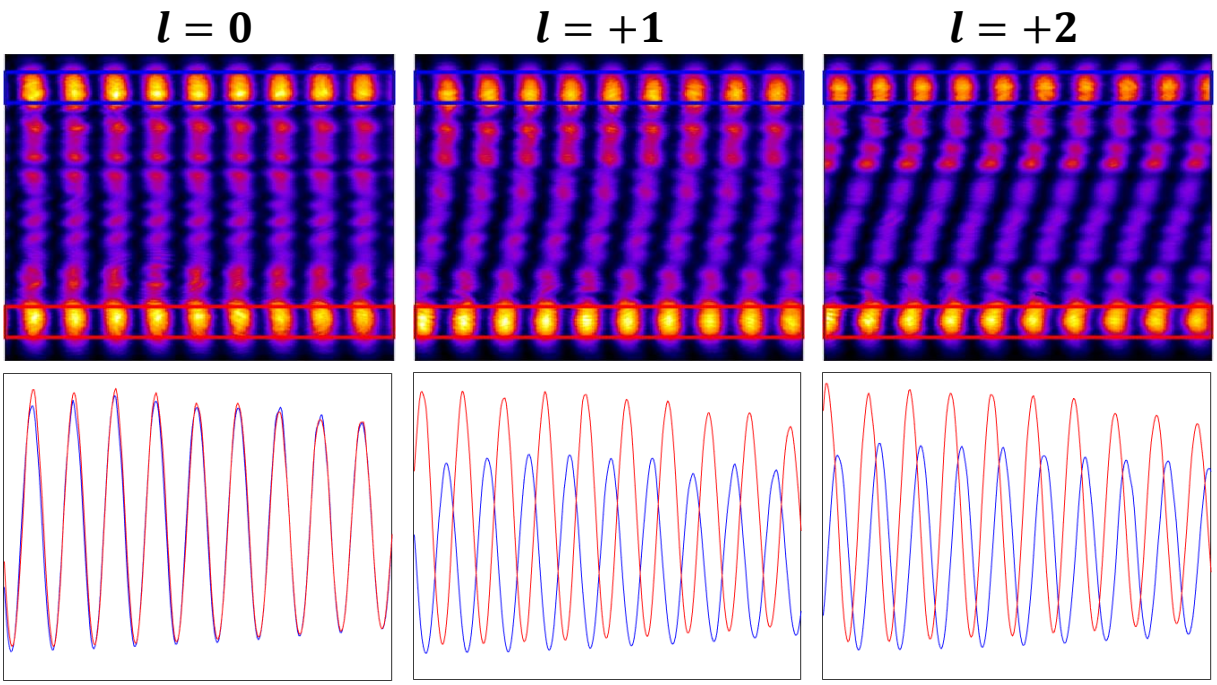

Figure C.1: **Calibration using 800 nm beams.** Top row: the measured fringe patterns from 800-nm beams; Bottom row: the lineouts in the upper zone (blue) and the bottom zone (red). From left to right: cases for $l = 0, +1, +2$.

Case B ($s_\omega = +1$, $l_\omega = 0$): $l_{2\omega} = +1$

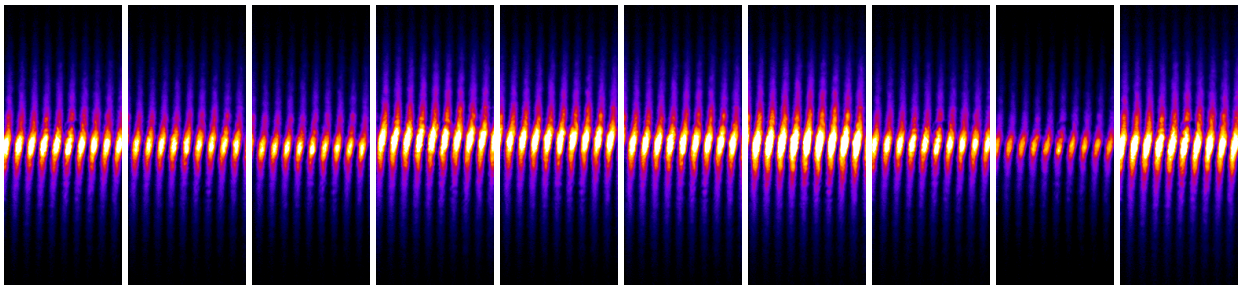

Case B ($s_\omega = -1$, $l_\omega = 0$): $l_{2\omega} = -1$

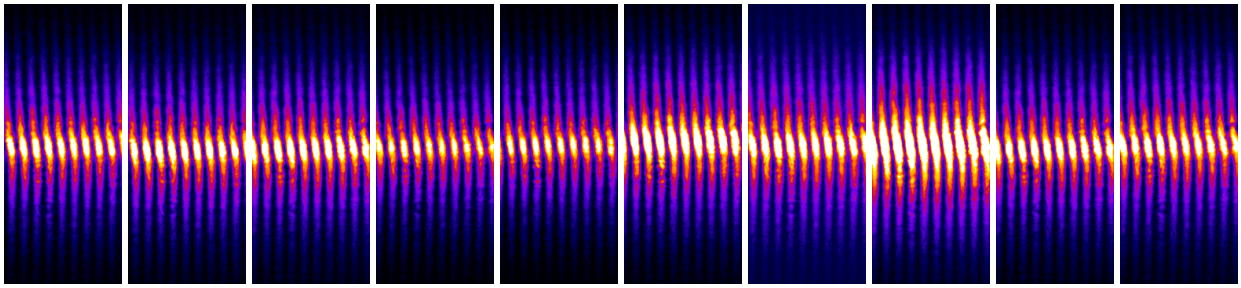

Case C ($s_\omega = 0$, $l_\omega = +1$): $l_{2\omega} = +2$

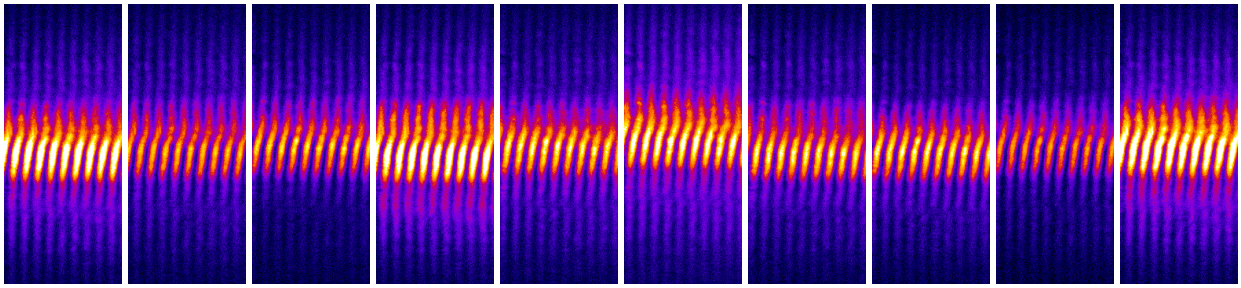

Case C ($s_\omega = 0$, $l_\omega = -1$): $l_{2\omega} = -2$

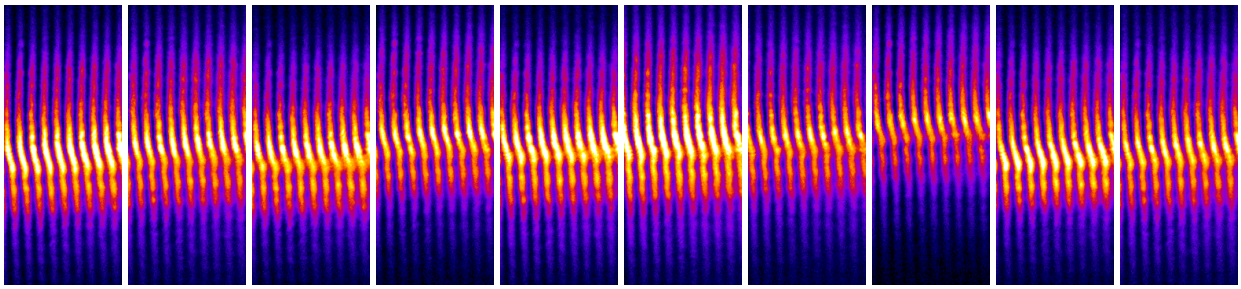

Figure C.2: 10 consecutive shots for case B and C in Table 5.1

Case D ($s_\omega = +1$, $l_\omega = +1$): $l_{2\omega} = +3$

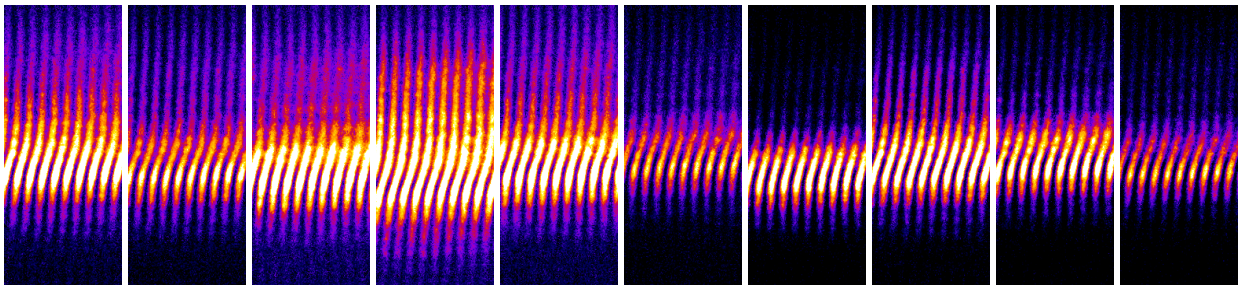

Case D ($s_\omega = -1$, $l_\omega = -1$): $l_{2\omega} = -3$

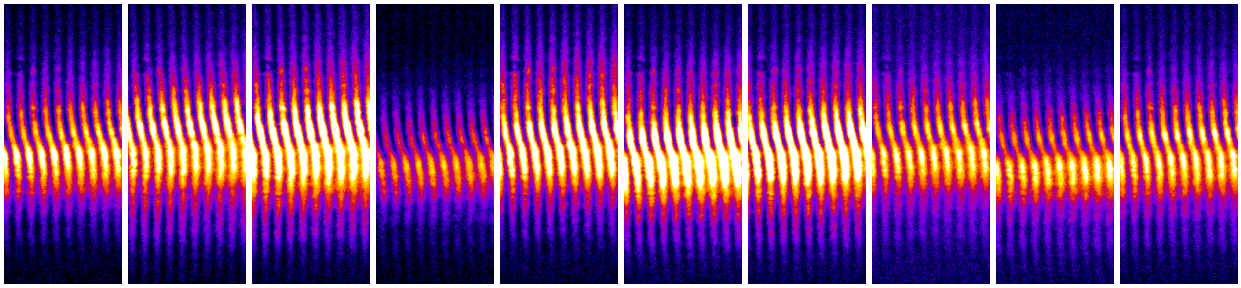

Case E ($s_\omega = -1$, $l_\omega = +1$): $l_{2\omega} = +1$

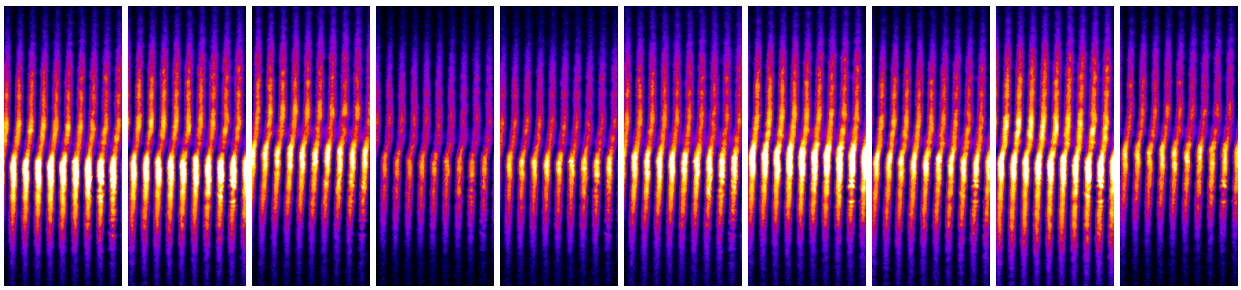

Case E ($s_\omega = +1$, $l_\omega = -1$): $l_{2\omega} = -1$

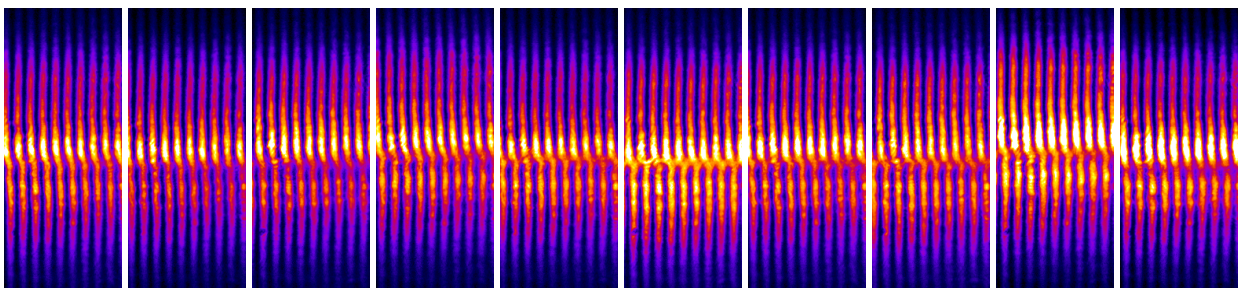

Figure C.3: 10 consecutive shots for case D and E in Table 5.1

APPENDIX D

Codes

D.1 EVDF of OFI plasmas

Tunnel ionization rate, residual energy spectra and electron distribution functions (in Fig. 2.1, 2.2, 2.4, and 2.5) are generated using this Matlab script. The script is also modified to compute the unusual distributions shown in Fig. 2.8.

```
% ========================================================================
% Script file: TunnelIonization_Distribution.m
%
% Define variables:
%   gas: gas type, choose from H(H2), He, ...
%   I_0: laser peak intensity
%   tau_fwhm: laser pulse duration
%   lam_0: laser wavelength
%   Ax1,Ay1: x,y components of the laser field
%   data_point_T: temporal points
%   data_point_Z: spatial points
%
% Note:
%   1. Most parameters in SI unit, some in cgs unit.
% ========================================================================
clear; close all; clc;
set(0,'defaultAxesFontName', 'Helvetica');
%-- Input parameters
gas= 'He';
I_0= 1*1e17;          % W/cm^2
tau_fwhm= 50*1e-15;  % sec
lam_0= 0.8*1e-6;       % m
Ax1 = 1;
Ay1 = 1;
data_point_T= 100001;
data_point_Z= 10001;
% ------------------------------------------------------------------------
switch gas
    case 'H'
        Z=1; l=0; m=0;
        U_i=13.6;   % ionization potential; eV
    case 'He'
        Z=2; l=[0  0]; m=[0  0];
        U_i=[24.6  54.4];
    case 'N'
```

```
    case 'Ne'
    case 'Ar'
    case 'Kr'
    case 'Xe'
end
%-- Fundamental constant
C=299792458; Me=9.109e-31; e=1.602e-19; hbar=1.055e-34; epsilon0=8.854e-12; U_h=13.6;
omg_0= 2*pi*C/lam_0;
n_eff= (1:Z)./sqrt(U_i/U_h);
%-- Other constants
const_K= 1/(4*pi*epsilon0);
omega_a= Me*e^4/(hbar^3)*const_K^2;
E_a= Me^2*e^5/(hbar^4)*const_K^3;
Up= e^2*(I_0*1e4)/(2*C*epsilon0*Me)/(omg_0^2)/e;
E_0= sqrt((2/C/epsilon0)*I_0*1e4/(Ax1^2+Ay1^2));
%% ------------------------------------------------------------------------
ts = linspace(-tau_fwhm*2,0,data_point_T);
zs = linspace(0,4*1e-6,data_point_Z);

for k=1:length(zs)
%- Define e-field in x and y, with a phase delay of pi/2
Ex_t = Ax1*E_0*exp(-(1.177/tau_fwhm*ts).^2).*cos(omg_0*ts-(2*pi/lam_0)*zs(k));
Ey_t = Ay1*E_0*exp(-(1.177/tau_fwhm*ts).^2).*sin(omg_0*ts-(2*pi/lam_0)*zs(k));
E_t= sqrt(Ex_t.^2+Ey_t.^2);     % field strength
I_t = C*epsilon0*abs(E_t).^2;

%- Calculate ionization rate using ADK model, using the eq.(3) of J.Opt.Soc.Am.B 6,1195 (1989)
for n=1:Z
    const_wt1=(2*l(n)+1)*factorial(l(n)+abs(m(n)))/(2^abs(m(n))) ...
        /factorial(abs(m(n)))/factorial(l(n)-abs(m(n)));
    const_wt2= 2*n_eff(n)-abs(m(n))-1;
    w_t(n,:) = 2*omega_a*const_wt1*(U_i(n)/U_h)*(2*((U_i(n)/U_h)^(3/2))*E_a./abs(E_t)).^const_wt2 ...
        .*exp(-(2/3)*((U_i(n)/U_h)^(3/2))*(E_a./abs(E_t)));

    % No recombination has been considered!
    if n==1
        n_t(n,:) = exp( -cumtrapz(ts,w_t(n,:)));
        n_t(isnan(n_t)) = 0;
        n_t(n+1,:) = 1-n_t(n,:);
        dn_t(n+1,:)= [0 diff(n_t(n+1,:))];
    else
        n_t_temp = exp( -cumtrapz(ts,w_t(n,:)) );
        n_t_temp(isnan(n_t_temp)) = 0;
        n_t(n+1,:) = 1-n_t_temp;
        n_t(n,:) = n_t(n,:)-n_t(n+1,:);
        dn_t(n+1,:)= [0 diff(n_t(n+1,:))];
    end
end
%- Electron density
ne_t=zeros(1,data_point_T);
for n=1:Z
    ne_t=ne_t+dn_t(n+1,:);
end
%- Initial velocity
Vx_t= Ax1*(e*E_0/Me/omg_0)*exp(-(1.177/tau_fwhm*ts).^2).*sin(omg_0*ts-(2*pi/lam_0)*zs(k));
Vy_t=-Ay1*(e*E_0/Me/omg_0)*exp(-(1.177/tau_fwhm*ts).^2).*cos(omg_0*ts-(2*pi/lam_0)*zs(k));
%- Kinetic energy (residual energy)
UE_t=0.5*Me*(Vx_t.^2+Vy_t.^2)/e;
```

```
%- Resolutions
V_edges= (-(ceil(sqrt(5*Up*e/Me)/100000)*100000):100000:(ceil(sqrt(5*Up*e/Me)/100000)*100000));
V_vec= (V_edges(1:end-1)+V_edges(2:end))/2;
E_edges= 0:2:(ceil((2*Up)/100)*100);
E_vec= (E_edges(1:end-1)+E_edges(2:end))/2;

if k==1
    NE= zeros(1,length(E_vec));
    NVx= zeros(1,length(V_vec));
    NVy= zeros(1,length(V_vec));
    NV_2D= zeros(length(V_vec),length(V_vec));
end

E_bin= discretize(UE_t,E_edges);
for i=1:data_point_T
    NE(E_bin(i))=NE(E_bin(i))+ne_t(i);
end

Vx_bin= discretize(Vx_t,V_edges);
Vy_bin= discretize(Vy_t,V_edges);
for i=1:data_point_T
    NVx(Vx_bin(i))=NVx(Vx_bin(i))+ne_t(i);
    NVy(Vy_bin(i))=NVy(Vy_bin(i))+ne_t(i);
    NV_2D(Vx_bin(i),Vy_bin(i))=NV_2D(Vx_bin(i),Vy_bin(i))+ne_t(i);
end
end
%% ------------------------------------------------------------------------
color_line= [rgb('Black'); rgb('Blue'); rgb('DeepPink')];
%- Fig.1: plot the relative population in laser field
fig1=figure(1);
area(ts*1e15,I_t*1e-4,'EdgeColor','none','FaceColor',rgb('DarkGray'));
ax1=gca;
set(gcf,'color','w','position',[100 200 700 500]);
set(ax1,'YColor','k','Box','off','YAxisLocation','right','xlim',[-80 0],'FontSize',18);
ylabel('Laser Intensity (W/cm^{2})'); xlabel('Time (fs)');
ax2=axes('Position',get(ax1,'Position'),'color','none','Box','off','xlim',[-80 0],'FontSize',18);
for k=1:(Z+1)
    line(ts*1e15,n_t(k,:),'Color',color_line(k,:),'LineWidth',2.5);hold on;
    if k==1
        legend_str = [gas '  '];
    else
        legend_str = [legend_str; strcat(gas,num2str(k-1),'+')];
    end
end
ylabel('Relative ion population','FontSize',18)
legend_str= cellstr(legend_str); legend(legend_str,'FontSize',22);

%- Fig.2: plot the electron energy distribution
fig2=figure(2);
plot(E_vec,NE,'b','LineWidth',2.5);
set(gcf,'color','w','position',[100 200 700 500]);
set(gca,'FontSize',18,'xlim',[0 1500],'ylim',[0 inf]);
xlabel('Electron energy (eV)'); ylabel('N(E) (R.U.)');

%- Fig.3: 2D distribution of electron velocity distribution
V_vec_c=V_vec/C;
fig3=figure(3);
imagesc(V_vec_c,V_vec_c,NV_2D);
xlabel('p_y [m_{e}c]'); ylabel('p_x [m_{e}c]'); axis square; grid on;
```

```
set(gca,'FontSize',20,'xlim',[-0.1 0.1],'ylim',[-0.1 0.1], ...
    'xtick',[-0.1 -0.05 0 0.05 0.1],'ytick',[-0.1 -0.05 0 0.05 0.1],'ydir','normal');
set(gcf,'color','w','Position',[900 200 700 600]);

%- Fig.4: Lineout of the distribution of electron velocity distribution
fig4=figure(4);
plot(V_vec_c,NVx,'color','k');
xlabel('p_x [m_{e}c]'); grid on;
set(gca,'FontSize',20,'xlim',[-0.1 0.1])
set(gcf,'color','w','Position',[950 200 600 400]);
```

D.2 Thomson scattering form factor

This Matlab script computes the form factor (Eq. (3.3)) of Thomson scattering spectral density function.

```
% ================================================================
% Script file: Thomson.m
%
% Define variables:
%   Type_cal: type of distribution function
%             1- single Maxwellian
%             2- two-Maxwellian
%   Type_probe: option of the probe
%               1- Single wavelength input
%               2- Broadband wavelength input
%               3- Spectrum from input file
%
% Note:
%   1. Require the tables generated by wtable.m and function Zprime.m
%      These function can be found in Reference []
% ================================================================
clear; close all; clc;
set(0,'defaultAxesFontName', 'Helvetica');
global C constants sarad Vpar Vperp ud gammarad Z fract Me Mi Length_data
%-- Input parameters
Type_cal = 1;
ud= 0;
%- Plasma conditions
% Te= [0.5];    % electron temperature KeV
Te= [0.02 0.05 0.1 0.2 0.5 1];
Ti= 0.000025;  % ion temperature KeV
ne= 1.6e18;      % plasma density in cm^(-3) 0.9e21
if Type_cal==2
    Te = [0.02    0.2];
    ud = 1.0e+07 *[ 0   0 ];
    ne_fra = [0.5 0.5];
end
Z= 2;         % ionization level of plasma
A= 4;         % atomic mass
fract= 1;     % fraction of each ion species
%- Probe beam
lamL=0.400e-4;          % laser wavelength: unit: cm
```

```
lamL_range = 50;        % wavelength range: unit: nm
lamL_res = 10000;
Type_probe = 1;         % Option 1: Single wavelength input
                        % Option 2: Broadband wavelength input
                        % Option 3: Spectrum from input file
%- Option 2
BWidthL = 3.5;  % unit: nm
PResolution2 = [-0.005e-4 0.005e-4 10001];
%- Option 3
Folder_probe = '';  % directory of the input file
File_probe = 'probe_spectrum.txt';  % name of the file
PResolution3 = 0;    % 0 means original resolution
%- End of Option

%--- Experiment geometry
sa= 60;                         % scattering angle in degree or
dphi=90;                        % the angle between the plane of polarization and the scattering plane in
    degree
L = 100*1e-4;                   % interaction length in cm
SA_lens= pi*(5.08^2)/(25^2);    % solid angle of the collecting optics

%--- Other parameter
Vpar=0;  % fluid velocity parallel to the Thomson laser (ki) in cm/s
Vperp=0; % fluid velocity perp to the Thomson laser (ki) in cm/s, in the scattering plane
% ud=0;  % relative drift velocity between the electrons and ions in cm/s along k
gamma=0; % the angles between k and the drift velocity ud

% ------------------------------------------------------------------------
%- Constant quantities
C=2.99792458e10;                % velocity of light cm/sec
Me=510.9896/C^2;                % electron mass KeV/C^2
Mp=Me*1836.1;                   % proton mass KeV/C^2
Mi=A*Mp;                        % ion mass
re=2.8179e-13;                  % classical electron radius cm
e=1.6e-19;                      % electron charge
Esq=Me*C^2*re;                  % sq of the electron charge KeV-cm
constants = sqrt(4*pi*Esq/Me);  % sqrt(4*pi*e^2/Me)
sarad=sa*2*pi/360;              % scattering angle in radians
dphirad = dphi*2*pi/360;        % dphi in radians
gammarad = gamma*2*pi/360;
omgL=2*pi*C/lamL;
if Type_cal==1
    Num_Te= length(Te);
    Num_ne= length(ne);
elseif Type_cal==2
    Num_Te= 1;
    Num_ne= 1;
end

%- Probe type
if Type_probe==2
    lambda_fwhm = BWidthL*10^-7;
    delta_lam = linspace(PResolution2(1),PResolution2(2),PResolution2(3));
    Ew = 10.*exp(-(2*log(2)/(lambda_fwhm)^2)*(delta_lam.^2));
    Iw = Ew.^2;
    Input_data_temp = fliplr(Iw);
    lam_temp = lamL+delta_lam;
    omg_temp= fliplr(2*pi*C./lam_temp);
    Input_omg=linspace(omg_temp(1),omg_temp(end),PResolution2(3));
```

```
    Input_data = interp1(omg_temp,Input_data_temp,Input_omg);
elseif Type_probe==3
    cd(Folder_probe)
    Temp_input = dlmread(File_probe);
    Input_dataX = Temp_input(1,:);
    Input_dataY = Temp_input(2,:);
    if PResolution3==0
        Input_omg_temp =fliplr(2*pi*C./(Input_dataX*10^-7));
        Input_omg=linspace(Input_omg1(1),Input_omg1(end),length(Input_dataX));
        Input_data=interp1(Input_omg_temp,fliplr(Input_dataY),Input_omg);
    else
        Input_omg_temp =fliplr(2*pi*C./(Input_dataX*10^-7));
        Input_omg=linspace(Input_omg_temp(1),Input_omg_temp(end),PResolution3);
        Input_data=interp1(Input_omg_temp,fliplr(Input_dataY),Input_omg);
    end
elseif Type_probe~=1
    error('Must identify probe type.');
end

Length_data = lamL_range*lamL_res+1;
% -------------------------------------------------------------------------
%% CALCULATION
%- Thomson scattering parameter (alpha)
Alpha = round(1.075e-4*lamL./sin(sarad/2).*sqrt(ne./(Te*1e3)),2);

%- Calculate form factor
if Type_cal==1
    omgs = linspace(2*pi*C/(lamL+lamL_range*1e-7),2*pi*C/(lamL-lamL_range*1e-7),lamL_range*lamL_res+1);
  if Alpha>10
    omgpe=constants*sqrt(ne);
    EPW_factor=QuadrSolver(1-9*(1/Alpha)^2-150*(1/Alpha)^4,...
        2+6*(1/Alpha)^2+60*(1/Alpha)^4,...
        -3*(1/Alpha)^2-15*(1/Alpha)^4);
    omega_IAW= 4*pi/lamL*sin(sarad/2)*sqrt(Alpha^2/(1+Alpha^2)*Z*Te/Mi+3*Ti/Mi);  % Ion wave
    I_omgs_1= find(omgs>(omgL-(1.016271996)*omgpe),1)-1;
    I_omgs_2= find(omgs>(omgL-(1.016271996)*omgpe),1);
    I_omgs_3= find(omgs>(omgL-1.5*omega_IAW),1)-1;
    I_omgs_4= find(omgs>(omgL+1.5*omega_IAW),1)+1;
    I_omgs_5= find(omgs>(omgL+(1.0171895798)*omgpe),1)-1;
    I_omgs_6= find(omgs>(omgL+(1.0171895798)*omgpe),1);
    omgs_add_1 = linspace(omgs(I_omgs_1),omgs(I_omgs_2),20000000);    % 20000000
    omgs_add_2 = linspace(omgs(I_omgs_5),omgs(I_omgs_6),20000000);    % 20000000
    omgs_add_3 = linspace(omgs(I_omgs_3),omgs(I_omgs_4),20000000);    % 20000000
    omgs = [omgs(1:I_omgs_1-1) omgs_add_1  omgs(I_omgs_2+1:I_omgs_3-1) omgs_add_3 ...
        omgs(I_omgs_4+1:I_omgs_5-1) omgs_add_2 omgs(I_omgs_6+1:end)];
    Length_data = length(omgs);
  end
    lamS = 2*pi*C*(1e-2)./fliplr(omgs);

switch Type_probe
    case 1
        for I_Te=1:Num_Te
            [FF_omg]=Cal_FormFactor(ne,Te(I_Te),Ti,omgL,omgs);

            Rs_omg{I_Te} = SA_lens*re^2*L*ne*(1-sin(sarad)^2*cos(dphirad)^2)*FF_omg;
            Rs_lam{I_Te} = fliplr(Rs_omg{I_Te})*1e10;
        end
    case 2
        lam_factor = Input_data;
```

```
        lam_factor= lam_factor/sum(lam_factor);
        for I_Te=1:Num_Te
            for I_temp=1:length(Input_omg)
                omgL_in = Input_omg(I_temp);
                [FF_omg]=Cal_FormFactor(ne,Te(I_Te),Ti,omgL_in,omgs);
                FF_lam = fliplr(FF_omg);

                Rs_omg_temp = SA_lens*re^2*L*ne*(1-sin(sarad)^2*cos(dphirad)^2)*FF_omg;
                Rs_lam_temp = FF_lam;

                if I_temp==1
                    Rs_omg{I_Te} = zeros(1,length(lamS));
                    Rs_lam{I_Te} = zeros(1,length(lamS));
                end
                Rs_omg{I_Te} = Rs_omg{I_Te} + Rs_omg_temp*lam_factor(I_temp);
                Rs_lam{I_Te} = Rs_lam{I_Te} + Rs_lam_temp*lam_factor(I_temp);
            end
        end
    case 3
        lam_factor = Input_data;
        lam_factor= lam_factor/sum(lam_factor);
        for I_Te=1:Num_Te
            for I_temp=1:length(Input_omg)
                omgL_in = Input_omg(I_temp);
                [FF_omg]=Cal_FormFactor(ne,Te(I_Te),Ti,omgL_in,omgs);
                Rs_omg_temp = SA_lens*re^2*L*ne*(1-sin(sarad)^2*cos(dphirad)^2)*FF_omg;
                if I_temp==1
                    Rs_omg{I_Te} = zeros(1,length(lamS));
                    Rs_lam{I_Te} = zeros(1,length(lamS));
                end
                Rs_omg{I_Te} = Rs_omg{I_Te} + Rs_omg_temp*lam_factor(I_temp);
            end
        end
        Rs_lam{I_Te} = fliplr(Rs_omg{I_Te})*1e23;
end
end

if Type_cal==2
    omgs = linspace(2*pi*C/(lamL+lamL_range*1e-7),2*pi*C/(lamL-lamL_range*1e-7),lamL_range*lamL_res+1);
    lamS = 2*pi*C*(1e-2)./fliplr(omgs);
switch Type_probe
    case 1
        [FF_omg]=Cal_FormFactor_2(ne,Te,Ti,omgL,omgs,ne_fra);
        Rs_omg = SA_lens*re^2*L*ne*(1-sin(sarad)^2*cos(dphirad)^2)*FF_omg;
        Rs_lam = fliplr(Rs_omg)*1e10;
    case 2
        lam_factor = Input_data;
        lam_factor= lam_factor/sum(lam_factor);
        for I_temp=1:length(delta_lam)
                lamL_temp = lamL+delta_lam(I_temp);
                omgL=2*pi*C/lamL_temp;
                lamS = linspace(lamL-(lamL_range*1e-7),lamL+(lamL_range*1e-7),lamL_range*lamL_res+1)*1e-2;
                omgs = fliplr(2*pi*C*(1e-2)./lamS);
                [FF_omg]=Cal_FormFactor_2(ne,Te,Ti,omgL,omgs,ne_fra);
                FF_lam = fliplr(FF_omg).*fliplr([omgs(2)-omgs(1) diff(omgs)])./[lamS(2)-lamS(1) diff(lamS)
                    ];

                Rs_omg_temp = SA_lens*re^2*L*ne*(1-sin(sarad)^2*cos(dphirad)^2)*FF_omg;
                Rs_lam_temp = SA_lens*re^2*L*ne*(1-sin(sarad)^2*cos(dphirad)^2)*FF_lam*1e-9;
```

```
                if I_temp==1
                    Rs_omg = zeros(1,length(lamS));
                    Rs_lam = zeros(1,length(lamS));
                end
                Rs_omg = Rs_omg + Rs_omg_temp*lam_factor(I_temp);
                Rs_lam = Rs_lam + Rs_lam_temp*lam_factor(I_temp);
        end
    case 3
        lam_factor = Input_data;
        lam_factor= lam_factor/sum(lam_factor);
        for I_temp=1:length(Input_omg)
                omgL_in = Input_omg(I_temp);
                [FF_omg]=Cal_FormFactor_2(ne,Te,Ti,omgL_in,omgs,ne_fra);
                Rs_omg_temp = SA_lens*re^2*L*ne*(1-sin(sarad)^2*cos(dphirad)^2)*FF_omg;
                if I_temp==1
                    Rs_omg = zeros(1,length(lamS));
                    Rs_lam = zeros(1,length(lamS));
                end
                Rs_omg = Rs_omg + Rs_omg_temp*lam_factor(I_temp);
        end
        Rs_lam = fliplr(Rs_omg)*1e23;
end
end

%% ------------------------------------------------------------------------
color_line=[rgb('DarkBlue');rgb('DeepPink');rgb('Green');rgb('Brown');rgb('Orange');rgb('Red');rgb('Gray')
    ;rgb('DarkBlue')];

%-- Fig.1 Spectral density in wavelenght with various electron tempertures
for i=1:Num_Te
    if i==1; Text_legend = {[num2str(Te(1)*1e3) ' eV, \alpha=' num2str(Alpha(1))]};
    else Text_legend = {Text_legend{:} [num2str(Te(i)*1e3) ' eV, \alpha=' num2str(Alpha(i))]};
    end
end
fig1=figure(1);
if Type_cal==1
    for i=1:Num_Te
        plot(lamS*1e9,Rs_lam{i},'Color',color_line(i,:),'Linestyle','-','LineWidth',2.5); hold on;
    end
else
    plot(lamS*1e9,Rs_lam,'Color',color_line(1,:),'Linestyle','-','LineWidth',2);
end
xlabel('Wavelength [nm]'); ylabel('Scattering power ratio per nm (P_s/P_i)');
set(gca,'FontSize',20,'XLim',[350 450],'YScale','linear','YLim',[0 4e-14]);
set(gcf,'color','w','Position',[100 100 1200 650]);
legend(Text_legend,'FontSize',25);

%-- Fig.2 Spectral density in wavelenght with various electron densities
% for i=1:Num_ne
%     if i==1; Text_legend = {[num2str(ne(1)) ' cm^{-3}, \alpha=' num2str(alpha(1))]};
%     else Text_legend = {Text_legend{:} [num2str(ne(i)) ' cm^{-3}, \alpha=' num2str(alpha(i))]};
%     end
% end
% fig2=figure(2);
% if Type_cal==1
%     for i=1:Num_Te
%         plot(omgs,Rs_omg{i},'Color',color_line(i,:),'LineWidth',1.5); hold on;
%     end
% else
```

```
%      plot(omgs,Rs_omg,'Color',color_line(i,:),'LineWidth',1.5);
% end
% xlabel('Frequency'); ylabel('Spectral density [A.U.]');
% set(gca,'FontSize',20,'XLim',[(4.58039605E15) (4.58039612E15)],'YLim',[0 1*1e-23],'YScale','linear');

%%%%%%%%%%%%%%%%%%%%%%%%%%%%%%%%%%%%%%%%%%%%%%%%%%%%%%%%%%%%%%%%%%%%%%%%%%%%%%%

function [FF_omg] = Cal_FormFactor(ne,Te,Ti,omgL,omgs)
global C constants sarad Vpar Vperp ud gammarad Z fract Me Mi
%- Calculating k and omega vectors
omgpe=constants*sqrt(ne);        % plasma frequency rad/s
omg = omgs-omgL;
ks=sqrt(omgs.^2-omgpe^2)/C;
kL=sqrt(omgL^2-omgpe^2)/C;       % laser wavenumber in rad/cm
k=sqrt(ks.^2+kL^2-2*kL*ks*cos(sarad));
kdotv = (kL-ks*cos(sarad))*Vpar - ks*sin(sarad)*Vperp;
omgdop = omg-kdotv;
clear ks kL kdotv;
%-- Plasma Parameters
%- electrons
vTe=sqrt(Te/Me);
klde=(vTe/omgpe).*k;
%- ions
Zbar = sum(Z.*fract);
ni = fract*ne./Zbar;
omgpi = constants.*Z.*sqrt(ni.*Me./Mi);
vTi=sqrt(Ti./Mi);
kldi=transpose(vTi./omgpi)*k;
%-- Electron Susceptibility
%-- calculating normalized phase velocity (xi's) for electrons
xd = ud/(sqrt(2.)*vTe)*cos(gammarad);
xie = omgdop./(k*sqrt(2.)*vTe) - xd;
Zpe = Zprime(xie);
chiE = -0.5./(klde.^2).*(Zpe(1,:)+sqrt(-1)*Zpe(2,:)) ;
clear klde Zpe;
%-- Ion Susceptibilities
%-- finding dervative of plasma dispersion function along xii array
xii=1./transpose((sqrt(2.)*vTi))*(omgdop./k);
[num_species, num_pts] = size(xii);
chiI=zeros(num_species, num_pts);

for m=1:num_species
    Zpi=Zprime(xii(m,:));
    chiI(m,:)=-0.5./(kldi(m,:).^2).*(Zpi(1,:)+sqrt(-1)*Zpi(2,:));
end
chiItot = sum(chiI,1);  %chiItot=0;
clear kldi Zpi chiI
%-- Form factor from electron contribution and ion contribution
econtr = sqrt(2*pi)./(vTe*k).*exp(-xie.^2).*abs((1+chiItot)./(1+chiItot+chiE)).^2;
icontr = Z*sqrt(2*pi)./(vTi*k).*exp(-xii.^2).*abs(chiE).^2./abs(1+chiItot+chiE).^2;  %icontr=0;
% icontr = 2*Ti/Te*klde.^2./omgdop.*abs(chiE).^2./abs(1+chiItot+chiE).^2.*imag(chiItot);
FF_omg = econtr + icontr;
end

function [FF_omg] = Cal_FormFactor_2(ne,Te,Ti,omgL,omgs,n_fra)
global C constants sarad Vpar Vperp ud gammarad Z fract Me Mi Length_data
%- Calculating k and omega vectors
omgpe=constants*sqrt(ne);        % plasma frequency rad/s
omg = omgs-omgL;
```

```
ks=sqrt(omgs.^2-omgpe^2)/C;
kL=sqrt(omgL^2-omgpe^2)/C;       % laser wavenumber in rad/cm
k=sqrt(ks.^2+kL^2-2*kL*ks*cos(sarad));
kdotv = (kL-ks*cos(sarad))*Vpar - ks*sin(sarad)*Vperp;
omgdop = omg-kdotv;
clear ks kL kdotv;
%-- Electron
vTe=sqrt(Te/Me);
%- Calculate electron susceptibility
chiEtot = zeros(1,Length_data);
for i=1:(length(Te))
    chiEtot=  chiEtot + n_fra(i)*Cal_chiE(vTe(i),ud(i),omgpe,k,omgdop);          % Cal_chiE(vTe,ud,omgpe,k,
        omgdop)
end
%- Calculate electron distribution
disE=zeros(1,Length_data);
for i=1:length(Te)
    disE = disE + 1/sqrt(2*pi)./(vTe(i)).*exp(-Cal_xie(vTe(i),omgdop,k,ud(i),gammarad).^2)*n_fra(i);  %
        (1/sqrt(2*pi)./(vTe(i)).*
end
%-- Ion
Zbar = sum(Z.*fract);
ni = fract*ne./Zbar;
omgpi = constants.*Z.*sqrt(ni.*Me./Mi);
vTi=sqrt(Ti./Mi);
kldi=transpose(vTi./omgpi)*k;
%-- finding dervative of plasma dispersion function along xii array
xii=1./transpose((sqrt(2.)*vTi))*(omgdop./k);
[num_species, num_pts] = size(xii);
chiI=zeros(num_species, num_pts);

for m=1:num_species
    Zpi=Zprime(xii(m,:));
    chiI(m,:)=-0.5./(kldi(m,:).^2).*(Zpi(1,:)+sqrt(-1)*Zpi(2,:));
end
chiItot = sum(chiI,1);

econtr = ((2*pi)./k).*disE.*abs((1+chiItot)./(1+chiItot+chiEtot)).^2;
icontr = Z*sqrt(2*pi)./(vTi*k).*exp(-xii.^2).*abs(chiEtot).^2./abs(1+chiItot+chiEtot).^2;
FF_omg = econtr + icontr;
end

function [chiE_s] = Cal_chiE(vTe,ud,omgpe,k,omgdop)
global gammarad
%-- Plasma Parameters
%- electrons
klde=(vTe/omgpe).*k;
%-- Electron Susceptibility
%-- calculating normalized phase velocity (xi's) for electrons
Zpe_s = Zprime(Cal_xie(vTe,omgdop,k,ud,gammarad));
chiE_s = -0.5./(klde.^2).*(Zpe_s(1,:)+sqrt(-1)*Zpe_s(2,:)) ;
end

function [xie_s] = Cal_xie(vTe_s,omgdop,k,ud_s,gammarad)
    xd = ud_s/(sqrt(2.)*vTe_s)*cos(gammarad);
    xie_s = omgdop./(k*sqrt(2.)*vTe_s) - xd;
end
```

D.3 Synthetic interferogram

This Matlab script computes interference patterns of the double-slit interferometer from a vortex beam.

```
% ========================================================================
% Script file: Cal_FringePattern.m
%
% Define variables:
%   Index_p: radial index
%   Index_m: azimuthal mode index
%   Lam: laser wavelength
%   sample_width: distance between two slits
%   L_screen: distance between the slit and the screen
% ========================================================================
clear; close all; clc;
set(0,'defaultAxesFontName', 'Helvetica');
%-- Input parameters
%- Laser
Index_p= 0;
Index_m= 1;
Lam= 0.4 *1e-3; % wavelength, unit: mm
%- Geometry
sample_width= 2;  % unit: mm
L_screen= 1000;   % unit: mm

%%
VecX= -5:0.01:5;
MatIN= zeros(length(VecX),length(VecX));
CenP = [(length(VecX)+1)/2 , (length(VecX)+1)/2];
MatOUT= AngleValueID(MatIN,CenP,'rad');
[Mx,My]= meshgrid(VecX,VecX);

M_phase1= exp(1i*Index_m*MatOUT);
M_phase2= angle(M_phase1);

AryP1= M_phase2(:,find(VecX==-sample_width,1));
AryP2= M_phase2(:,find(VecX==sample_width,1));

%% ------------------------------------------------------------------------
%- Generate Laguerre-Gaussian mode        (Radius,SpotSize,Res_r,Res_p,p,m)
[I0m, E0m, MatX, MatY] = GeneralizedLGBeam(5,2,0.01,(pi/1440),Index_p,Index_m);

%- Plot intensity pattern
fig1=figure(1);
surf(MatX,MatY,I0m,'EdgeColor','none'); %colormap('LightGray');
view(2); axis square;
set(gca,'XLim',[-3 3],'YLim',[-3 3],'XTick',[],'YTick',[]);
set(gcf,'color','white');
%- Plot phase pattern
fig2=figure(2);
surf(MatX,MatY,angle(E0m),'EdgeColor','none'); colormap('jet'); cb3=colorbar; axis square; view(-90,-90);
set(gca,'XLim',[-3 3],'YLim',[-3 3],'XTick',[],'YTick',[],'FontSize',24);
set(gcf,'color','white')
set(cb3,'Ticks',[-2.8 2.8],'TickLabels',{'-\pi' '\pi'},'FontSize',35)

% ------------------------------------------------------------------------
```

```
w= L_screen*Lam/sample_width;

vec_x= (-0.975):0.005:(0.975);
DPhi = AryP1-AryP2;

for j=1:length(DPhi)
       Iy(j,:)= cos(pi*vec_x/w+DPhi(j)/2).^2;
end

%- Plot fringe pattern
fig3=figure(3);
imagesc(Iy); colormap(fire); axis square
set(gca,'XTick',[],'YTick',[]);
set(gcf,'color','w','Position',[900 200 700 750]);


%%%%%%%%%%%%%%%%%%%%%%%%%%%%%%%%%%%%%%%%%%%%%%%%%%%%%%%%%%%%%%%%%%%%%%%%%%%%%%%

function [Mat_I, Mat_E, MatX, MatY]=GeneralizedLGBeam(Radius,SpotSize,Res_r,Res_p,p,m)
% This function generates the electric field and intensity profile of a
% Laguerre-Gaussian mode with radial index p and azimuthal index m.
%
% Inputs
%   - Radius: radius of the profile
%   - SpotSize: spot size of the beam
%   - Res_r, Res_p: resolution of the r- and phi-axis
%   - p, m: radial and azimuthal index of generalized Laguerre polynomials
%
% Outputs
%   - Mat_I, Mat_E: matrice of intensity and electric field profile
%   - MatX, MatY: meshgrid of x- and y- axis
Vec_r =0:Res_r:Radius;
Vec_p= -1*pi:Res_p:1*pi;
[R, Phi]= meshgrid(Vec_r,Vec_p);
w0= SpotSize;

MatX= R.*cos(Phi);
MatY= R.*sin(Phi);
%- generalized Laguerre polynomials
switch p
    case 0
        LP= @(x) 1;
    case 1
        LP= @(x) -x+m+1;
    case 2
        LP= @(x) x.^2/2-(m+2)*x+(m+2)*(m+1)/2;
    case 3
        LP= @(x) -x.^3/6+(m+3)*x.^2/2-(m+2)*(m+3)*x/2+(m+1)*(m+2)*(m+3)/6;
    case 4

    case 5
end

Cpm= sqrt(2*factorial(p)/(pi*factorial(p+abs(m))));
Mat_E= Cpm*exp(-R.^2/(w0^2)).*(R*sqrt(2)/w0).^m.*LP(2*R.^2/(w0^2)).*exp(-1i*m*Phi);
Mat_I= Mat_E.*conj(Mat_E);
end
```

Bibliography

[1] F. F. Chen. *Introduction to Plasma Physics and Controlled Fusion.* Springer, New York, 3rd edition, 2016.

[2] P. B. Corkum, N. H. Burnett, and F. Brunel. Above-threshold ionization in the long-wavelength limit. *Phys. Rev. Lett.*, 62:1259–1262, March 1989.

[3] P. B. Corkum. Plasma perspective on strong field multiphoton ionization. *Phys. Rev. Lett.*, 71:1994–1997, Sep 1993.

[4] Peter Amendt, David C. Eder, and Scott C. Wilks. X-ray lasing by optical-field-induced ionization. *Phys. Rev. Lett.*, 66:2589–2592, May 1991.

[5] Yutaka Nagata, Katsumi Midorikawa, Shoich Kubodera, Minoru Obara, Hideo Tashiro, and Koichi Toyoda. Soft-x-ray amplification of the Lyman-α transition by optical-field-induced ionization. *Phys. Rev. Lett.*, 71:3774–3777, Dec 1993.

[6] N. Lemos, T. Grismayer, L. Cardoso, G. Figueira, R. Issac, D. A. Jaroszynski, and J. M. Dias. Plasma expansion into a waveguide created by a linearly polarized femtosecond laser pulse. *Phys. Plasmas*, 20(6):063102, 2013.

[7] N. Lemos, T. Grismayer, L. Cardoso, J. Geada, G. Figueira, and J. M. Dias. Effects of laser polarization in the expansion of plasma waveguides. *Phys. Plasmas*, 20(10):103109, 2013.

[8] R. J. Shalloo, C. Arran, A. Picksley, A. von Boetticher, L. Corner, J. Holloway, G. Hine, J. Jonnerby, H. M. Milchberg, C. Thornton, R. Walczak, and S. M. Hooker. Low-density hydrodynamic optical-field-ionized plasma channels generated with an axicon lens. *Phys. Rev. Spec. Top. Accel Beams*, 22:041302, Apr 2019.

[9] S. C. Wilks, J. M. Dawson, W. B. Mori, T. Katsouleas, and M. E. Jones. Photon accelerator. *Phys. Rev. Lett.*, 62:2600–2603, May 1989.

[10] C. G. R. Geddes, Cs. Toth, J. van Tilborg, E. Esarey, C. B. Schroeder, D. Bruhwiler, C. Nieter, J. Cary, and W. P. Leemans. High-quality electron beams from a laser wakefield accelerator using plasma-channel guiding. *Nature*, 431(7008):538–541, 2004.

[11] M. Hentschel, R. Kienberger, Ch. Spielmann, G. A. Reider, N. Milosevic, T. Brabec, P. Corkum, U. Heinzmann, M. Drescher, and F. Krausz. Attosecond metrology. *Nature*, 414(6863):509–513, 2001.

[12] N. H. Burnett and P. B. Corkum. Cold-plasma production for recombination extreme-ultraviolet lasers by optical-field-induced ionization. *Journal of the Optical Society of America B: Optical Physics*, 6(6):1195–1199, Jun 1989.

[13] R. C. Davidson. Kinetic waves and instabilities in a uniform plasma. In A. A. Galeev and R. N. Sudan, editors, *Handbook of Plasma Physics*, volume 1, page 229. North-Holland, Amsterdam, 1983.

[14] D. Anderson, R. Fedele, and M. Lisak. A tutorial presentation of the two stream instability and Landau damping. *Am. J. Phys*, 69(12):1262–1266, 2001.

[15] Burton D. Fried. Mechanism for instability of transverse plasma waves. *Phys. Fluids*, 2(3):337–337, 1959.

[16] Erich S. Weibel. Spontaneously growing transverse waves in a plasma due to an anisotropic velocity distribution. *Phys. Rev. Lett.*, 2:83–84, Feb 1959.

[17] Mikhail V. Medvedev and Abraham Loeb. Generation of magnetic fields in the relativistic shock of gamma-ray burst sources. *Astrophys. J*, 526:697, 1999.

[18] G. Sarri, W. Schumaker, A. Di Piazza, M. Vargas, B. Dromey, M. E. Dieckmann, V. Chvykov, A. Maksimchuk, V. Yanovsky, Z. H. He, B. X. Hou, J. A. Nees, A. G. R. Thomas, C. H. Keitel, M. Zepf, and K. Krushelnick. Table-top laser-based source of femtosecond, collimated, ultrarelativistic positron beams. *Phys. Rev. Lett.*, 110:255002, Jun 2013.

[19] G. Sarri, K. Poder, J. M. Cole, W. Schumaker, A. Di Piazza, B. Reville, T. Dzelzainis, D. Doria, L. A. Gizzi, G. Grittani, S. Kar, C. H. Keitel, K. Krushelnick, S. Kuschel, S. P. D. Mangles, Z. Najmudin, N. Shukla, L. O. Silva, D. Symes, A. G. R. Thomas, M. Vargas, J. Vieira, and M. Zepf. Generation of neutral and high-density electron-positron pair plasmas in the laboratory. *Nat. Commun.*, 6(1):6747, 2015.

[20] F. Fiuza, R. A. Fonseca, J. Tonge, W. B. Mori, and L. O. Silva. Weibel-instability-mediated collisionless shocks in the laboratory with ultraintense lasers. *Phys. Rev. Lett.*, 108:235004, Jun 2012.

[21] Eckart Marsch. Kinetic physics of the solar corona and solar wind. *Living Rev. Sol. Phys.*, 3(1):1, 2006.

[22] Jiayong Zhong, Yutong Li, Xiaogang Wang, Jiaqi Wang, Quanli Dong, Chijie Xiao, Shoujun Wang, Xun Liu, Lei Zhang, Lin An, Feilu Wang, Jianqiang Zhu, Yuan Gu, Xiantu He, Gang Zhao, and Jie Zhang. Modelling loop-top X-ray source and reconnection outflows in solar flares with intense lasers. *Nat. Phys.*, 6(12):984–987, 2010.

[23] Haihong Che, Melvyn L. Goldstein, Patrick H. Diamond, and Roald Z. Sagdeev. How electron two-stream instability drives cyclic Langmuir collapse and continuous coherent emission. *Proc. Natl. Acad. Sci. U.S.A.*, 114(7):1502–1507, 2017.

[24] W. C. Feldman, R. C. Anderson, S. J. Bame, J. T. Gosling, R. D. Zwickl, and E. J. Smith. Electron velocity distributions near interplantary shocks. *J. Geophys. Res.*, 88(A12):9949–9958, 1983.

[25] C. S. Wu, D. Winske, Y. M. Zhou, S. T. Tsai, P. Rodriguez, M. Tanaka, K. Papadopoulos, K. Akimoto, C. S. Lin, M. M. Leroy, and C. C. Goodrich. Microinstabilities associated with a high Mach number, perpendicular bow shock. *Space Sci. Rev.*, 37(1):63–109, 1984.

[26] R. Schlickeiser, M. J. Michno, D. Ibscher, M. Lazar, and T. Skoda. Modified temperature-anisotropy instability thresholds in the solar wind. *Phys. Rev. Lett.*, 107:201102, Nov 2011.

[27] Peter H. Yoon. Kinetic instabilities in the solar wind driven by temperature anisotropies. *Reviews of Modern Plasma Physics*, 1(1):4, 2017.

[28] L. O. Silva, R. Bingham, J. M. Dawson, J. T. Mendonça, and P. K. Shukla. Neutrino driven streaming instabilities in a dense plasma. *Phys. Rev. Lett.*, 83:2703–2706, Oct 1999.

[29] P. K. Shukla, L. O. Silva, H. Bethe, R. Bingham, J. M. Dawson, L. Stenflo, J. T. Mendonça, and S. Dalhed. The physics of collective neutrino-plasma interactions. *Plasma Phys. Controlled Fusion*, 41(3A):A699–A707, jan 1999.

[30] S. Mrówczyński. Stream instabilities of the quark-gluon plasma. *Phys. Lett. B*, 214(4):587 – 590, 1988.

[31] S. Mrówczyński. Instabilities driven equilibration of the quark-gluon plasma. *Acta Phys. Polon. B*, 37:427–454, 2006.

[32] Peter Arnold, Jonathan Lenaghan, Guy D. Moore, and Laurence G. Yaffe. Apparent thermalization due to plasma instabilities in the quark-gluon plasma. *Phys. Rev. Lett.*, 94:072302, Feb 2005.

[33] Y. Sentoku, K. Mima, P. Kaw, and K. Nishikawa. Anomalous resistivity resulting from MeV-electron transport in overdense plasma. *Phys. Rev. Lett.*, 90:155001, Apr 2003.

[34] J. T. Mendonça, P. Norreys, R. Bingham, and J. R. Davies. Beam instabilities in laser-plasma interaction: relevance to preferential ion heating. *Phys. Rev. Lett.*, 94:245002, Jun 2005.

[35] V. P. Krainov. Weibel instability in plasma produced by a superintense femtosecond laser pulse. *J. Exp. Theor. Phys.*, 96(3):430–435, Mar 2003.

[36] V. Yu. Bychenkov, D. V. Romanov, W. Rozmus, C. E. Capjack, and R. Fedosejevs. Distinctive features of photoionized plasma from short x-ray-pulse interaction with gaseous medium. *Phys. Plasmas*, 13(1):013101, 2006.

[37] K. Yu. Vagin and S. A. Uryupin. Electron modes of plasma generated at tunnel ionization of atoms by a circularly polarized radiation. *Phys. Plasmas*, 24(10):103118, 2017.

[38] U. Mohideen, M. H. Sher, H. W. K. Tom, G. D. Aumiller, O. R. Wood, R. R. Freeman, J. Bokor, and P. H. Bucksbaum. High intensity above-threshold ionization of He. *Phys. Rev. Lett.*, 71:509–512, Jul 1993.

[39] S. J. McNaught, J. P. Knauer, and D. D. Meyerhofer. Measurement of the initial condition of electrons ionized by a linearly polarized, high-intensity laser. *Phys. Rev. Lett.*, 78:626–629, Jan 1997.

[40] C. I. Moore, A. Ting, S. J. McNaught, J. Qiu, H. R. Burris, and P. Sprangle. A laser-accelerator injector based on laser ionization and ponderomotive acceleration of electrons. *Phys. Rev. Lett.*, 82:1688–1691, Feb 1999.

[41] T. E. Glover, T. D. Donnelly, E. A. Lipman, A. Sullivan, and R. W. Falcone. Subpicosecond Thomson scattering measurements of optically ionized helium plasmas. *Phys. Rev. Lett.*, 73:78–81, Jul 1994.

[42] T. E. Glover, J. K. Crane, M. D. Perry, R. W. Lee, and R. W. Falcone. Measurement of velocity distributions and recombination kinetics in tunnel-ionized helium plasmas. *Phys. Rev. Lett.*, 75:445–448, Jul 1995.

[43] A. A. Offenberger, W. Blyth, E. Dangor, A. Djaoui, M. H. Key, Z. Najmudin, and J. S. Wark. Electron temperature of optically ionized gases produced by high intensity 268 nm laser radiation. *Phys. Rev. Lett.*, 71:3983–3986, Dec 1993.

[44] C. J. Zhang, J. F. Hua, Y. Wan, C.-H. Pai, B. Guo, J. Zhang, Y. Ma, F. Li, Y. P. Wu, H.-H. Chu, Y. Q. Gu, X. L. Xu, W. B. Mori, C. Joshi, J. Wang, and W. Lu. Femtosecond probing of plasma wakefields and observation of the plasma wake reversal using a relativistic electron bunch. *Phys. Rev. Lett.*, 119:064801, Aug 2017.

[45] Martin Centurion, Peter Reckenthaeler, Sergei A. Trushin, Ferenc Krausz, and Ernst E. Fill. Picosecond electron deflectometry of optical-field ionized plasmas. *Nat. Photonics*, 2(5):315–318, 2008.

[46] M. Dunne, T. Afshar-Rad, J. Edwards, A. J. MacKinnon, S. M. Viana, O. Willi, and G. Pert. Experimental observations of the expansion of an optical-field-induced ionization channel in a gas jet target. *Phys. Rev. Lett.*, 72:1024–1027, Feb 1994.

[47] Martin Centurion, Ye Pu, Zhiwen Liu, Demetri Psaltis, and Theodor W. Hänsch. Holographic recording of laser-induced plasma. *Opt. Lett.*, 29(7):772–774, Apr 2004.

[48] R. A. Beth. Mechanical detection and measurement of the angular momentum of light. *Phys. Rev.*, 50:115–125, Jul 1936.

[49] M. G. Haines. Generation of an axial magnetic field from photon spin. *Phys. Rev. Lett.*, 87:135005, Sep 2001.

[50] D. Strickland and G. Mourou. Compression of amplified chirped optical pulses. *Opt. Commun.*, 56(3):219 – 221, 1985.

[51] R. G. Meyerand and A. F. Haught. Gas breakdown at optical frequencies. *Phys. Rev. Lett.*, 11:401–403, Nov 1963.

[52] P. Lambropoulos. Multiphoton ionization of one-electron atoms with circularly polarized light. *Phys. Rev. Lett.*, 29:453–455, Aug 1972.

[53] P. Lambropoulos. Topics on Multiphoton Processes in Atoms. volume 12 of *Advances in Atomic and Molecular Physics*, pages 87 – 164. Academic Press, 1976.

[54] L. V. Keldysh. Ionization in the field of a strong electromagnetic wave. *J. Exp. Theor. Phys.*, 20(5):1307, May 1965.

[55] N. B. Delone and V. P. Krainov. Tunneling and barrier-suppression ionization of atoms and ions in a laser radiation field. *Physics-Uspekhi*, 41(5):469–485, may 1998.

[56] S. Augst, D. D. Meyerhofer, D. Strickland, and S. L. Chin. Laser ionization of noble gases by Coulomb-barrier suppression. *J. Opt. Soc. Am. B*, 8(4):858–867, Apr 1991.

[57] A. M. Perelomov, V. S. Popov, and M. V. Terent'ev. Ionization of atoms in an alternating electric field. *J. Exp. Theor. Phys.*, 23:924, November 1966.

[58] Yu Hang Lai, Junliang Xu, Urszula B. Szafruga, Bradford K. Talbert, Xiaowei Gong, Kaikai Zhang, Harald Fuest, Matthias F. Kling, Cosmin I. Blaga, Pierre Agostini, and Louis F. DiMauro. Experimental investigation of strong-field-ionization theories for laser fields from visible to midinfrared frequencies. *Phys. Rev. A*, 96:063417, Dec 2017.

[59] M. V. Ammosov, N. B. Delone, and V. P. Krainov. Tunnel ionization of complex atoms and of atomic ions in an alternating electromagnetic field. *J. Exp. Theor. Phys.*, 64(6):1191, December 1986.

[60] D. Dimitrovski, J. Maurer, H. Stapelfeldt, and L. B. Madsen. Low-energy photoelectrons in strong-field ionization by laser pulses with large ellipticity. *Phys. Rev. Lett.*, 113:103005, Sep 2014.

[61] B. M. Penetrante and J. N. Bardsley. Residual energy in plasmas produced by intense subpicosecond lasers. *Phys. Rev. A*, 43:3100–3113, Mar 1991.

[62] S. C. Rae and K. Burnett. Possible production of cold plasmas through optical-field-induced ionization. *Phys. Rev. A*, 46:2077–2083, Aug 1992.

[63] K. B. Persson. Inertia-controlled ambipolar diffusion. *Phys. Fluids*, 5(12):1625–1632, 1962.

[64] Li Zhang, Xinhua Xie, Stefan Roither, Daniil Kartashov, Y. L. Wang, C. L. Wang, Markus Schöffler, Dror Shafir, Paul B. Corkum, Andrius Baltuška, Igor Ivanov, Anatoli Kheifets, X. J. Liu, André Staudte, and Markus Kitzler. Laser-sub-cycle two-dimensional electron-momentum mapping using orthogonal two-color fields. *Phys. Rev. A*, 90:061401, Dec 2014.

[65] Christopher A. Mancuso, Daniel D. Hickstein, Patrik Grychtol, Ronny Knut, Ofer Kfir, Xiao-Min Tong, Franklin Dollar, Dmitriy Zusin, Maithreyi Gopalakrishnan, Christian Gentry, Emrah Turgut, Jennifer L. Ellis, Ming-Chang Chen, Avner Fleischer, Oren Cohen, Henry C. Kapteyn, and Margaret M. Murnane. Strong-field ionization with two-color circularly polarized laser fields. *Phys. Rev. A*, 91:031402, Mar 2015.

[66] C. Joshi. Plasma accelerators. *Sci. Amer.*, 294:40–47, February 2006.

[67] C. Joshi, T. Tajima, J. M. Dawson, H. A. Baldis, and N. A. Ebrahim. Forward Raman instability and electron acceleration. *Phys. Rev. Lett.*, 47:1285–1288, Nov 1981.

[68] J. L. Shaw, N. Lemos, L. D. Amorim, N. Vafaei-Najafabadi, K. A. Marsh, F. S. Tsung, W. B. Mori, and C. Joshi. Role of direct laser acceleration of electrons in a laser wakefield accelerator with ionization injection. *Phys. Rev. Lett.*, 118:064801, Feb 2017.

[69] R. A. Fonseca, L. O. Silva, F. S. Tsung, V. K. Decyk, W. Lu, C. Ren, W. B. Mori, S. Deng, S. Lee, T. Katsouleas, and J. C. Adam. OSIRIS: A Three-Dimensional, Fully Relativistic Particle in Cell Code for Modeling Plasma Based Accelerators. In *Lect. Notes Comput. Sci.*, pages 342–351, 2002.

[70] André T. J. B. Eppink and David H. Parker. Velocity map imaging of ions and electrons using electrostatic lenses: application in photoelectron and photofragment ion imaging of molecular oxygen. *Rev. Sci. Instrum.*, 68(9):3477–3484, 1997.

[71] R. H. Huddlestone and S. L. Leonard. *Plasma Diagnostic Techniques.* New York, Academic Press, 1965.

[72] Dustin H. Froula, Siegfried H. Glenzer, Neville C. Luhmann, and John Sheffield. *Plasma Scattering of Electromagnetic Radiation.* Academic Press, Boston, second edition edition, 2011.

[73] B. D. Fried and S. D. Conte. *The Plasma Dispersion Function.* Academic Press, 1961.

[74] M. V. Chegotov. Thomson scattering in a plasma created by a short intense laser pulse. *Plasma Phys. Rep.*, 26(7):602–605, Jul 2000.

[75] Aleksander S. Radunsky, Ellen M. Kosik Williams, Ian A. Walmsley, Piotr Wasylczyk, Wojciech Wasilewski, Alfred B. U'Ren, and Matthew E. Anderson. Simplified spectral phase interferometry for direct electric-field reconstruction by using a thick nonlinear crystal. *Opt. Lett.*, 31(7):1008–1010, Apr 2006.

[76] A. Bret, M.-C. Firpo, and C. Deutsch. Collective electromagnetic modes for beam-plasma interaction in the whole k space. *Phys. Rev. E*, 70:046401, Oct 2004.

[77] Chaojie Zhang, Chen-Kang Huang, Ken A. Marsh, Chris E. Clayton, Warren B. Mori, and Chan Joshi. Ultrafast optical field-ionized gases— A laboratory platform for studying kinetic plasma instabilities. *Sci. Adv.*, 5(9), 2019.

[78] A. Bret, L. Gremillet, and M. E. Dieckmann. Multidimensional electron beam-plasma instabilities in the relativistic regime. *Phys. Plasmas*, 17(12):120501, 2010.

[79] A. Bret, M.-C. Firpo, and C. Deutsch. Characterization of the initial filamentation of a relativistic electron beam passing through a plasma. *Phys. Rev. Lett.*, 94:115002, Mar 2005.

[80] R. J. Goldston and P. H. Rutherford. *Introduction to Plasma Physics*. CRC Press, 1995.

[81] M. Tzoufras, C. Ren, F. S. Tsung, J. W. Tonge, W. B. Mori, M. Fiore, R. A. Fonseca, and L. O. Silva. Space-charge effects in the current-filamentation or Weibel instability. *Phys. Rev. Lett.*, 96:105002, Mar 2006.

[82] A. Bret, L. Gremillet, and J. C. Bellido. How really transverse is the filamentation instability? *Phys. Plasmas*, 14(3):032103, 2007.

[83] D. H. Froula, J. S. Ross, L. Divol, and S. H. Glenzer. Thomson-scattering techniques to diagnose local electron and ion temperatures, density, and plasma wave amplitudes in laser produced plasmas (invited). *Rev. Sci. Instrum.*, 77(10):10E522, 2006.

[84] J. Katz, R. Boni, R. Rivlis, C. Muir, and D. H. Froula. A pulse-front-tilt-compensated streaked optical spectrometer with high throughput and picosecond time resolution. *Rev. Sci. Instrum.*, 87(11):11E535, 2016.

[85] J.-C. Chanteloup. Multiple-wave lateral shearing interferometry for wave-front sensing. *Appl. Opt.*, 44(9):1559–1571, Mar 2005.

[86] Biao Hao, Z.-M. Sheng, C. Ren, and J. Zhang. Relativistic collisional current-filamentation instability and two-stream instability in dense plasma. *Phys. Rev. E*, 79:046409, Apr 2009.

[87] D. V. Romanov, V. Yu. Bychenkov, W. Rozmus, C. E. Capjack, and R. Fedosejevs. Self-organization of a plasma due to 3D volution of the Weibel instability. *Phys. Rev. Lett.*, 93:215004, Nov 2004.

[88] Sudipta Mondal, V. Narayanan, Wen Jun Ding, Amit D. Lad, Biao Hao, Saima Ahmad, Wei Min Wang, Zheng Ming Sheng, Sudip Sengupta, Predhiman Kaw, Amita Das, and G. Ravindra Kumar. Direct observation of turbulent magnetic fields in hot, dense laser produced plasmas. *Proceedings of the National Academy of Sciences*, 109(21):8011–8015, 2012.

[89] Gourab Chatterjee, Kevin M. Schoeffler, Prashant Kumar Singh, Amitava Adak, Amit D. Lad, Sudip Sengupta, Predhiman Kaw, Luis O. Silva, Amita Das, and G. Ravindra Kumar. Magnetic turbulence in a table-top laser-plasma relevant to astrophysical scenarios. *Nat. Commun.*, 8(1):15970, 2017.

[90] Thomas H. Stix. *Waves in Plasmas*. AIP-Press, New York, 1st edition, 1992.

[91] C.-J. Zhang, C.-K. Huang, K. A. Marsh, and C. Joshi. Probing thermal Weibel instability in optical-field-ionized plasmas using relativistic electron bunches. *Plasma Phys. Controlled Fusion*, 62(2):024010, jan 2020.

[92] Chaojie Zhang, Jianfei Hua, Yipeng Wu, Yu Fang, Yue Ma, Tianliang Zhang, Shuang Liu, Bo Peng, Yunxiao He, Chen-Kang Huang, Ken A. Marsh, Warren B. Mori, Wei Lu, and Chan Joshi. Measurements of the growth and saturation of electron Weibel instability in optical-field ionized plasmas. *Phys. Rev. Lett.*, 125:255001, Dec 2020.

[93] C.-K. Huang, C.-J. Zhang, K. A. Marsh, C. E. Clayton, and C. Joshi. Initializing anisotropic electron velocity distribution functions in optical-field ionized plasmas. *Plasma Phys. Controlled Fusion*, 62(2):024011, jan 2020.

[94] A. Bret, L. Gremillet, D. Bénisti, and E. Lefebvre. Exact relativistic kinetic theory of an electron-beam-plasma system: hierarchy of the competing modes in the system-parameter space. *Phys. Rev. Lett.*, 100:205008, May 2008.

[95] K. Krushelnick, A. Ting, H. R. Burris, A. Fisher, C. Manka, and E. Esarey. Second harmonic generation of stimulated Raman scattered light in underdense plasmas. *Phys. Rev. Lett.*, 75:3681–3684, Nov 1995.

[96] D. F. Gordon, B. Hafizi, D. Kaganovich, and A. Ting. Electro-optic shocks from ultraintense laser-plasma interactions. *Phys. Rev. Lett.*, 101:045004, Jul 2008.

[97] L. Allen, M. W. Beijersbergen, R. J. C. Spreeuw, and J. P. Woerdman. Orbital angular momentum of light and the transformation of Laguerre-Gaussian laser modes. *Phys. Rev. A*, 45:8185–8189, Jun 1992.

[98] H. He, M. E. J. Friese, N. R. Heckenberg, and H. Rubinsztein-Dunlop. Direct observation of transfer of angular momentum to absorptive particles from a laser beam with a phase singularity. *Phys. Rev. Lett.*, 75:826–829, Jul 1995.

[99] A. T. O'Neil, I. MacVicar, L. Allen, and M. J. Padgett. Intrinsic and extrinsic nature of the orbital angular momentum of a light beam. *Phys. Rev. Lett.*, 88:053601, Jan 2002.

[100] M. E. J. Friese, J. Enger, H. Rubinsztein-Dunlop, and N. R. Heckenberg. Optical angular-momentum transfer to trapped absorbing particles. *Phys. Rev. A*, 54:1593–1596, Aug 1996.

[101] N. B. Simpson, K. Dholakia, L. Allen, and M. J. Padgett. Mechanical equivalence of spin and orbital angular momentum of light: an optical spanner. *Opt. Lett.*, 22(1):52–54, Jan 1997.

[102] J. Courtial, D. A. Robertson, K. Dholakia, L. Allen, and M. J. Padgett. Rotational frequency shift of a light beam. *Phys. Rev. Lett.*, 81:4828–4830, Nov 1998.

[103] M. Padgett and R. Bowman. Tweezers with a twist. *Nat. Photonics*, 5(6):343–348, 2011.

[104] W. P. Wang, C. Jiang, B. F. Shen, F. Yuan, Z. M. Gan, H. Zhang, S. H. Zhai, and Z. Z. Xu. New optical manipulation of relativistic vortex cutter. *Phys. Rev. Lett.*, 122:024801, Jan 2019.

[105] W. Kruer. *The Physics of Laser Plasma Interactions*. CRC Press, Boca Raton, 2003.

[106] S. Eliezer. *The Interaction of High-Power Lasers with Plasmas*. CRC Press, Boca Raton, 2002.

[107] J. T. Mendonça, B. Thide, and H. Then. Stimulated Raman and Brillouin backscattering of collimated beams carrying orbital angular momentum. *Phys. Rev. Lett.*, 102:185005, May 2009.

[108] J. Vieira, J. T. Mendonça, and F. Quéré. Optical control of the topology of laser-plasma accelerators. *Phys. Rev. Lett.*, 121:054801, Jul 2018.

[109] J. Vieira and J. T. Mendonça. Nonlinear laser driven donut wakefields for positron and electron acceleration. *Phys. Rev. Lett.*, 112:215001, May 2014.

[110] J. T. Mendonça and J. Vieira. Donut wakefields generated by intense laser pulses with orbital angular momentum. *Phys. Plasmas*, 21(3):033107, 2014.

[111] G.-B. Zhang, M. Chen, C. B. Schroeder, J. Luo, M. Zeng, F.-Y. Li, L.-L. Yu, S.-M. Weng, Y.-Y. Ma, T.-P. Yu, Z.-M. Sheng, and E. Esarey. Acceleration and evolution of a hollow electron beam in wakefields driven by a Laguerre-Gaussian laser pulse. *Phys. Plasmas*, 23(3):033114, 2016.

[112] C. Brabetz, S. Busold, T. Cowan, O. Deppert, D. Jahn, O. Kester, M. Roth, D. Schumacher, and V. Bagnoud. Laser-driven ion acceleration with hollow laser beams. *Phys. Plasmas*, 22(1):013105, 2015.

[113] Joana Luís Martins, Jorge Vieira, Julien Ferri, and Tünde Fülöp. Radiation emission in laser-wakefields driven by structured laser pulses with orbital angular momentum. *Sci. Rep.*, 9(1):9840, 2019.

[114] S. Ali, J. R. Davies, and J. T. Mendonca. Inverse Faraday effect with linearly polarized laser pulses. *Phys. Rev. Lett.*, 105:035001, Jul 2010.

[115] Y. Shi, J. Vieira, R. M. G. M. Trines, R. Bingham, B. F. Shen, and R. J. Kingham. Magnetic field generation in plasma waves driven by copropagating intense twisted lasers. *Phys. Rev. Lett.*, 121:145002, Oct 2018.

[116] A. Denoeud, L. Chopineau, A. Leblanc, and F. Quéré. Interaction of ultraintense laser vortices with plasma mirrors. *Phys. Rev. Lett.*, 118:033902, Jan 2017.

[117] Jonas B. Ohland, Udo Eisenbarth, Markus Roth, and Vincent Bagnoud. A study on the effects and visibility of low-order aberrations on laser beams with orbital angular momentum. *Appl. Phys. B*, 125(11):202, 2019.

[118] D. F. Gordon, B. Hafizi, and A. Ting. Nonlinear conversion of photon spin to photon orbital angular momentum. *Opt. Lett.*, 34:3280–3282, 2009.

[119] Kenan Qu, Qing Jia, and Nathaniel J. Fisch. Plasma q-plate for generation and manipulation of intense optical vortices. *Phys. Rev. E*, 96:053207, Nov 2017.

[120] X. Zhang, B. Shen, Y. Shi, X. Wang, L. Zhang, W. Wang, J. Xu, L. Yi, and Z. Xu. Generation of intense high-order vortex harmonics. *Phys. Rev. Lett.*, 114:173901, Apr 2015.

[121] A. Leblanc, A. Denoeud, L. Chopineau, G. Mennerat, Ph. Martin, and F. Quéré. Plasma holograms for ultrahigh-intensity optics. *Nat. Phys.*, 13(5):440–443, 2017.

[122] J. Vieira, R. M. G. M. Trines, E. P. Alves, R. A. Fonseca, J. T. Mendonça, R. Bingham, P. Norreys, and L. O. Silva. Amplification and generation of ultra-intense twisted laser pulses via stimulated Raman scattering. *Nat. Commun.*, 7(1):10371, 2016.

[123] Alex Wilhelm, David Schmidt, and Charles Durfee. Nonlinear optical conversion of photon spin to orbital angular momentum. In *Conference on Lasers and Electro-Optics*, page FTh3E.3. Optical Society of America, 2018.

[124] G. Gariepy, J. Leach, K. T. Kim, T. J. Hammond, E. Frumker, R. W. Boyd, and P. B. Corkum. Creating high-harmonic beams with controlled orbital angular momentum. *Phys. Rev. Lett.*, 113:153901, Oct 2014.

[125] Kevin M. Dorney, Laura Rego, Nathan J. Brooks, Julio San Román, Chen-Ting Liao, Jennifer L. Ellis, Dmitriy Zusin, Christian Gentry, Quynh L. Nguyen, Justin M. Shaw, Antonio Picón, Luis Plaja, Henry C. Kapteyn, Margaret M. Murnane, and Carlos Hernández-García. Controlling the polarization and vortex charge of attosecond high-harmonic beams via simultaneous spin-orbit momentum conservation. *Nat. Photonics*, 13(2):123–130, 2019.

[126] W. P. Leemans, C. E. Clayton, W. B. Mori, K. A. Marsh, P. K. Kaw, A. Dyson, C. Joshi, and J. M. Wallace. Experiments and simulations of tunnel-ionized plasmas. *Phys. Rev. A*, 46:1091–1105, Jul 1992.

[127] V. Malka, A. Modena, Z. Najmudin, A. E. Dangor, C. E. Clayton, K. A. Marsh, C. Joshi, C. Danson, D. Neely, and F. N. Walsh. Second harmonic generation and its interaction with relativistic plasma waves driven by forward Raman instability in underdense plasmas. *Phys. Plasmas*, 4(4):1127–1131, 1997.

[128] Szu-yuan Chen, Anatoly Maksimchuk, and Donald Umstadter. Experimental observation of relativistic nonlinear Thomson scattering. *Nature*, 396(6712):653–655, 1998.

[129] K. Y. Kim, I. Alexeev, and H. M. Milchberg. Single-shot measurement of laser-induced double step ionization of helium. *Opt. Express*, 10(26):1563–1572, Dec 2002.

[130] Primož Rebernik Ribič, Benedikt Rösner, David Gauthier, Enrico Allaria, Florian Döring, Laura Foglia, Luca Giannessi, Nicola Mahne, Michele Manfredda, Claudio Masciovecchio, Riccardo Mincigrucci, Najmeh Mirian, Emiliano Principi, Eléonore Roussel, Alberto Simoncig, Simone Spampinati, Christian David, and Giovanni De Ninno. Extreme-ultraviolet vortices from a free-electron laser. *Phys. Rev. X*, 7:031036, Aug 2017.

[131] D. Gauthier, P. Rebernik Ribič, G. Adhikary, A. Camper, C. Chappuis, R. Cucini, L. F. DiMauro, G. Dovillaire, F. Frassetto, R. Géneaux, P. Miotti, L. Poletto, B. Ressel, C. Spezzani, M. Stupar, T. Ruchon, and G. De Ninno. Tunable orbital angular momentum in high-harmonic generation. *Nat. Commun.*, 8(1):14971, 2017.

[132] C. A. Balanis. *Advanced Engineering Electromagnetics*. Wiley, 2012.

[133] F. A. Starikov, G. G. Kochemasov, S. M. Kulikov, A. N. Manachinsky, N. V. Maslov, A. V. Ogorodnikov, S. A. Sukharev, V. P. Aksenov, I. V. Izmailov, F. Yu. Kanev, V. V. Atuchin, and I. S. Soldatenkov. Wavefront reconstruction of an optical vortex by a Hartmann-Shack sensor. *Opt. Lett.*, 32(16):2291–2293, Aug 2007.

[134] Jonathan Leach, Stephen Keen, Miles J. Padgett, Christopher Saunter, and Gordon D. Love. Direct measurement of the skew angle of the Poynting vector in a helically phased beam. *Opt. Express*, 14(25):11919–11924, Dec 2006.

[135] H. I. Sztul and R. R. Alfano. Double-slit interference with Laguerre-Gaussian beams. *Opt. Lett.*, 31(7):999–1001, Apr 2006.

[136] O. Emile and J. Emile. Young's double-slit interference pattern from a twisted beam. *Appl. Phys. B*, 117(1):487–491, 2014.

[137] D. H. Goldstein. *Polarized Light*. CRC Press, 2017.

[138] T. Fujimoto and A. Iwamae. *Plasma Polarization Spectroscopy*. Springer, Berlin, Heidelberg, 2008.

[139] J. Deschamps, M. Fitaire, and M. Lagoutte. Inverse Faraday effect in a plasma. *Phys. Rev. Lett.*, 25:1330–1332, Nov 1970.

[140] Chaojie Zhang, Chen-Kang Huang, Ken A. Marsh, Chris E. Clayton, Warren B. Mori, and Chan Joshi. Ultrafast optical field–ionized gases—A laboratory platform for studying kinetic plasma instabilities. *Sci. Adv.*, 5(9), 2019.

[141] W. J. Blyth, S. G. Preston, A. A. Offenberger, M. H. Key, J. S. Wark, Z. Najmudin, A. Modena, A. Djaoui, and A. E. Dangor. Plasma temperature in optical field ionization of gases by intense ultrashort pulses of ultraviolet radiation. *Phys. Rev. Lett.*, 74:554–557, Jan 1995.